Treatment planning optimization for non-coplanar volumetric modulated arc therapy

Franklin Okoli

Franklin Okoli. Treatment planning optimization for non-coplanar volumetric modulated arc therapy. Human health and pathology. Université de Bretagne occidentale - Brest, 2020. English. NNT : 2020BRES0061 . tel-03384158

THESE DE DOCTORAT DE

L'UNIVERSITE
DE BRETAGNE OCCIDENTALE

ECOLE DOCTORALE N° 605
Biologie Santé
Spécialité : Analyse et Traitement de l'Information et des Images Médicales

Par
Franklin OKOLI

Treatment Planning Optimization for Non-coplanar Volumetric Modulated Arc Therapy

Thèse présentée et soutenue à Brest le 17 Novembre 2020
Unité de recherche : LaTIM UMR 1101

Rapporteurs avant soutenance :

Jean-Michel LETANG	Maitre de Conférences, CREATIS Lyon
Ben HEIJMEN	Professeur, Erasmus University Medical Center Rotterdam

Composition du Jury :

Pdt du jury :	David SARRUT	DR CNRS, CREATIS Lyon
Examinateurs :	Jean-Michel LETANG	Maitre de Conférences, CREATIS Lyon
	Ben HEIJMEN	Professeur, Erasmus University Medical Center Rotterdam
	Salih ABDELAZIZ	Maitre de Conférences, LIRMM Montpellier
	Julien BERT	Ingénieur de Recherche, LaTIM Brest
Dir. de thèse :	Dimitris VISVIKIS	DR INSERM, LaTIM Brest

CONTENTS

Page

LIST OF FIGURES

LIST OF TABLES

To my family, teachers, friends and every one who made me.

"Reach for the stars, even if you
fail you will land on the moon."

CHAPTER

1

INTRODUCTION

This chapter aims to provide background information on cancer and some of the methods for treating cancer. We start by providing a general knowledge about cancer, the associated risk factors, the rates of incidences and the rates of mortality in order to understand the extent of the problem. We make a brief recall on radiotherapy and the different techniques used for treatment planning. We make a further study on the state of the art related to non-coplanar VMAT treatment planning. We identify some of the problems that hinder non-coplanar VMAT treatment planning and make an objective thesis statement of our approach for solving some of these problems.

1.1 Cancer

Cancer is a disease that occurs due to abnormal cell growth which can spread to other parts of the body [7] [8]. Some of the body's cells begin to divide without stopping and spread into surrounding tissues. There are several types of cancer which can be identified by the body organ or structure where they occur or the type of cells that gives rise to this cancer. Cancer is one of the main causes of premature deaths (death at less than 65 years) with more than 17 million new cases world wide in 2018 [9] and almost 2 million deaths each year in Europe [10]. In France, cancer is the leading cause of death with an estimated 455,000 new cases in 2018 and an incidence rate of 344.1 per 100,000 of the population measured in the same year [11].

1.1.1 Treatment of Cancer

The chances of surviving cancer is much more improved through early detection and treatment [12]. Today there exists treatment techniques that can be used for the treatment of cancer. They include:

- **Surgery**: Cancer surgery is a technique where a surgical oncologist removes the cancer tumor and the surrounding tissues during a surgical operation [13]. Some non-negligible side effects could appear after surgery such as the loss of an organ function or loss of the entire organ when removed. There is also a risk of a relapse if the cancer has spread to other parts of the body different from where the surgery was performed.
- **Chemotherapy**: Chemotherapy is a technique where drugs are prescribed for a person who has cancer to be used to destroy the cancer cells [14]. These drugs can be administered intravenously or ingested through the mouth and can cause some side-effects such as loss of hair, nausea and sores on the body.
- **Hormonal Therapy**: Hormonal therapy involves the altering or stopping of the hormonal activity of the body which otherwise would aid the development of cancer in the human body [15]. It is mainly applied to breast, ovarian, kidney and prostate cancers by administering medicines which will inhibit the production of such hormones.
- **Targeted Cancer Therapy**: Targeted therapy is a recent development in precision medicine which allows the treatment of cancerous cells while sparing the other healthy cells by taking advantage of the differences between both cells [16]. Targeted therapy uses specially made drugs to target the specific cancer cells. It usually involves a biopsy to take some cancer tissues from the patient and design drugs to specifically target such cancerous tissues for destruction.
- **Radiotherapy**: This is the use of radiation in order to kill cancer cells. Radiotherapy works on the principle that when sufficient energy from ionising radiation is deposited on cancerous cells, it causes damage to the DNA structure of these cells causing them to die off without an ability to regenerate.

A combination of cancer treatment techniques can be applied during treatment depending on the stage of the tumor, patient age and health status. When it is not possible to remove the tumor by surgery (inoperable cases), chemotherapy, targeted therapy and radiation therapy are usually recommended by the doctor [17].

1.2 Radiotherapy

Radiotherapy is the use of radiation in order to kill cancer cells. Radiation activity was discovered in 1896 by a french scientist Henri Becquerel [18]. Further works out in this field were carried by Pierre and Marie Curie, Ernest Rutherford and many other scientists till date. Radioactivity occurs due to the emission of radioactive particles (α, β, γ) and energy from the nucleus of an unstable atom in order to form a stable nuclide [19]. The measurement unit of the absorbed radioactivity dose is the Gray (Gy) which defines the deposit of a joule of radiation energy on a kilogram of matter. The quantity of radiation can be measured using ionisation chambers and diodes.

$$1Gy = 1Jkg^{-1} \tag{1.1}$$

1.2.1 How radiation kills cancer cells

Radiation kills cancer cells by damaging the Deoxyribonucleic acid (DNA) portion of cells [20]. DNA is the part of the cell that contains the genetic information used in cell division and when it is damaged, the cell division stops. The effect of radiation on the DNA is seen in two forms:

Direct effect of radiation on cells

The direct action of radiation energy on cells can induce the liberation of free electrons from the water molecules present in the cell. These electrons can go on to rupture of the DNA structure directly. The electron release is shown below:

$$H_2O \Rightarrow H_2O^+ + e^- \tag{1.2}$$

Indirect effect of radiation on cells

The indirect action of radiation on cells comes mainly from the radiolysis of water [21]. Incident radiation causes water molecules to split into hydrogen ions, hydrogen peroxide and other free radicals. These free radicals interact with the DNA molecules causing a chemical reaction that damage the cell structure. These free radicals can go on to rupture of the DNA structure directly.

$$H_2O \Rightarrow H^+ + HO^o \tag{1.3}$$

1.2.2 The goals of Radiotherapy

The main goal of radiotherapy is to deliver a prescribed radiation dose to the tumor volume while sparing the healthy cells and tissues surrounding the tumor [22]. Two effects can be desired:

- Curative Effect: The primary aim of radiotherapy is to kill the cancer cells by the exposure of the cancer cells to radiation.

- Palliative Effect: Another aim of radiotherapy could be to alleviate the suffering of cancer patient from a specific symptom such as pain or bleeding.

1.3 Types of Radiotherapy

- **Brachytherapy** which is a technique where seeds of radioactive source such as ^{125}I , $^{137}C_s$, $^{198}A_u$, are placed close to the tumor (interstitial, intracavitary or on the skin surface) to kill the tumor cells [1]. The seeds may either be placed during a temporary period and removed according to the prescribed dose or left permanently in the body of the patient with no lasting effects [23]. We will not be focusing on brachytherapy as a treatment technique in this thesis, interested readers are encouraged to refer to more detailed explanations in the references above.

- **External Radiotherapy**: Also known as teletherapy is a technique where a source placed at a distance from the patient is used to irradiate the tumor in order to destroy the cancerous cells. It is the most commonly recommended modality for treating cancer. In the next phase, we will be discussing more about the different techniques in external radiotherapy. External radiotherapy offers a cost effective technique for treating cancer as its cost represents about 5% of the total cost of cancer care [24]. It is recommended as part of treatment in almost half of all cancer cases [25]. The importance of external radiotherapy to cancer treatment cannot be underestimated and for this reason this study focuses in more detail about the radiotherapy technique in the next sections.

1.4 External Radiotherapy

External radiotherapy makes use of high energy radiation (electrons or photons) coming from linear accelerators to kill tumor cells. Here we can remark a difference between a treatment that is carried out using incident electrons called *electron beam therapy* and a treatment done using photons called *photon beam therapy* but the same machine is capable of producing both forms of radiation when slight adjustments are made. This machine is called the Linear Accelerator.

1.4.1 The Linear Accelerator

The Linear accelerator, also called LINAC [19] [1], is an equipment used to produce mega voltage radiation which can penetrate deep into the body to kill deep-sited tumors. The linear accelerator produces electrons through thermionic emission, then uses a high frequency travelling or stationary microwaves to accelerate them to produce radiation with more energy and better penetrating power. The block diagram of the linear accelerator is shown in figure 1.1:

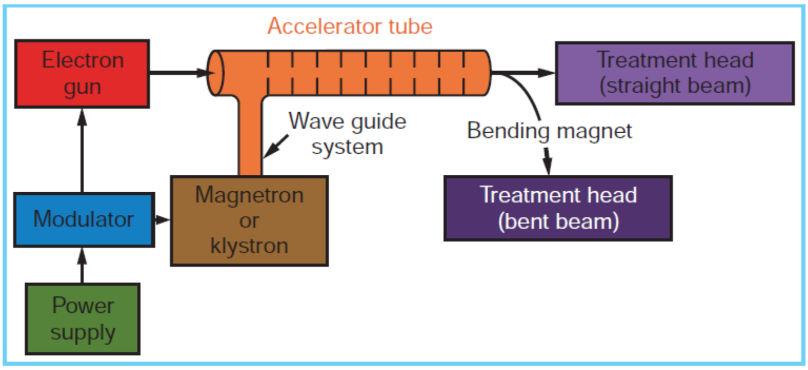

Figure 1.1 – Block Diagram of a Linear accelerator [1]

A thermionic source is heated to produce electrons in the electron gun. These electrons are accelerated using high frequency microwaves of up to 3000Mhz produced in a klystron tube and transmitted via a waveguide. The microwaves used for the acceleration of the electrons could be standing waves or travelling waves. The LINAC could be used to produce lower energy mega voltage beams (< 8 MeV) using an electron accelerator that is positioned perpendicular to the axis of rotation of the gantry and medium or higher energy mega voltage beams (>8-10 MeV) when the electron accelerator is positioned parallel to the axis of rotation of the gantry [26].

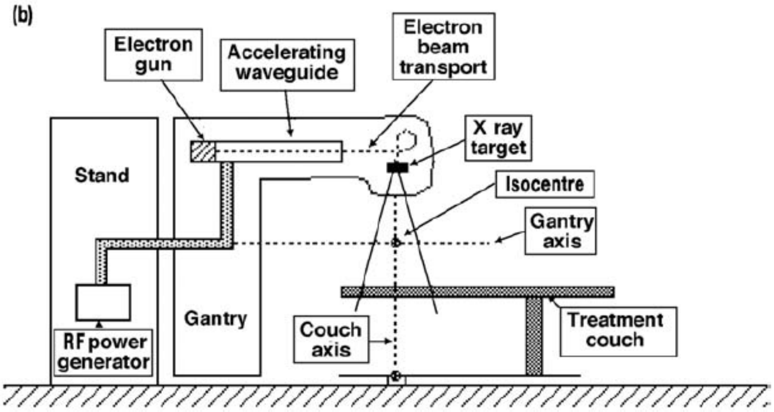

Figure 1.2 – Structure of the Linear accelerator [2]

Figure 1.2 shows an example of the LINAC, highlighting some important parts such as:

- **Multileaf Collimators:** Multileaf collimators (MLC) are used to perform the shaping of the radiation beam. The MLC leaves are made up of leaves which can move independently in order to produce any beam shape [19]. The design of the MLC has to provide sufficient mechanical gap so that the leaves can move freely but this could also lead to a leakage of radiation. Some MLC manufacturers have designed MLC leaves to have a curved profile to prevent radiation leakage. The position control of these leaves produces a field shape that is adapted to the shape of the tumor at each plane thus enabling greater accuracy and control of the radiation dose. Better smoothing of the field shape and edges can be achieved through the use of mini and micro MLCs. An example of an MLC can be seen in figure 1.3

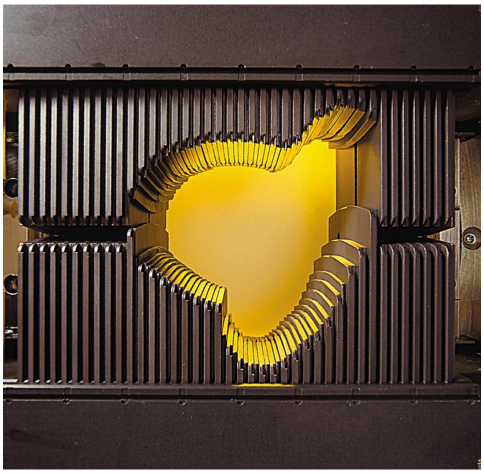

Figure 1.3 – A 120-leaf Multi-leaf collimator [3]

- **Gantry:** This is a mobile unit that carries the accelerator unit while rotating about an axis parallel to the horizontal plane of the treatment room. This enables the central axis of the radiation beam from the collimator to rotate about a horizontal axis at a point, called the *isocenter*, where both the central axis of the beam and the axis of rotation of the gantry intersect.
- **Couch:** The patient undergoing treatment lies on a treatment table that is also called a couch whilst the radiation beams are active. The patient could also be immobilized on this couch to prevent motion that may cause the radiation beams to deviate and strike unwanted parts of the body during treatment.

1.4.2 Treatment planning for External Radiotherapy

Treatment planning refers to methods used to plan treatments for external radiotherapy. When a patient is diagnosed with cancer, a certain quantity of radiation dose is prescribed by the doctor. Treatment planning is performed to determine the parameters of the irradiation equipment that will deliver the prescribed dose to the patient. Such parameters include: the number of beams, their orientations, their shapes and the intensity of the radiation. All these parameters determine the final dose recieved by the patient and the distribution of the dose to the different parts of the patient. We note that some methods are more applied in certain treatment centers and other methods used elsewhere depending on the installed equipment manufacturer, skills available and specialty of the treatment required.

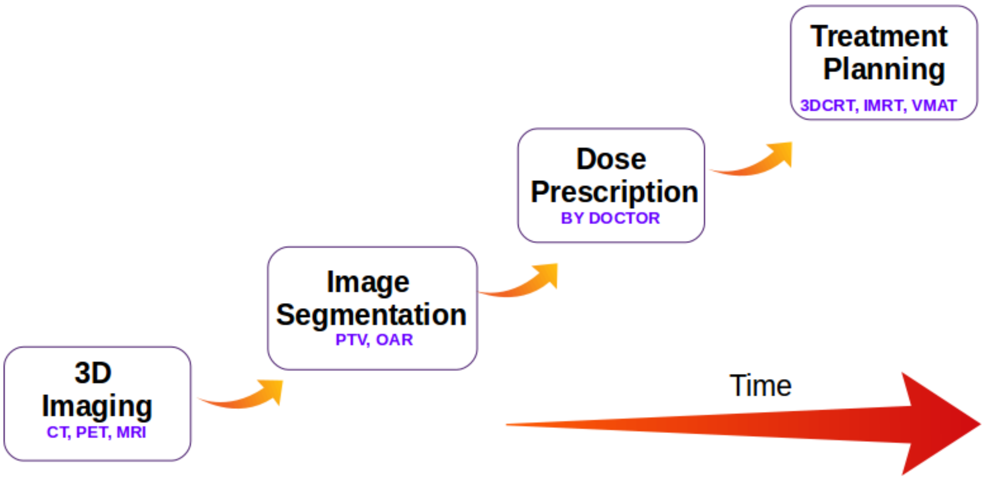

Figure 1.4 – Steps in radiotherapy up to treatment planning stage

Before treatment planning is performed, a 3D image of the patient tumor is acquired using techniques such as computed tomography (CT) [27], positron emission tomography (PET) [28] or magnetic resonance imaging (MRI) [29]. Image segmentation is performed to localize the tumor and the organs-at-risk within the patient. A prescription dose to be recieved by the cells within the tumor is then given by the doctor to be used to prepare the treatment plan. These steps are illustrated in figure 1.4.

Previously, treatment methods relied on the intuition of the radiation oncologists and physicists to decide the appropriate treatment plan for a cancer patient. Developments in equipment components, modern computing and algorithm design have given rise to advanced techniques such as that enable the computation of optimal treatment plan specific to a patient. Such techniques include: three-dimensional conformal radiotherapy (3D-CRT), intensity-modulated radiotherapy (IMRT) and volumetric modulated arc therapy (VMAT). Other advancements have enabled non-coplanar treatment techniques especially in IMRT and VMAT. In the next section, we will make a brief recall on the aforementioned treatment planning methods and then make a much deeper study into the non-coplanar VMAT treatment planning.

1.4.3 Three-dimensional conformal radiotherapy (3D-CRT)

Three-dimensional conformal radiotherapy is an image based treatment planning performed with the aim of conforming (wrapping around) a prescribed dose to the planning target volume while minimizing the dose to the surrounding tissues [4]. This methodology became popular in the 1970s with the advent of 3D medical imaging capabilities such as computed tomography (CT) allowing the treatment planner to perform treatment planning and evaluation using 3D data.

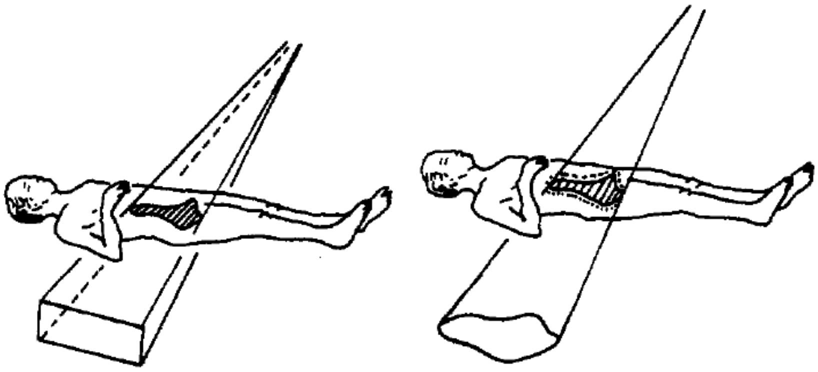

Figure 1.5 – Image showing improvements to dose shaping achieved using 3D-CRT. Treatment on the left uses conventional radiotherapy giving a rectangular shape that is undesirable for sensitive organs while treatment on the right uses 3D conformal therapy to conform the shape of the dose to the shape of the tumor [4]

The 3D anatomical information of the patient is used to localize and delineate the tumor. Beams are manually chosen by the treatment planner then the dose and the beam's-eye-view are calculated. The beam's-eye-view is a view through which the patient tumor can be observed from the origin of the beam moving along its central axis [4]. The effect of using the beam's-eye-view is that the field of treatment conforms to a projection of the volume of the tumor at the MLC. 3D-CRT is an improvement that saw the introduction of beam shaping into radiotherapy treatment over the previously used rectangular field shaping as seen in figure 1.5. 3D-CRT employs a forward planning process to determine the dose distribution from a set a radiation beams as illustrated in figure 1.6. However, the beam selection for 3D-CRT is done manually leading to treatment plans that are not optimal.

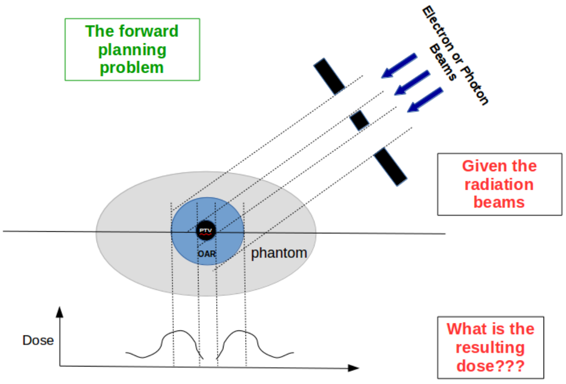

Figure 1.6 – Illustration of the forward planning process

1.4.4 Intensity-modulated radiotherapy (IMRT)

Intensity modulation radiotherapy (IMRT) is a treatment planning technique where beams of non-uniform radiation intensity are used for tumor irradiation in order to achieve a conformal dose distribution. The IMRT technique makes use of radiation beams of modulated intensity as illustrated in figure 1.7. This property differentiates IMRT from 3D-CRT which makes use uniform intensity beams. The modulation of beam intensity is made possible in IMRT by the sub-division of a beam into beamlets. A single beamlet is a subset of a radiation beam created using a grid that subdivides the beam into several smaller units. The smaller the size of the beamlet, the better the amount of shielding to the organs-at-risk during treatment [30] [31]. The increase or decrease of the intensity of individual beamlets is used to achieve modulation.

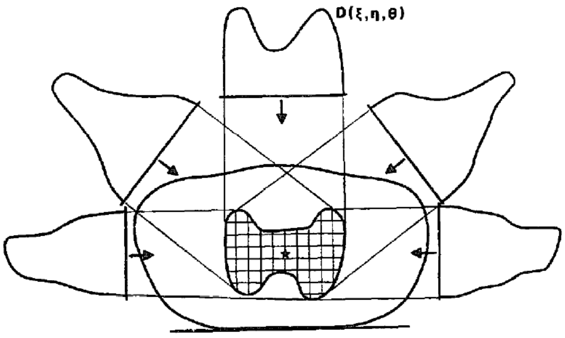

Figure 1.7 – Image showing the modulation of radiation intensity for IMRT for better organ-at-risk avoidance. The different radiation beam profiles are used to target different regions of interest [5]

An improvement in dosimetry has been observed using IMRT compared to 3D-CRT in patient cases where the planning treatment volume is concave and located close to sensitive organs. IMRT enables the delivery of a concave shaped dose distribution around the target tumor cells. In IMRT, the intensity of the rays passing through the sensitive organs are reduced while the intensity of the rays passing through the tumor is increased to achieve modulation. The non-uniform radiation intensities used in IMRT are calculated by an inverse planning process as illustrated in figure 1.8.

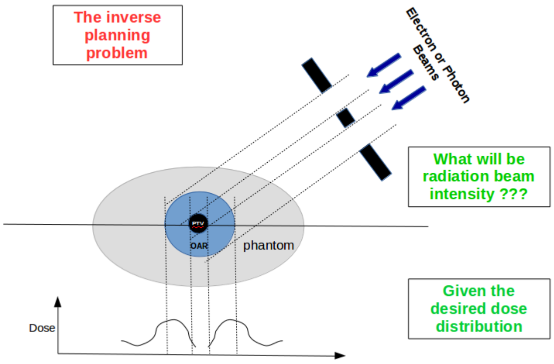

Figure 1.8 – Illustration of the inverse planning process

The inverse planning in IMRT is to determine the radiation intensity distribution from a prescribed dose distribution. IMRT is usually formulated as a fluence map optimization problem (FMO) [5]. This is because it is difficult to obtain an exact solution that delivers the full prescription dose to the tumor without any dose to the sensitive organs [32]. After the IMRT optimization sequencing if done to convert the fluence intensities into actual MLC leaf shapes that can be delivered by the LINAC machine [33].

IMRT is generally delivered of two forms, fixed-gantry IMRT and rotational IMRT. Many techniques for the delivery of IMRT which has been developed over the years such as NOMOS MIMiC [34], multiple-static-field MLC technique [35], Dynamic MLC technique [36], step-and-shoot delivery technique [37], helical tomotherapy [38], robotic IMRT [6] and intensity modulated arc therapy (IMAT) [39] which came to be known as volumetric modulated arc therapy (VMAT). Since the introduction of LINACs capable of a rotational delivery intensity-modulated fields, VMAT has seen wide-spread clinical use [40]. However most published studies on VMAT focus on its clinical properties while studies on the underlying mathematical optimization and impementation are still scarce [41]. This is the reason why we focus this study on VMAT technique.

IMRT presents the advantages of being able to use beams of different intensities to deliver shaped doses to different parts of the patient tumor. This reduces the possibility of the re-population of tumor cells. But the planning and quality assurance processes for IMRT are complex compared to 3D-CRT. IMRT could use higher MU than conventional radiotherapy [42]. The sequencing process performed after the fluence map optimization for IMRT could result in a degraded plan if there is a difference between the dose planned and the dose delivered. We detail the fluence map optimization formulation in section 1.4.4 as we will make several references to it in this thesis. More detailed review on the historical developments on IMRT can be found in [43].

Fluence map optimization (FMO)

The fluence map optimization is used to determine the beamlet intensities to be used for treatment in IMRT. Given the 3D CT image of a cancer patient, the entire volume is composed of a set of voxels denoted as $\mathbb{V}$ and the incident radiation beam denoted as b is composed of a set of beamlets.

The dose is received by a voxel $j \in \mathbb{V}$ is denoted as d_j and the intensity of an incident beamlet $i \in b$ of fluence intensity is denoted as x_i. $\mathbb{B}$ denotes the set of beam angles that are selected for the VMAT treatment plan such that $b \in \mathbb{B}$. The dose influence matrix, $\mathbf{D}$, expresses the relationship between the dose recieved by a voxel d_j and a beamlet of unit fluence intensity x_i, such that:

$$d_j = \sum_{i \in b} D_{ji} x_i \tag{1.4}$$

$$\mathbf{D} = \begin{bmatrix} D_{1,1} & D_{1,2} & \dots & D_{1,i} \\ \vdots & \vdots & \ddots & \vdots \\ D_{j,1} & D_{j,2} & \dots & D_{j,i} \end{bmatrix}_{nv \times nb}, \quad \mathbf{x} = \begin{bmatrix} x_1 \\ \vdots \\ x_i \end{bmatrix}_{nb \times 1}, \quad \mathbf{d} = \begin{bmatrix} d_1 \\ \vdots \\ d_j \end{bmatrix}_{nv \times 1} \tag{1.5}$$

where nv is the number of voxels in the patient and nb is the number of the beamlets used in the treatment. $\mathbf{D}$ is usually a large and sparsely populated matrix. It is calculated using finite pencil beam methods [44] or monte carlo methods [45]. Given a dose prescribed by the physician $\mathbf{d}^p$ to be delivered to the tumor, the objective is to minimize the least-square deviation between the prescribed dose and the actual dose received by the tumor voxels. The objective function is:

$$f(\mathbf{d}) = \frac{1}{N_t} \sum_{j \in V_t} p^+ (d_j - d_j^p)^2 + \frac{1}{N_o} \sum_{j \in V_o} p^- (d_j - d_j^p)^2 \tag{1.6}$$

where $V_t \subset \mathbb{V}$ denotes the tumor voxels with cardinality $|V_t| = N_t$ and $V_o \subset \mathbb{V}$ denotes the organ-at-risk voxels with cardinality $|V_o| = N_o$. p^+ is a penalty factor for controlling the relative importance of the target tumor voxels and p^- is the penalty factor for controlling the relative importance of organ-at-risk voxels. The fluence map optimization writes:

$$\begin{aligned} &\underset{\mathbf{x}}{\operatorname{argmin}} \, f(\mathbf{d}) \\ &subject\ to: \\ &\qquad \mathbf{x} \geq \mathbf{0} \end{aligned} \tag{1.7}$$

The choice of the objective function $f(\mathbf{d})$ is not unique. Linear or Quadratic objective functions can be used to reflect a clinician's desired dosimetric objectives. A detailed review of the possible formulations of the fluence map optimization depending on the objective function or the constraints can be found in [46]. The positivity constraint ($\mathbf{x} \geq \mathbf{0}$) is imposed on the beamlet intensity solution $\mathbf{x}$ because it is physically impossible to deliver radiation of negative intensity.

Solution to Fluence map optimization problem

Key considerations for the choice of optimization algorithm to solve the FMO problem include the number of iterations required, memory considerations, region of convergence, complexity of the algorithm and number of parameters required. Below, we highlight two methods to solve the fluence map optimization problem.

Newton method with line search

The newton method is a popular technique to solve optimization problems where the objective function is convex and differentiable. At the initial stage, the beamlet intensity vector is initialized $\mathbf{x}_0 \in R_+$. At each iteration, k, the descent step direction $\mathbf{m}$ and a step size α_k, is used to update the beamlet intensity vector $\mathbf{x}_{k+1}$ until the minimum of the objective function is reached[47]. The pseudocode for the newton method is illustrated in algorithm 1. The beamlet intensity vector at step $k + 1$ is given as:

$$\mathbf{x}_{k+1} = \mathbf{x}_k + \alpha_k \mathbf{m} \tag{1.8}$$

Where $R_+(\mathbf{x}) = max(0, \mathbf{x})$ is the poitivity operator. The newton method approximates the next iteration's objective function value using a Taylor series expansion of the current objective function value using:

$$f(\mathbf{x}_{k+1}) = f(\mathbf{x}_k + \delta\mathbf{x}) \approx f(\mathbf{x}_k) + \mathbf{g}_k^T \delta\mathbf{x} + \frac{1}{2}\delta\mathbf{x}^T \mathbf{H}_k \delta\mathbf{x} \tag{1.9}$$

where $\mathbf{g}$ is the first derivative of the objective function and $\mathbf{H}$ is the symmetric Hessian matrix or the second derivative given as:

$$\mathbf{g}_k = \nabla f(\mathbf{x}_k) = \begin{bmatrix} \frac{\partial f}{\partial x_1} \\ \vdots \\ \frac{\partial f}{\partial x_i} \end{bmatrix}, \ \mathbf{H}_k = \mathbf{H}(\mathbf{x}_k) = \begin{bmatrix} \frac{\partial^2 f}{\partial x_1^2} & \cdots & \frac{\partial^2 f}{\partial x_1 \partial x_i} \\ \vdots & \ddots & \vdots \\ \frac{\partial^2 f}{\partial x_i \partial x_1} & \cdots & \frac{\partial^2 x_1}{\partial x_i^2} \end{bmatrix} \tag{1.10}$$

At the minimum of the objective function, $\nabla f(\mathbf{x}_k) = 0$ so that :

$$\nabla f(\mathbf{x}_k) = \mathbf{g}_k + \mathbf{H}_k \delta\mathbf{x} = \mathbf{0} \tag{1.11}$$

And then we can obtain the descent step for the next iteration as:

$$\delta\mathbf{x} = -\mathbf{H}_k^{-1}\mathbf{g}_k = \mathbf{m} \tag{1.12}$$

$$\mathbf{x}_{k+1} = \mathbf{x}_k - \mathbf{H}_k^{-1}\mathbf{g}_k \tag{1.13}$$

Newton methods are known to be fast for smaller problem applications especially when the current solution is near the minimum. If we consider the objective function given in equation 1.7, its first order derivative can be expressed as:

$$\nabla f(\mathbf{d}) = \mathbf{D}^T(\frac{2p^+}{N_t}(d_j - d_j^p) + \frac{2p^-}{N_o}(d_j - d_j^p)) \tag{1.14}$$

A line search is usually applied to the newton method to obtain an adequate step size to guarantee convergence. A backtracking line search that applies Armijo's rule could be used [48]. In the backtracking line search, the new objective function value is imposed to be smaller than an estimated objective function found using the relation:

$$f(\mathbf{x}_k) - c.\alpha_k.\ \mathbf{g}_k^T\mathbf{m} < f(\mathbf{x}_k + \alpha_k\mathbf{m}) \tag{1.15}$$

Algorithm 1 Newton method aplied to solve FMO

```
Init :  $\mathbf{x}_0 \,; k = 0 \,; \tau \in (0.5, 0.6) \,; c \in (0,1) \,; \epsilon = 10^{-6} \,; \mathbf{m}_0 \in (\mathbf{0},\mathbf{1}) \,; \alpha_0 > 0$
while (true) do
    $\mathbf{m} = -\mathbf{H}_k^{-1}\mathbf{g}_k$
    $\alpha_k = 1$
    while $(f(\mathbf{x}_k + \alpha_k\mathbf{m}) \leq f(\mathbf{x}_k) + c.\alpha_k.\mathbf{g}_k^T\mathbf{m})$ do
        $\alpha_k = \alpha_k.\tau$
    end while
    $\mathbf{x}_{k+1} = \mathbf{x}_k + \alpha_k.\mathbf{m}$
    project $\mathbf{x}_{k+1}$ to $\mathbb{R}_+^{nb}$ and $f_{k+1}(\mathbf{d})$ using 1.4 and 1.6
    compute $\mathbf{H}_k^{-1}$ and $\mathbf{g}_k$ using 1.10
    if $(||\mathbf{g}_k|| < \epsilon)$ then
        break
    end if
    $k = k + 1$
end while
return $\mathbf{x}_{k+1}$
```

The newton method assumes that the Hessian matrix is positive definite with eigen-values greater than zero. If this assumption does not hold, the newton method could fail and might even become unstable. For application to FMO problems, it is preferable to avoid the calculation of the hessian matrix or its storage at each iteration due to the large size of the problem. This will enable the generation of a treatment plan in a reasonable amount of time. To overcome the challenge of calculating the hessian, quasi-newton methods can be used.

Quasi-Newton methods

Quasi-newton methods are able to avoid the computation of the second-order derivative of a vector function by approximating the hessian matrix [49]. A popular quasi-newton method for solving FMO problems is the L-BFGS method [50]. L-BFGS is a limited-memory quasi newton method that can successfully solve large problems involving non-sparse hessian matrices. L-BFGS approximates the hessian by storing a few vectors and then using the curvature information of the most recent iteration to construct the hessian approximation. The quasi-newton method differs in its strategy for computing the descent direction 1.13. At each step in the L-BFGS method, the inverse of the hessian matrix is approximated using the vectors:

$$\mathbf{s}_{k+1} = \mathbf{x}_{k+1} - \mathbf{x}_k \tag{1.16}$$

$$\mathbf{y}_{k+1} = \mathbf{g}_{k+1} - \mathbf{g}_k \tag{1.17}$$

These vectors are then stored as illustrated in 1.18 and used for subsequent computations.

$$\mathbf{S} = \begin{bmatrix} \mathbf{s}_1 & \dots & \mathbf{s}_m \end{bmatrix}_{nb \times m} \quad \mathbf{Y} = \begin{bmatrix} \mathbf{y}_1 & \dots & \mathbf{y}_m \end{bmatrix}_{nb \times m} \quad \rho = \begin{bmatrix} \frac{1}{\mathbf{s}_1^T \mathbf{y}_1} & \cdots & \frac{1}{\mathbf{s}_m^T \mathbf{y}_m} \end{bmatrix}^T_{m \times 1} \tag{1.18}$$

The pseudo-code for the quasi-newton method is show in algorithm 2 and 3.

Algorithm 2 Quasi-Newton method applied to FMO (L-BFGS)

```
Init :   $\mathbf{x}_0$ ; $k = 0$ ; $\tau \in (0.5, 0.6)$ ; $c \in (0, 1)$ ; $\epsilon = 10^{-6}$ ; $\mathbf{m}_0 \in (\mathbf{0}, \mathbf{1})$ ; $\alpha_k > 0$
while (true) do
    $\mathbf{m} = -\mathbf{H}_k^{-1}\mathbf{g}_k$
    $\alpha_k = 1$
    while  $(f(\mathbf{x}_k + \alpha_k \mathbf{m}) \leq f(\mathbf{x}_k) + c.\alpha_k.\mathbf{g}_k^T \mathbf{m})$  do
        $\alpha_k = \alpha_k.\tau$
    end while
    $\mathbf{x}_{k+1} = \mathbf{x}_k + \alpha_k.\mathbf{m}$
    project $\mathbf{x}_{k+1}$ to $\mathbb{R}_+^{nb}$ and $f_{k+1}(\mathbf{d})$ using 1.4 and 1.6
    compute $\mathbf{g}_k$ using 1.10
    if ($||\mathbf{g}_k|| < \epsilon$) then
        break
    end if
    compute $\mathbf{s}_{k+1}$ and $\mathbf{y}_{k+1}$ using 1.16 and 1.17
    store $\mathbf{s}_{k+1}$ and $\mathbf{y}_{k+1}$ using1.18
    $\mathbf{H}_{k+1}^{-1}$ = HessianUpdate($\mathbf{H}_k^{-1}, \mathbf{S}, \mathbf{Y}, \rho$) using Algorithm 3
    $k = k + 1$
end while
return $\mathbf{x}_{k+1}$
```

Algorithm 3 **HessianUpdate($\mathbf{H}_k^{-1}, \mathbf{S}, \mathbf{Y}, \rho$)**

```
Require : $\mathbf{H}_k^{-1}, \mathbf{S}, \mathbf{Y}, \rho$;
for $j = 1, ..., m$ do
    $\mathbf{U}_j = \mathbf{I} - \rho_j \mathbf{y}_j \mathbf{s}_j^T$
    $\mathbf{V}_j = \rho_j \mathbf{s}_j \mathbf{s}_j^T$
    $\mathbf{H}_k^{-1} = \mathbf{U}_j^T \mathbf{H}_k^{-1} \mathbf{U}_j + \mathbf{V}_j$
end for
return $\mathbf{H}_k^{-1}$
```

Beam angle selection

In IMRT treatment planning, a number of beams have to be chosen to be used for treatment before the fluence map optimization is performed using these beam angles. The beam angle selection (BAS) problem is to find the optimal beam orientations, at which the patient will be irradiated, to be used in treatment planning. The optimal beams are the beams that intersect with the target tumor region and do not come in contact with the OAR(s). Given a set of candidate beam orientations **B**, the beam angle selection problem is to find an optimal set of beam orientations $\mathbf{b}^*$ for patient treatment such that:

$$\mathbf{b}^* \subseteq \mathbf{B} \tag{1.19}$$

The beam angle selection problem in equation 1.19 is a non-convex combinatorial problem with many local minima [51] and consequently NP-Hard [52]. Two categories of approaches can be distinguished:

- One way is to solve the beam angle selection and fluence map optimization problems simultaneously. In the first step a technique is used to select the beam combination and in the next step the FMO problem is solved to evaluate the resulting plan. The beam combination that results from the best plan is then chosen as the optimal. Such methods include simulated annealing [53] [54] [55], genetic algorithms [56], [57], mixed integer programming [58] [59] and exhaustive search [60] [61].

- Another method is to use previous information of the beam angle combination to generate a new beam angle combination and then to carry out the fluence map optimization in the final step. Such methods include: iterative methods [62] [63], geometric methods [64] [65] [65], ranking methods [66] [67] [68] and clustering methods [69]. There are also approaches that make use of proximal gradient methods for beam selection [70]. Here a term is included in the objective function that penalizes the l_1 norm of the fluence intensity solution vector and thus induce sparsity.

The fluence map optimization for beam selection has to be solved as many times as the number of different beam combinations evaluated which leads to long computation times. Large amounts of dose influence data must be stored and transferred to and from the computer random access memory (RAM) when needed during calculation. Many different approaches have been proposed in literature but there are no clear studies that make a comparison of the different approaches in order to determine the best. Nonetheless, automated beam angle selection has shown dosimetric improvements over manual selection of beams.

1.4.5 Volumetric modulated arc therapy (VMAT)

Volumetric modulated arc therapy (VMAT) is an IMRT delivery technique that involves the continuous rotation of the gantry while the radiation beam is on during patient irradiation [71]. In step-and-shoot IMRT, the gantry is fixed at each orientation where radiation is delivered, leading to an increased usage of monitor units (MU) for treatment. VMAT overcomes this problem by using a continuously rotating gantry during treatment thus delvering lower monitor units on the whole. The lower monitor units recieved by the patient results in a significant improvements in organ-at-risk sparing e.g.a lower dose on the skin.

VMAT allows a variation in different machine parameters such as dose rate, gantry speed, and MLC leaf positions during irradiation. VMAT differs from 3D-CRT in the sense that the treatment beam does not have to conform to a shape of the tumor. The motion of the gantry is approximated as a change in the angular distance $\delta\theta$ between two adjacent radiation beams. We denote a single radiation beam orientation as a *control point*. The motion of the MLC leaves between two control points is approximated as a change in the length δd of the MLC. Restrictions are placed on the motion of the MLC leaf and fluence intensity between two control points so that they are not too dissimilar. The optimization for VMAT is more challenging than other forms of IMRT due to the inclusion of machine parameters in the optimization [72]. Table 1.1 makes a comparison to illustrate the important differences between VMAT, IMRT and 3DCRT.

VMAT is more time efficient and produces a conformal dose distribution of equal or superior plan quality compared to IMRT. The parameters for the VMAT optimization depends on the target LINAC equipment on which the plan is delivered. Modern Linear accelerators have the ability to vary the dose rate, the gantry speed and the MLC apertures simultaneously thereby lending themselves for use in VMAT delivery. We can distinguish two main methods to perform VMAT optimization, aperture-based method and leaf trajectory VMAT method.

Table 1.1 – Comparison between different radiotherapy techniques

Metric	**3DCRT**	**IMRT**	**VMAT**
Uses Patient 3D Imaging	Yes	Yes	Yes
Uses Intensity Modulated Beams	No	Yes	Yes
Uses Optimized Beams	No	Yes	Yes
Optimizes Machine Parameters	No	No	Yes

Aperture-based VMAT method

This refers to the use of the aperture shape of the MLC leaves to compute the fluence intensity at each control point. These methods start out by solving a fluence map optimization on a number of control points sampled at a coarse discretization. The fluence intensities are subsequently converted into apertures in a process called *arc sequencing* [33]. Finally, the resulting apertures are used as a starting point to solve a direct aperture optimization (DAO) [73]. The control points for the DAO are sampled at a finer discretization and the aperture shape and aperture intensity is determined at each control point.

The different aperture-based VMAT methods differ mainly in the approach to solving the DAO problem such as: column-generation methods [74] [75], local DAO initialized with apertures obtained from FMO [76] [77] [78] and global DAO approach [71] [79]. We do not explicitly detail the formulation for direct aperture optimization as it is not used in this thesis. A good review of the different approaches can be found in [72].

The difficulty with the aperture-based method is that the DAO formulation requires the calculation of the gradient of the objective function with respect to the machine parameters which is difficult to obtain. The gradient of the objective function with respect to the shape of the MLC leaf shape is non-convex and many authors make assumptions or use heuristic methods to overcome this problem. Most VMAT algorithms that use this formulation are not published and their implementation are not available in open source making comparison a difficult task. Finally the three-step process of FMO, arc-sequencing and DAO increases the sources of errors and approximations.

Leaf trajectory VMAT method

This method computes the fluence intensity by optimizing the trajectory of the MLC leaf according to an objective function. This method was proposed as direct leaf trajectory optimization [80]. The direct leaf trajectory optimization computes the fluence intensity as a function of the time at which an MLC leaf arrives to and departs from a beamlet. A number of arc segments, where the MLC leaf moves unidirectionally, are used to generate a fluence map which closely resembles an ideal IMRT plan. The formulation is detailed in section 1.4.5. This direct leaf trajectory optimization approach directly optimizes the piecewise linear MLC leaf trajectories giving rise to a formulation that is convex under certain assumptions.

Direct leaf trajectory optimization

The direct leaf trajectory optimization was proposed to generate a deliverable VMAT plan in a single step by directly optimizing the leaf trajectory of the multileaf collimator [80]. It is written as:

$$\min_{\mathbf{x}} f(\mathbf{d}) \tag{1.20a}$$

$$subject\,to:\ d_j = \sum_{k=1}^{k=K}\sum_{n=1}^{n=N}\sum_{i=1}^{i=I} D^k_{jni}x^k_{ni} \quad \forall \quad j,\ n,\ i, \tag{1.20b}$$

$$x^k_{ni} = \delta . t^k_{ni} \tag{1.20c}$$

$$t^k_{ni} = \frac{1}{2}(l^{out}_{kni} - r^{out}_{kni} + l^{in}_{kn(i+1)} - r^{in}_{kn(i+1)}) \quad \forall \quad k,\ n,\ i \tag{1.20d}$$

$$0 \le r^{in}_{kni} \le r^{out}_{kni} \le \frac{t^{max}}{K},\ 0 \le l^{in}_{kni} \le l^{in}_{kni} \le \frac{t^{max}}{K} \tag{1.20e}$$

$$r^{out}_{kni} + \Delta t \le r^{in}_{kn(i+1)},\ l^{out}_{kni} + \Delta t \le l^{in}_{kn(i+1)} \tag{1.20f}$$

$$r^{in}_{kni} \le l^{in}_{kni},\ r^{out}_{kni} \le l^{out}_{kni} \tag{1.20g}$$

- where d_j is the dose in voxel j.
- $n \in N$ and $i \in I$ are the row and column indices respectively in the intensity matrix of an exposed beamlet at control point $k \in K$.
- n also corresponds to the row index of MLC leaf pair.
- D^k_{jni} is an element in the dose influence matrix **D**. It denotes dose contribution to voxel j from unit intensity of beamlet (n,i) at the control point k. Each control point k corresponds to a column in matrix **D** and each beamlet (n,i) corresponds to a row in this matrix.
- δ is the machine dose rate in MUs^{-1}.
- t^k_{ni} is the exposure time for beamlet (n,j) in secs at beam k, t^{max} is total delivery time.
- t^k_{max} is the maximum allowed exposure time for all beamlets in beam k
- r^{in}_{kni} and l^{in}_{kni} denote the time at which the right and left leaf on row n to arrive beamlet (n,i) respectively
- r^{out}_{kni} and l^{out}_{kni} denote the time at which the right and left leaf on row n to depart beamlet (n,i) respectively.

Equation 1.20 enables us to optimize the delivery time directly and thus determine the MLC leaf trajectory in a single step. The MLC leaf arrival and leaf departure time at each beamlet, which define the leaf trajectory, are the variables being optimized under this formulation. The model also takes into account the leaf constraints such as maximum MLC leaf speed, minimum MLC leaf motion per degree. The direct-leaf trajectory method for VMAT optimization avoids the two-step approach to VMAT seen in literature [77] [81] that can compromise treatment plan quality when fluence intensities are converted to leaf positions by arc-sequencing. The optimization problem is also convex under this formulation, leading to solutions that can be obtained from available convex optimization solvers.

Below we will explain the constraints 1.20c -1.20g. Equation 1.20c defines the beamlet intensity as a product of the dose rate of the machine and the beamlet exposure time. Equation 1.20d is used to calculate the beamlet exposure time for all exposed beamlet from the arrival and departure times of the left and right MLC leaf. Equation 1.20e is a constraint for the ordering of the leaf arrival and departure times so that, for the left and right leaves in a row index, the departure time from a beamlet is always greater than the arrival time and positively bounded to a maximum exposure time period t^k_{max}. Equation 1.20f is a constraint on the maximum leaf speed moving from one beamlet to the next. Equation 1.20g keeps the arrival and departure times of the right MLC leaf behind the arrival and departure time of the leading left leaf.

Gradient of the objective function

We provide an expression for the gradient of our objective function in matrix notation by expanding equations 1.20b - 1.20d. We define a beamlet exposure vector **v** which is the variable of optimization and contains the leaf arrival and departure time for each beamlet. We also define an aperture matrix **M** that performs the linear mapping between the fluence intensity space **t** and the beamlet exposure space **v**. Thus enabling equation 1.20d to be rewritten in matrix notation into equation 1.22.

$$\mathbf{v} = \begin{bmatrix} \mathbf{l}^{out}_{nb\times 1} \\ \mathbf{r}^{out}_{nb\times 1} \\ \mathbf{l}^{in}_{nb\times 1} \\ \mathbf{r}^{in}_{nb\times 1} \end{bmatrix}, \mathbf{M} = \begin{bmatrix} \mathbf{I}_{nb\times nb} & -\mathbf{I}_{nb\times nb} & \mathbf{S}_{nb\times nb} & -\mathbf{S}_{nb\times nb} \end{bmatrix} \tag{1.21}$$

$$\mathbf{t} = \mathbf{Mv} \tag{1.22}$$

$$\delta_{i,j} = \begin{cases} 1, & \text{if } i = j \\ 0, & \text{if } elsewhere \end{cases} \tag{1.23}$$

$$\mathbf{I}_{i,j} = \delta_{i,j} \tag{1.24}$$

$$\mathbf{S}_{i,j} = \delta_{i+1,j} \tag{1.25}$$

If we define δ_{ij} as the Kronecker delta function as equation 1.23, we can find expressions for **I** which is the identity matrix as in equation 1.24 and **S** which is the upper shift of the identity matrix as in equation 1.25. So the beamlet intensity defined in equation 1.20c can be rewritten in matrix notation:

$$\mathbf{x} = \delta.\mathbf{t} \tag{1.26}$$

The matrix notation enables us to write the gradient of the objective function as:

$$\nabla f(\mathbf{d}) = \mathbf{D}^T(\frac{2p^+}{N_t}(d_j - d^p_j) + \frac{2p^-}{N_o}(d_j - d^p_j)) \tag{1.27}$$

Definition of Upper bound for exposure time

Direct leaf trajectory optimization requires an upper bound for the exposure time t^k_{max} as seen in constraint 1.20e at each control point k. For our implementation, we define the maximum exposure time as the time it takes the trailing multileaf collimator leaf to leave the furtherest exposed beamlet. This is obtained using the limit position of the left and right leaf of each row of the multileaf collimator in the beam-eye-view (BEV) aperture to determine the maximum time leaf traversal time in each row. The relationship is obtained using:

$$\mathbf{t}^{k}_{row} = \frac{\mathbf{l}_{max} - \mathbf{r}_{max}}{s_{leaf}} \tag{1.28}$$

where $\mathbf{t}^{k}_{row}$ is a vector of the traversal time of each row of multileaf collimator leaf pairs that have their beamlets exposed, $\mathbf{l}_{max}$ and $\mathbf{r}_{max}$ are the limit positions (mm) of the left and right leaves in the BEV aperture and s_{leaf} is the leaf speed.

The upper bound for the exposure time is calculated by a summation of the time taken by the slowest multileaf collimator pair at a control point and the time taken to move from one control point to the next.

$$t^{k}_{max} = max(\mathbf{t}^{k}_{row}) + \frac{\Delta\Theta_{k,k+1}}{g_s} \tag{1.29}$$

where $\Delta\Theta_{k,k+1}$ is the angular distance from one control point to the next and g_s is the angular speed of the gantry. For this thesis, it is assumed that the couch moves at the same speed as the gantry for all VMAT optimizations performed.

1.4.6 Coplanar vs Non-coplanar VMAT

Originally, VMAT planning was performed using a rotating gantry with the patient couch fixed to 0° in what can be referred to as coplanar VMAT. A very recent and promising technique is the use of non-coplanar trajectories for VMAT treatment planning [82]. In non-coplanar VMAT, the gantry carrying the radiation beam and the patient couch rotate simultaneously to change the radiation beam orientation. A comparison of the space of candidate beam orientations used for coplanar and non-coplanar treatments can be see in figure 1.9.

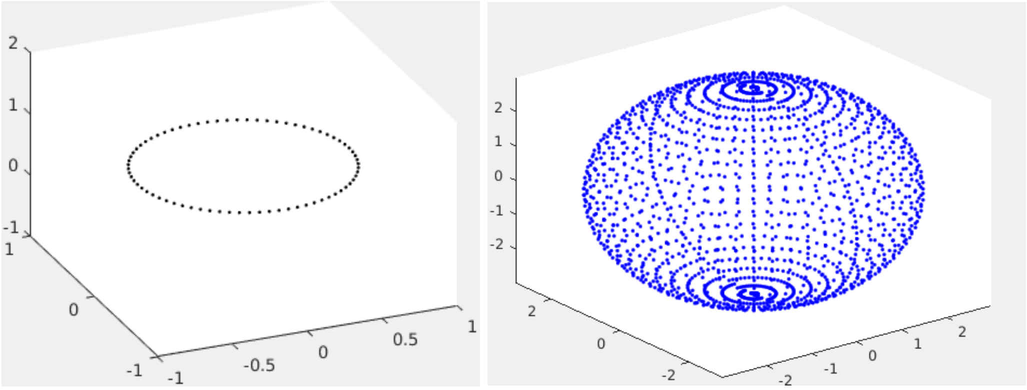

(a) (b)

Figure 1.9 – Comparing the space of candidate beam orientations (a) Coplanar orientations (b) Non-coplanar orientations

Non-coplanar VMAT is made possible with the introduction of LINACs capable of a dynamic motion of the couch and gantry. This makes it possible to create non-coplanar VMAT trajectories around the patient thus increasing the number of orientations available for irraditation [83]. More recently has seen the introduction of specialized robotic assisted irradiation equipment such as the CyberKnife [6]. The CyberKnife system consists of a 6 degree-of-freedom (DOF) robotic positioning arm carrying a 6MV linear accelerator mounted and integrated with X-ray imaging and visualisation feedback systems. The CyberKnife posesses a high degree of flexibility and is able to follow highly dynamic trajectories to cover the 4π space around the patient as shown in figure 1.10.

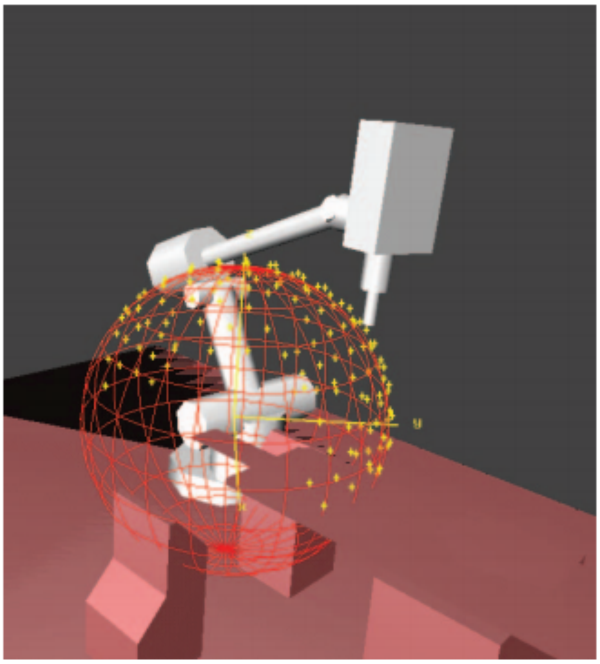

Figure 1.10 – The use of CyberKnife to cover 4π space around the patient [6]

Several authors have argued that non-coplanar VMAT could lead to superior treatment plans and should be used more extensively in tretament planning [84]. Conceptually, the non-coplanar beam geometry is a superset of the coplanar beam geometry and therefore should yield treatment plans of superior dosimetry. A major advantage is that non-coplanar VMAT can achieve better organ-at-risk avoidance by orienting the radiation beams in a different geometric plane relative to the patient [85] [86] [77] [83]. A non-coplanar trajectory consists of evenly or unevenly spaced combinations of couch-gantry orientations along which the patient will be irradiated. We can distinguish three main methods in literature for performing non-coplanar VMAT planning on the basis of the motion of the couch or gantry i.e fixed-couch method, fixed-gantry method and dynamic couch-gantry method.

Fixed-couch non-coplanar VMAT method

This method makes use of a combination of a fixed patient couch orientation and a dynamic gantry rotation for non-coplanar VMAT treatment. The author in [87] uses four non-coplanar arcs at a fixed non-coplanar couch rotation for treating twelve patients with intracranial lesions.

A similar approach is seen in [88] for treating fifteen patients with brain metastases, for sixteen patients with sinonasal cancers [89] and for twenty patients treated using liver stereotactic body radiation therapy (SBRT) [90]. In all cases, a comparison to a coplanar VMAT plan showed better OAR sparing.

One weakness of this fixed-couch approach is that the definition of the treatment trajectory is manually done and thus varies from one treatment planner to the other. Indeed the author reports that *"The arc length or gantry span of each arc was adjusted to avoid organs-at-risk when possible"*. Such a method for selecting non-coplanar trajectory is not repeatable when a different tumor geometry is presented or when a different planner performs the trajectory selection. Also, the entire space of possible couch-gantry orientation combination is not explored to select the most optimal trajectory with respect to the treatment objectives. These were the earliest applications of non-coplanar VMAT treatment planning.

Fixed-gantry non-coplanar VMAT method

This method uses a combination of a dynamic couch rotation and a fixed gantry orientation for non-coplanar VMAT treatment. This approach was used for accelerated partial breast irradiation (APBI) in [91]. The APBI aims to irradiate only a portion of the lumpectomy cavity at a margin with as little as possible dose to the surrounding tissues of the breast, heart and lungs. The study was carried out using a fixed gantry and rotating couch on twelve breast cancer patients showed a reduction of the maximum dose to the breast, lung and heart. Such a technique increases the possibility of collision between the gantry and the couch. Lateral couch translations would then have been used to avoid collisions thereby increasing planning complexity. The dynamic couch fixed gantry combination produces a discontinuous and non-isocentric beam trajectory which is unsuitable for tumor most locations in the body. The search space for the optimal control points for irradiation is also severely limited.

Dynamic couch-gantry non-coplanar VMAT method

This method uses a combination of a dynamic couch rotation and a dynamic gantry rotation to perform non-coplanar VMAT treatment. In this way, there is increased degree of freedom and consequently a greater flexibility to obtain optimal control points for patient irradiation [92, 85, 86, 77, 93, 94, 95, 96].

We can distinguish geometric methods that use the beam's eye view (BEV) information [85, 86, 94, 96, 95]. The geometric methods assign a score to each beam orientation in relation to the tumor's shape and a search algorithm is used to determine a non-coplanar trajectory through the lowest scoring beams. The geometric methods differ in the search algorithm they employ such as hierarchical clustering [85], Djikstra's algorithm [86, 94] or A^* [96, 95]. The advantage of these geometric methods is that they offer a fast way to choose beam angles that form part of the non-coplanar VMAT treatment trajetory.

The author in [86] uses dynamic couch rotation for planning VMAT treatment for four patient cases: brain, breast, prostate and pelvic nodes. A graph-search algorithm was used to find a minimum cost trajectory through a cost map scored from beamlet-OAR intersections. The results showed significant reductions in the mean dose to the OARs in all four cases considered when compared to a coplanar VMAT plan. Similar geometric methods applied in [85] use non-coplanar VMAT for treating fifteen patients with tumors located close to the central nervous system. A geometric overlap score is calculated at each control point from the BEV projection of the OAR and tumor. A hierarchical clustering algorithm combined with graph-search is used to generate a VMAT treatment planning trajectory from control points with minimum overlap scores. Their results show a improved dose conformity to the tumor and a lower maximum dose to OARs like brainstem, optic nerves and chiasm compared to coplanar VMAT plans for the same patients. The geometric methods have drawbacks in that the cost function is obtained from geometric relations and does not incorporate the dosimetric objectives. The geometric methods may fail to generate a continuous trajectory in patient cases where all irradiation trajectories traverse the OARs. The trajectory obtained is dependent on the initial patient set-up and the same set-up will need to be reproduced prior to treatment delivery to avoid errors.

Other authors have formulated the trajectory determination for dynamic non-coplanar VMAT plan as a beam angle selection problem [77] [93]. The advantage of the beam selection is that a dosimetric evaluation of a combination of beams is performed which is not done using geometric methods. The author in [77] uses a genetic algorithm to perform beam angle selection and then solves DAO on the selected control points to generate the treatment plan for three nasopharyngeal patients. They compare the non-coplanar VMAT plan trajectories to plan trajectories obtained using coplanar IMRT and non-coplanar IMRT as well as coplanar VMAT. Their results show an average reduction of 19% of the mean and maximum doses to the OARs with a similar mean dose to the target tumor.

Another method is to use a gradient norm strategy for beam angle selection as seen in [93]. The gradient norm of each control point is used to select a few promising control points and then a trajectory is generated to connect this control points by solving a travelling salesman problem. A VMAT plan is then generated along this non-coplanar trajectory using direct leaf trajectory optimization. As we have noted in section 1.4.4 the beam angle selection is a non-convex, combinatorial optimization problem which is computationally expensive. The author in [93] performs only a limited exploration of the beam angle space to overcome this problem and no solution is proposed to overcome the non-convexity. Moreover, there is a possibility to be stuck in a local minima when using the gradient norm strategy and therefore generate trajectories that are not globally optimal.

The NoVo method [95] determines the noncoplanar VMAT trajectory by combining a geometric scoring technique with a beam angle selection based on fluence elimination. A path finding algorithm based on A^* was used to find a continuous trajectory through the most promising beam angles that were identified after beam scoring. The results from the NoVo method show more than a 50% reduction in the computation time compared to other methods, but the dosimetric improvements that can be obtained using this method is not very evident.

The methods that employ beam angle selection for non-coplanar trajectory determination may produce treatment plans of high quality but with trajectories that can be sub-optimal [82]. This is due to the fact that when the selected control points are linked up to form a complete trajectory, intermediate control points have to be included. Some control points selected by the beam selection algorithm may also be very far from each other and a path to connect the two points may traverse an OAR. Some authors have tried to evaluate the dosimetry of the entire trajectory rather than a few optimal control points. The author in [94] combines beam angle selection with direct apertutre optimization by introducing a sparsity term in the objective function. A graph search algorithm is then used to determine the resulting trajectory corresponding to the shortest path on a djikstra's graph of the selected optimal control points. The algorithm alternates between the beam angle selection combined with DAO and the trajectory generation until there is no change in the trajectory. The treatment plan prepared with this method showed reductions to the mean and maximum OAR dose compared to a coplanar VMAT plan for nine patients with brain, lung, or prostate cancer. In non-coplanar VMAT, when a number of beams have been chosen for treatment, it is important to create a trajectory that allows to visit each beam orientation once during the motion of the gantry and couch. A travelling salesman problem is usually solved to achieve this.

Traveling Salesman Problem (TSP)

Given a set of nodes on a directed edge-weighted graph, the Travelling Salesman Problem (TSP) is to find a minimum cost trajectory which visits all the nodes on the graph and returns to the first node [97, 98, 99]. The TSP corresponds to finding the Hamiltonian cycle or the minimum cost cyclic path that visits every node once on a directed edge-weighted graph. The use of TSP to create a trajectory is illustrated in figure 1.11.

By formal definition, if we consider an edge-weighted, directed graph $G = (N, E, \mathbf{W})$ with nodes $N = \{n_1, n_2, \ldots, n_N\}$, with directed edges $E \subseteq V \times V$ and $\mathbf{W}(n_i, n_{i+1})$ is a matrix of costs between the nodes. The traveling salesman problem is to find a Hamiltonian cycle $H^N = \{n_1, n_2, \ldots, n_N\}$ that satisfies the criteria in equation 1.30.

$$D(H^N) = \sum_{n=1}^{n=N_{n_{N+1}=n_1}} W(n_i, n_{i+1}) \longrightarrow minimum \tag{1.30}$$

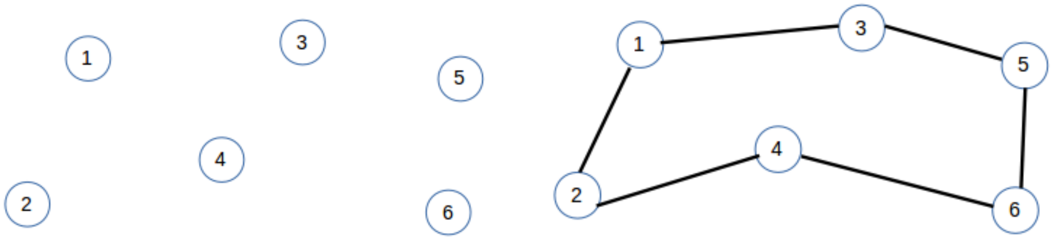

(a) (b)

Figure 1.11 – Solving the Traveling Salesman Problem to create a minimum cost trajectory to connect the nodes in figure (a), the final trajectory is shown in figure (b)

The traveling salesman problem is a combinatorial optimization problem and are considered to be NP-hard. The TSP has been applied to overhauling gas turbine engines [100], vehichle routing [101], observation of space-based satellite systems [102]. In radiotherapy treatment planning, TSP is applied to determine a feasible non-coplanar treatment trajectory that connects the optimal beam angles selected during BAS [103, 77, 93, 94].

Several strategies exist for solving the TSP such as dynamic programming [104], genetic algorithm, branch-and-bound method [105], greedy heurisitc [106], nearest neighbour heuristic [106], insertion heuristic [106], christofides algorithm [107]. A more exhaustive list of the methods that can be used to solve the traveling salesman problem can be found in [99].

The choice of the cost function for defining matrix **W** between the nodes depends on the application. Usually for finding a shortest path between nodes, the euclidean distance is used as a cost function.

The author in [93] uses TSP solved by integer programming method to create the final beam trajectory for non-coplanar VMAT. The cost function is defined as the shortest distance to reposition the couch and gantry angle from one beam orientation to the other (equation 1.31). This implies that between two couch-gantry positions (c_1, g_1) and (c_2, g_2) the cost is measured in degrees.

$$\mathbf{W}(1,2) = max(\mid c_1 - c_2 \mid, \mid g_1 - g_2 \mid) \tag{1.31}$$

Another author [77] uses TSP for creating the beam trajectory in non-coplanar VMAT. In this case, the cost function is defined as the time to move from one couch-gantry angle combination to the next. Genetic algorithm is applied to solve the traveling salesman problem in this case.

Non-coplanar VMAT shares the same issues inherent in other non-coplanar techniques such as: increased complexity, greater risk for collision, longer treatment times and longer radiation trajectories that lead increased cumulative dose [84]. Another difficulty of this method is that the optimization has to be performed along the entire VMAT trajectory rather than on a few control points giving rise to very large problem sizes.

1.5 Thesis Objective Statement

The use of dynamic couch-gantry trajectories significantly enhances the degree of freedom and flexibilty available for non-coplanar VMAT treatment planning. This offers an opportunity for more precise and accurate delivery of radiation during cancer treatments. Non-coplanar VMAT has the potential to treat tumors that are located in close proximity of critical organs or that are partially surrounded by normal tissues. It also offers an opportunity for a more efficient treatment delivery through by using a lower amount of monitor units. The lower usage of monitor unit results in a faster treatment delivery time and less inconvenience for the patient. Despite the improvements that have been seen in non-coplanar VMAT, challenges still persist.

The first problem is that the dynamic motion of the patient couch and gantry significantly increases the risk of collisions during treatment. It is important to find a way to eliminate this risk of collisions during non-coplanar VMAT treatment. A method is required to identify and remove collision-prone orientations before the treatment planning stage. Such a method has to be fast, automated and easy to reproduce in any radiotherapy treatment center.

The cumulative dose received by the tumor and its distribution also depends on the orientation of the beams used for treatment. There is a significant increase in the number of possible solutions to the non-coplanar VMAT problem due to the exploration of a 4π space. The second problem is to find a method to select the best possible beam orientations for the accurate delivery of the prescribed dose. Existing methods for non-coplanar VMAT limit the search space for the optimal beam orientations to avoid this problem. This is due to the large size and the combinatorial nature of the problem but leads to local solutions. There is a need to define a criteria for selecting the optimal beam orientations from a large number of possible beam orientations without limiting a priori the search space available at the initial stage.

The third problem we have identified is the need to create a trajectory that accounts for the dosimetric property of each beam orientation that forms part of the trajectory. Existing methods for non-coplanar VMAT insert intermediate beams orientations after performing beam selection and thereafter proceed to solve a travelling salesman problem. This is done when the neighbouring optimal beams are far from each other and intermediate beam orientations are inserted to create a valid trajectory. This approach is prone to introducing errors in the dosimetry. The inserted beams contribute a dose that is not accounted for in the original optimization. This could lead to an excessive dose being delivered to the patient during treatment. There is a need for a non-coplanar VMAT approach that evaluates the dosimetry of the entire trajectory to ensure that it constitutes a deliverable plan that respects the dosimetric objectives.

From the three main limitations identified in the state-of-art methods, this thesis proposes improvements to collision detection, global optimization and trajectory generation for non-coplanar VMAT treatment planning. This thesis will present the suggested improvements for non-coplanar VMAT treatment planning in three main chapters.

Chapter 2 will presents a methodology for the determination of collision free couch-gantry orientations. This methodology is proposed to avoid the possibility of a collision during the motion of the couch and gantry. The method is based on detecting the forces that may result from a collision between the couch and the gantry at each orientation during treatment. The dynamics of the treatment equipment are simulated at each orientation using precise 3D computer-aided design (CAD) models of the LINAC equipment. A dynamic co-simulation is performed using MATLAB [108] and ADAMS [109] which are easily obtainable software tools. The methodology is applicable at any other radiotherapy treatment center irrespective of the type of equipment installed. The chapter starts with a brief introduction to review the exisiting collision detection methods. A detailed description is used to show how the proposed method can be reproduced by other researchers. A simulation example is presented and the results are discussed.

In Chapter 3 we present the algorithm for non-coplanar VMAT treatment planning formulated as a beam selection problem. This algorithm is proposed to solve the problem of defining a criteria for selecting globally optimal beam orientations for non-coplanar VMAT treatment planning. The new algorithm combines direct leaf trajectory optimization and a beam selection using simulated annealing. Direct leaf trajectory optimization is employed to overcome the problems of aperture based methods such as obtaining the gradient of the objective function with respect to the machine parameters. Simulated-annealing is employed for beam angle selection to ensure that globally optimal beam orientations are obtained due to the combinatorial nature of the problem. A travelling salesman problem is used to determine the final trajectory to connect the selected beams. A comparison to the state-of-the-art is performed to show the improvements that can be achieved with this algorithm. The chapter starts with a brief introduction and description of the simulated annealing algorithm and its use for treatment planning. The algorithm is presented with a description of what each step is designed to achieve. The results of a study carried out with different patient cases are presented and the comparison to other state-of-the art approaches is discussed at the end of the chapter.

Chapter 4 presents the sampling-based algorithm for generating the trajectory for the non-coplanar VMAT plan delivery. The algorithm is proposed to solve the problem of the addition of intermediate beam orientations observed in beam selection methods. The algorithm is inspired from rapidly exploring random trees (RRT^*). It proceeds by sampling the space of candidate beam orientations and creating a tree structure for the discovered beam orientations. The algorithm performs the minimization of a dosimetric objective function along each trajectory consisting of a branch from a newly discovered node on the tree to the root node of the tree. The chapter begins with a brief introduction on the use of sampling-based algorithms in radiotherapy and (RRT^*) . The formulation of the algorithm is detailed in the subsequent section and the different functions employed are explained. A study to evaluate the algorithm is presented and a comparison is made to the previously presented simulated annealing method. Another comparison is made with a state-of-the-art method and afinal comparison is made to coplanar VMAT approach. We discuss the results and propose some improvements that can be made to this approach.

Finally, the last chapter discusses the proposed methods and concludes on the obtained results. Perspectives for the future improvements are suggested and the difficulties encountered during this research are emphasized.

CHAPTER

2

COLLISION DETECTION FOR NON-COPLANAR VMAT

A methodology for collision detection is presented in this chapter. The dynamics of the LINAC equipment at each orientation are simulated using it's precise 3D computer-aided design (CAD) model in a simulation software called ADAMS. A co-simulation is performed between ADAMS and MATLAB in order to detect collision prone couch-gantry configurations. An experiment is peformed using the real LINAC equipment to verify the results of the simulation. The experimental results show an accurate detection of collision prone couch-gantry configurations.

2.1 Introduction

Most linear accelerator equipment vendors have incorporated the possibility to perform simultaneous couch and gantry motion thereby making non-coplanar treatment a possibility. A major concern when using non-coplanar trajectories during treatment is the possibility that a collision between the couch carrying the patient and the gantry could occur. Such a collision can lead to an injury to the patient, an inaccurate delivery of the planned treatment or an equipment damage. It is clear that collisions are highly undesirable and must be detected and eliminated if the treatment goals have to be met.

Early approaches to collision detection during radiotherapy treatment planning made the use of collision indicator charts [110]. The collision indicator charts was used by treatment planners to identify the couch and gantry configurations that can lead to a collision-free treatment delivery. This method for collision detection was used when beam design was performed manually and the selected beams were sub-optimal. As automated techniques for beam selection were introduced, the need for optimized beams and automatic collision detection increased.

Room-eye-view approach to collision detection can be see in the work [111]. The author measures the geometric dimensions of the radiotherapy equipment and uses this measurement to approximate different parts of the equipment to known geometric shapes. Collisions are detected when test points defined on the gantry head fall into the geometric shapes representing the patient or couch. A detected collision prints a warning message and the treatment planner has to peform adjustment manually. This results in a cubersome process of taking measurements, choosing appropriate shapes for the different parts of the radiotherapy equipment. If the equipment is changed, the measurements have to be retaken to perform collision calculations for the new equipment. Only a few number of points were chosen for the analytical computation collision detection limiting the accuracy. This method for collision detection is not automated limiting it's usefulness.

Another room-eye-view approach to collision detection is seen in the work [112] by performing a graphical simulation using a 3D scaled representation of the couch, the gantry and the patient. The collisions are detected by checking if an intersection exists between the triangulated vertices of the 3D models. It is evident that this method requires extensive computation when all vertices of the 3D model to check for collision by using triangular intersection. The software proposed cannot easily accept a large input data of different couch gantry angle combinations or communicate with other software components.

Another way to perform collision detection is by the use of surface imaging [113]. The surface imaging technique involves the use of a Kinect camera [114] to acquire an image of the patient and the radiotherapy equipment in the form of a 3D point cloud [113]. The collision free distance between the gantry and the patient couch is defined as a clearance cylinder. The collisions are detected by identifying the points that lie outside the clearance cylinder. One advantage of this approach is that it enables the simultaneous real-time capture of scene objects and collision detection. The collision between the patient and the LINAC can also be easily checked with this method as the patient model is created in real-time. One drawback here is the possibility of the existence of blind spots where the camera does not scan objects in the scene completely. This results in an incomplete point cloud representation of the patient or treatment equipment leading to errors in collision detection.

A more recent proposal for collision detection which has been implemented for the open-source radiotherapy research toolkit SlicerRT [115] can be seen in the work of [116]. The author uses a collision detection filter implemented in SlicerRT to check for collisions between couch and gantry using 3D models that have been imported into SlicerRT. One limitation of this approach is that each gantry and couch angle combination to be checked has to be inputed manually leading to a cumbersome process. If we imagine a 6° discretization on a 4π space the operation could involve about 3600 candidate couch-gantry angles. In a similar way, when a collision is detected, the process for removing the corresponding couch-gantry configuration is not automated.

For our application, we require an automated method for collision detection that is fast and easy to integrate into our workflow for selecting non-coplanar beam angles. This is to avoid having to test each individual gantry-couch combination manually. We require a method that can obtain input beam angles easily from another software component and deliver output in a common format. One problem we found in literature is that the software used for collision detection are not open-source and sometimes difficult to obtain, not sufficiently maintained or even obsolete in some cases. Our proposition has to make use of software that is easily obtainable, continuosly maintained to make for easier comparison.

Considering these factors, we propose a method for collision detection for non-coplanar radiotherapy based on performing a dynamic co-simulation to detect contact forces using MATLAB [108] and ADAMS [109]. Both software are easily obtainable and well known within the research community. The proposed approach can be reproducible in other radiotherapy treatment centers thereby allowing for better comparison of results. Our method also offers possibility to change the 3D models to that of a specific radiotherapy equipment being employed at a particular treatment clinic while avoiding cumbersome measurements. The input candidate angles are very easy to generate in MATLAB and subsequently sent to the collision detection engine in real-time without need for manual input. Finally we note the speed of this approach enables us to obtain the collision-free couch-gantry angles for treatment in clinically feasible time.

2.2 Geometric Setup

We make use of the 3D CAD model of the LINAC equipment by Varian Trubeam obtained from the work of [116]. This 3D model is the same as the Varian Trubeam LINAC installed at the radiotherapy treatment clinic, CHRU Brest. This 3D model was chosen to enable an easier comparison of the simulated model to the real equipment. The 3D model is obtained as a *.stl* file, a format that can be read by most common 3D dynamics simulation engines. The component parts of the 3D model are imported into ADAMS a 3D dynamic simulation engine [109] and assembled following the IEC-61217 standards for radiotherapy equipment [117]. The different parts of the 3D model imported into ADAMS before assembly can be visualized in figure 2.1.

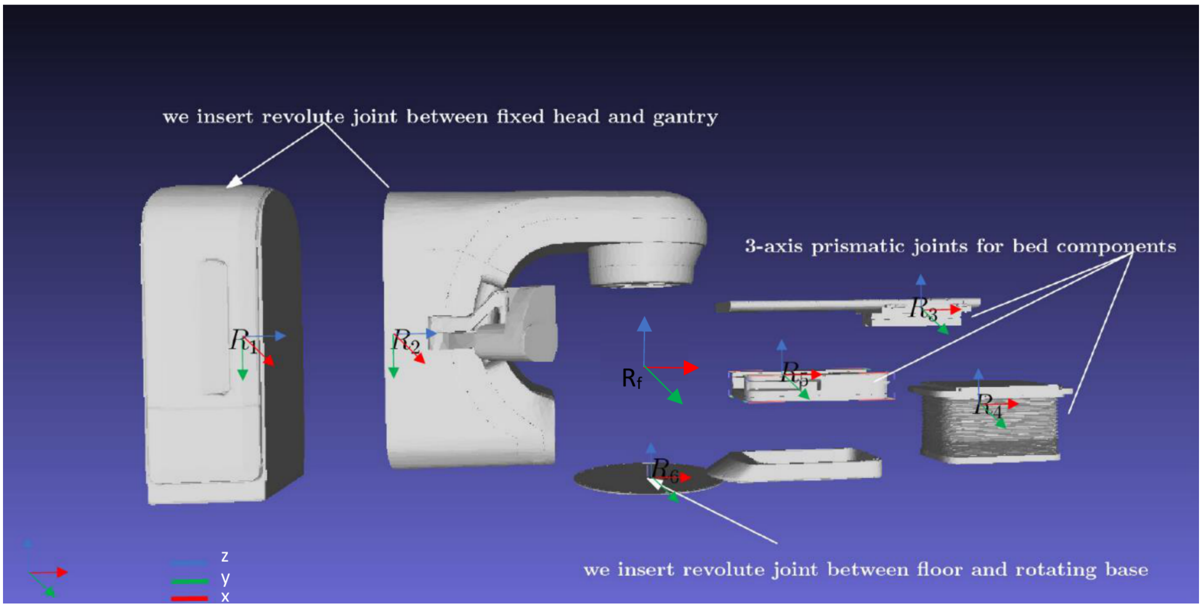

Figure 2.1 – 3D CAD models of the different parts of a radiotherapy equipment showing the different frames attached to each body with the axis colred x (red), y (green), z (blue)

The isocenter is denoted by frame R_f in figure 2.1 and is located at $1295mm$ along the vertical measured from the center of the cicular base for the Varian Trubeam. The isocenter constitutes the origin of the reference frame within ADAMS enviroment. The gantry (fig 2.1 parts 1 & 2) makes use of a local co-ordinate system R_1 in figure 2.1 which differs from the reference frame.

Joint 1 located at the origin of frame R_1 in figure 2.1 is a revolute joint which rotates anti-clockwise around z-axis of the local frame attached the gantry. Joint 1 is introduced between the fixed head (fig 2.1 part 1) and the rotating gantry (fig 2.1 part 2). The transformation between the reference frame and the local frame attached to the gantry is taken into account for the assembly of Joint 1.

The rotation matrix that defines the orientation of Joint 1 with respect to reference frame ${}^{gantry}\mathbf{R}_f$ is given as:

$$ {}^{gantry}\mathbf{R}_f = \begin{bmatrix} cos(\pi) & -sin(\pi) & 0 \\ sin(\pi) & cos(\pi) & 0 \\ 0 & 0 & 1 \end{bmatrix} \begin{bmatrix} 1 & 0 & 0 \\ 0 & cos(\frac{\pi}{2}) & -sin(\frac{\pi}{2}) \\ 0 & sin(\frac{\pi}{2}) & cos(\frac{\pi}{2}) \end{bmatrix} \begin{bmatrix} cos(\frac{\pi}{2}) & -sin(\frac{\pi}{2}) & 0 \\ sin(\frac{\pi}{2}) & cos(\frac{\pi}{2}) & 0 \\ 0 & 0 & 1 \end{bmatrix} \tag{2.1} $$

Thus for a gantry rotation of $\phi°$ is

$$ {}^{gantry}\mathbf{R}_f(\phi) =^{gantry} \mathbf{R}_f . \begin{bmatrix} cos(\phi) & -sin(\phi) & 0 \\ sin(\phi) & cos(\phi) & 0 \\ 0 & 0 & 1 \end{bmatrix} \tag{2.2} $$

Joint 3 located at the origin of frame R_3 in figure 2.1 is a prismatic joint is introduced between the bed and the Base Interior. It moves along the x-axis of the reference frame in order to achieve longitudnal motion of the patient couch. The homogenuos transformation matrix that defines the position and orientation of Joint 3 with respect to the fixed reference frame is given as:

$$
{}^{f}\mathbf{T}_3 = \begin{bmatrix} 1 & 0 & 0 & P_x \\ 0 & 1 & 0 & 0 \\ 0 & 0 & 1 & 0 \\ 0 & 0 & 0 & 1 \end{bmatrix} \tag{2.3}
$$

Joint 4 located at the origin of frame R_4 in figure 2.1 is a prismatic joint between the vertical support and the base of the couch for linear motion along the z-axis of the reference frame. A change in the length of Joint 4 is used to vertically position the patient couch. The homogenuos transformation matrix that defines the position and orientation of Joint 4 with respect to the fixed reference frame is given as:

$$
{}^{f}\mathbf{T}_4 = \begin{bmatrix} 1 & 0 & 0 & 0 \\ 0 & 1 & 0 & 0 \\ 0 & 0 & 1 & -P_z \\ 0 & 0 & 0 & 1 \end{bmatrix} \tag{2.4}
$$

Joint 5 located at the origin of frame R_5 in figure 2.1 is a prismatic joint between the Base Interior and the vertical support for linear motion along the y-axis of the reference frame. The motion of Joint 5 achieves a lateral positioning of the patient couch. The homogenuos transformation matrix that defines the position and orientation of Joint 5 with respect to the fixed reference frame is given as:

$$
{}^{f}\mathbf{T}_5 = \begin{bmatrix} 1 & 0 & 0 & 0 \\ 0 & 1 & 0 & P_y \\ 0 & 0 & 1 & 0 \\ 0 & 0 & 0 & 1 \end{bmatrix} \tag{2.5}
$$

Joint 6 located at the origin of frame R_6 in figure 2.1 is a revolute joint which rotates anti-clockwise around the z-axis of the reference frame. Joint 6 is introduced between the base of the patient couch and the ground. The rotation matrix that defines the orientation of Joint 6 with respect to the fixed reference frame for a couch rotation of $\theta°$ is given as:

$$
{}^{f}\mathbf{R}_6(\theta) = \begin{bmatrix} cos(\theta) & -sin(\theta) & 0 \\ sin(\theta) & cos(\theta) & 0 \\ 0 & 0 & 1 \end{bmatrix} \tag{2.6}
$$

Therefore our simulated LINAC model has 5-degrees of freedom consisting of two rotations of the gantry and couch combined with three translations of the patient couch. We consider only these 5-degrees of freedom for this study. The linear motion of the couch along the three axis is used to align the tumor isocenter to the machine isocenter during patient positioning before treatment. The rotational motion of the couch and gantry are used to change the orientation of the beam during treatment. The entire colission detection setup can be seen in figure 2.2.

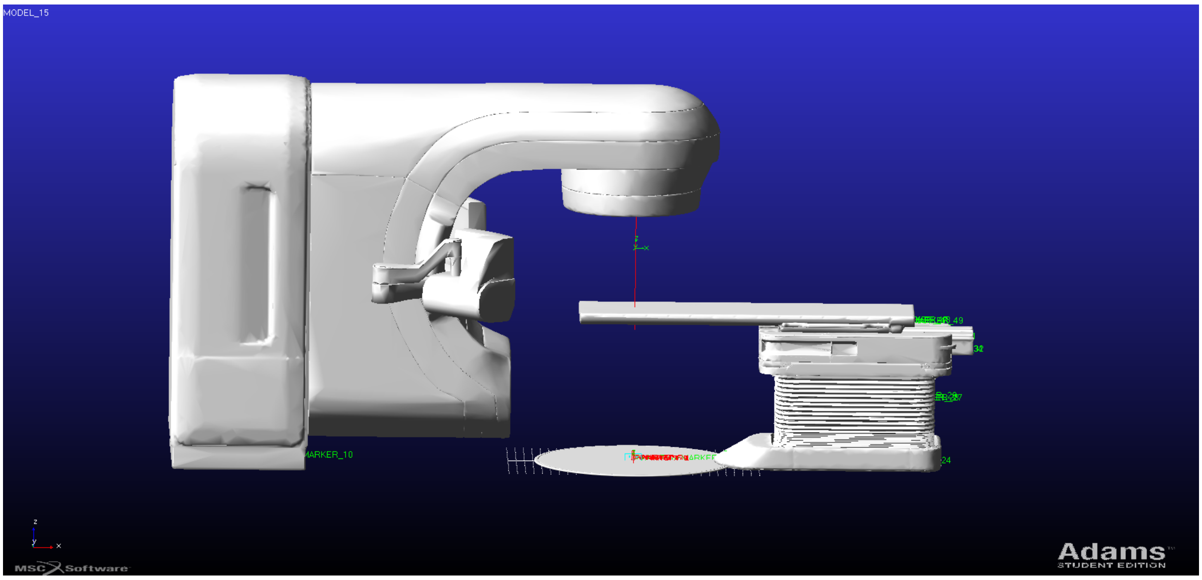

Figure 2.2 – Radiotherapy Treatment Setup in ADAMS

ADAMS allows us to measure shell-to-shell contact forces when two bodies collide in dynamic simulation. We create contact measurement elements in ADAMS between all component parts of the couch and gantry 3D models enumerated previously in figure 2.1. At each orientation, a force measurement element in ADAMS is used to detect whether or not there exists a collision between these component parts.

2.3 Co-simulation with MATLAB

The assembled model of the LINAC is exported as an ADAMS plant to MATLAB in the form of a simulink file model (.slx) as shown in figure 2.3. This plant has 2 inputs which are the couch and gantry angles and 6 outputs which are the contact force measure for each of the 6 parts of the simulated LINAC model. The prismatic joints values which position the patient couch are held constant during simulation and therefore fixed before the plant is exported. The couch and gantry revolute joint values vary during simulation and are recieved as input variables from MATLAB when the LINAC model is in simulation.

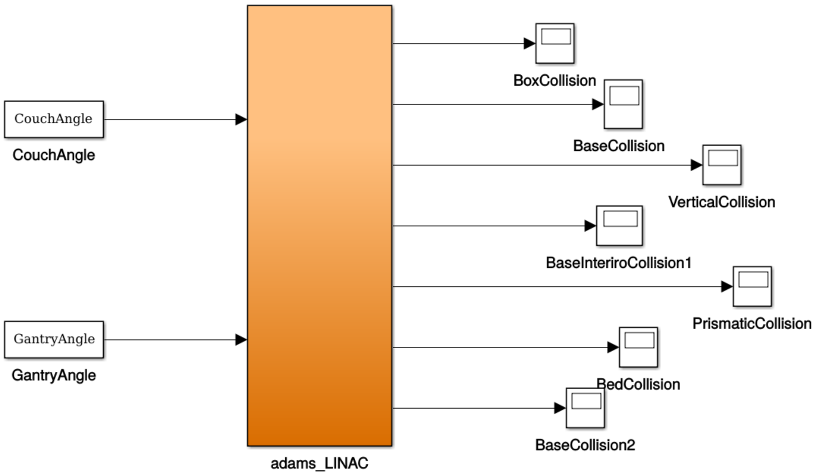

Figure 2.3 – Co-simulation for LINAC collision detection between MATLAB and ADAMS: Inputs to the ADAMS plant (left) are couch and gantry angles and Outputs (right) are collisions measured between the simulated bodies

The motion control of the simulated LINAC colission detection setup is performed using a MATLAB script. At each iteration, a couch-gantry angle pair is sent to the ADAMS plant from MATLAB by calling it's simulink model. The revolute joints attached to the couch and the gantry of the simulated LINAC in ADAMS are rotated according to the input angles. If any contact occurs between any of the bodies during this time period, a measurement of the contact force value in Newtons is recorded.

The ouput of the co-simulation is an array of measured contact forces. If there exists any component of the output array with a value greater than zero at a particular couch-gantry angle pair, this indicates the existence of a collision. This couch-gantry angle pair must then removed from the candidate set to be used for the treatment planning. The trajectory considerations moving from one couch-gantry angle pair to the next is not taken into consideration during this simulation. The analysis for each pair is done on an absolute basis so that the collision effect at one couch-gantry angle pair is not influenced by the collision effect of the previous couch-gantry angle pair.

2.4 Evaluation Study

To evaluate the proposed method, we perform a co-simulation using the 3D CAD model of a LINAC called the Varian Trubeam®. The results of the simulation are compared to the results from a real equipment of a similar model installed at the radiology section, Brest Regional University Hospital (CHRU). The aim of this evaluation study is to verify that collisions detected in simulation are the same on the real equipment. The couch angles θ and gantry angles ϕ are generated with a 5° discretization such that $-180^\circ \leq \theta, \phi \leq 180^\circ$ as shown in figure 2.4. To ensure stability in the simulation, we remove the angles in the sample where the solution to the dynamic model is undetermined notably $0^\circ, 180^\circ, 360^\circ$. All inputs can be collected in a set of couch-gantry input pairs $\mathbb{B}$. Iteratively, a pair of (θ_i, ϕ_i) is sent to the ADAMS plant from MATLAB. The three translational degrees-of-freedom of the treatment couch do not vary during this simulation and fix patient couch position to chosen value (P_x, P_y, P_z).

To verify the simulated collision detection, tests are carried out on the real LINAC equipment at different couch-gantry positions. The Developer Mode interface available on the LINAC enables the input of the test couch-gantry angles on the real equipment. Twenty couch-gantry angle pairs are chosen at random from all angles used for simulation to perform these tests. Each of the chosen couch-gantry pair is entered manually on the LINAC causing the LINAC to rotate the couch and the gantry to the desired configuration. A potential collision on the real equipment is signaled on the display and causes the machine to stop motion for safety reasons.

2.4.1 Results

The results of the simulation and verification studies are shown in the table 2.1. An example of such a test is shown in figure 2.7.

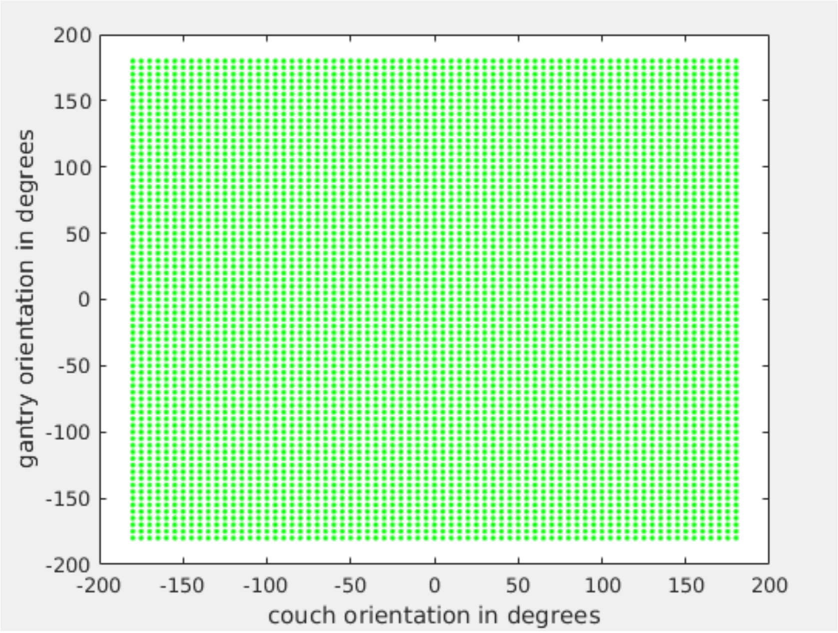

Figure 2.4 – Plot of the full workspace of the couch-gantry orientations

Table 2.7 compares the results of the collision detection tests carried out on the real LINAC equipment to the simulated results. No differences were observed in the collisions detected in the simulation and those observed in the real equiment. We note that a command to move the real LINAC equipment to an orientation that leads to collision causes the machine to stop before attaining this orientation to prevent eqipment damage. This comparison between the real and simulated equipment thereby validates the proposed method.

Table 2.1 – Collision Detection results comparing selected couch-gantry angle pairs simulated vs real equipment

Gantry Angle	**Couch Angle**	**Couch Vertical**	**Couch Lateral**	**Couch Longitudnal**	**Collision in Simulation**	**Collision on Real Equipment**
−80°	−95°	−29.67cm	112.35cm	0cm	True	True
15°	−60°	−29.67cm	112.35cm	0cm	False	False
75°	−25°	−29.67cm	112.35cm	0cm	False	False
135°	−10°	−29.67cm	112.35cm	0cm	True	True
−5°	15°	−29.67cm	112.35cm	0cm	False	False
70°	30°	−29.67cm	112.35cm	0cm	False	False
40°	40°	−29.67cm	112.35cm	0cm	False	False
−76°	65°	−29.67cm	112.35cm	0cm	False	False
−100°	80°	−29.67cm	112.35cm	0cm	True	True
73.9°	85°	−29.67cm	112.35cm	0cm	True	True

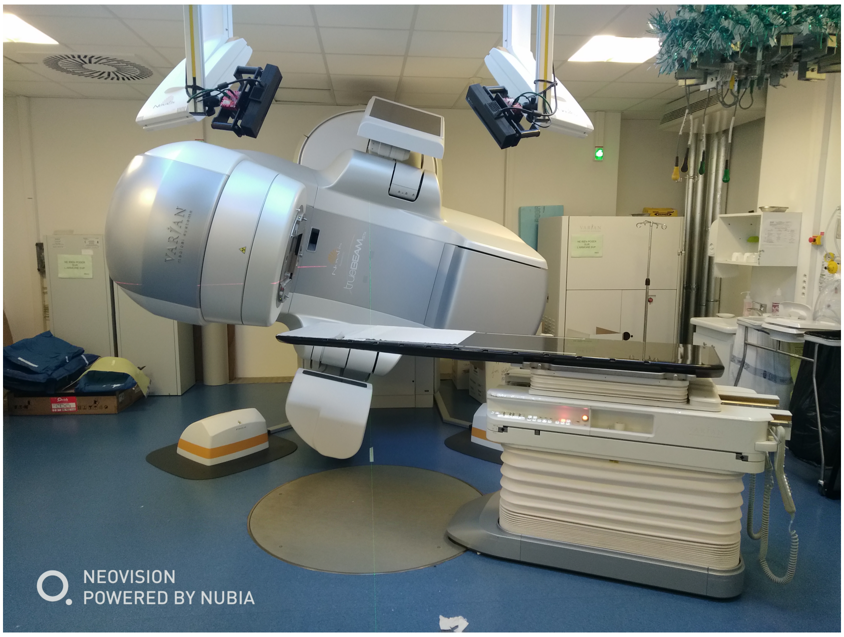

(a)

Figure 2.5 – Example of collision test done on Real equipment a Varian Trubeam®LINAC installed at CHRU Brest $\phi = -76°, \theta = 65°$

Figure 2.6a shows a plot of the couch-gantry orientations where collisions have been detected (in black) and couch-gantry orientations that are collision-free (in blue) at a fixed patient couch position of $(P_x = 0mm, P_y = 0mm, P_z = 0mm)$. We observe that the largest collision-free workspace is a pure subset of the full couch-gantry workspace. This implies that a continuous trajectory can be found to move from a particular couch-gantry angle orientation to another without crossing a collision-prone area of the workspace. This is a very important for non-coplanar VMAT treatment planning as the gantry and couch rotate continuosly during treatment., it is important that the trajectory does not traverse a collision-prone configuration.

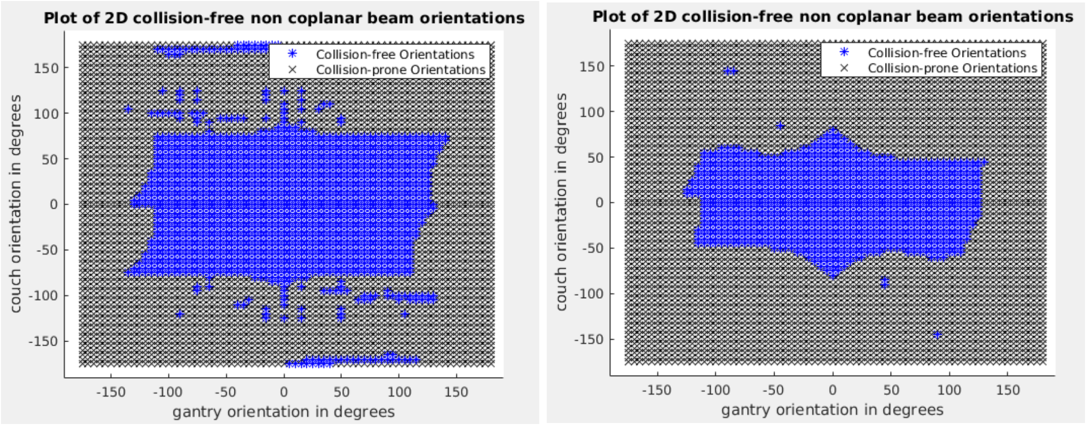

(a) (b)

Figure 2.6 – Plot of collision-free workspace at couch setting (a) $(P_x = 0mm, P_y = 0mm, P_z = 0mm)$ (b) $(P_x = 0mm, P_y = 0mm, P_z = -200mm)$

To see the effect of different patient couch positions on the collision-free workspace we change the couch position to $(P_x = 0mm, P_y = 0mm, P_z = -200mm)$. This change corresponds to a motion of the patient couch vertically upwards by 200mm. Figure 2.7a plots the results of the collision detection simulation with collision-prone workspace in black and collision-free workspace in blue. We observe a reduction in the size of the collision-free workspace when the position of the patient couch is increased vertically. This is because an increased height of the patient couch moves it closer to the rotating gantry thereby increasing the likelihood that a collision occurs.

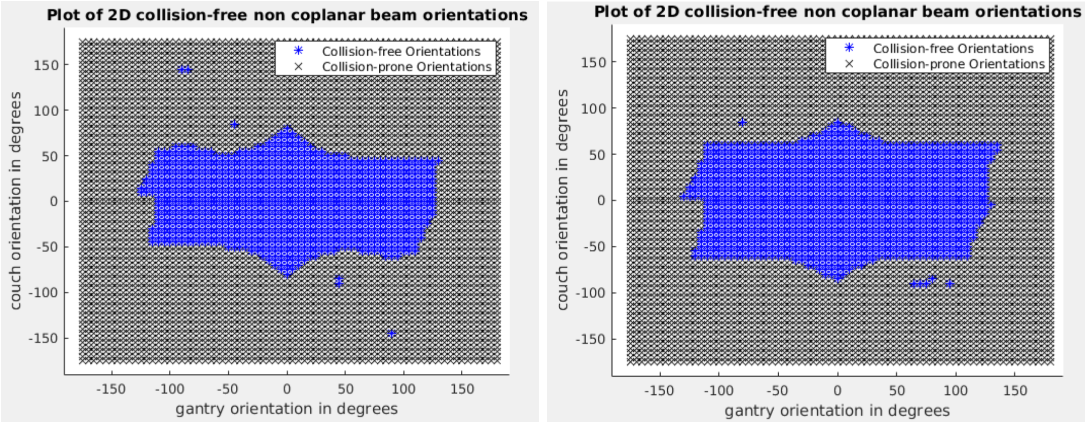

(a) (b)

Figure 2.7 – Plot of collision-free workspace at couch setting (a) $(P_x = 0mm, P_y = 0mm, P_z = -200mm)$ (b) $(P_x = 100mm, P_y = 0mm, P_z = -200mm)$

The next test is to see the effect of a change in the longitudinal couch position on the collision-free workspace. The couch position is set to $(P_x = 100mm, P_y = 0mm, P_z = -200mm)$ corresponding to a longitudinal motion of the couch towards the gantry. From the plot of the collision detection results in figure 2.7b we see that the increase of the longitudinal position of the couch allows for a slight increase in the workspace compared to the couch setting where the longitudinal position was unchanged in figure 2.7a.

2.5 Discussion

Non-coplanar treatment planning requires the simultaneous rotation of the couch and gantry which raises the posibilty of collision between parts of the treatment equipment. Each couch and gantry angle combination has to be checked for the existence a collision and the collision-prone pairs have to be omitted for planning purposes. We have presented a methodology that can be used to check and detect collisions at a pre-planning stage to generate collision-free candidate couch-gantry orientations.

The proposed methodology can facilitate the process of collision checking for each fixed table position in an automated fashion which is an improvment over previous methods [116] that required a manual entry of each orientation to be checked. The methodology can be easily integrated in the planning workflow as a pre-planning step and the resulting couch-gantry angles can be utilized during the planning and post planning steps. The software tools employed (MATLAB and ADAMS) are easily obtainable and very commonly used in research, therefore the proposed method is repeatable at other treatment centers.

The required input for repeating this experiment is a 3D CAD model of the radiotherapy equipment installed at the treatment center and the desired translation positions of the couch. The use of a 3D CAD model of the LINAC equipment eliminates the need to peform cumbersome measurement on the equipment [111] and avoid introducing further errors in the simulation. The use of a 3D CAD model also reduces the computational cost that would have been incurred if image processing methods [114] were used to detect the collisions. The translation positions of the couch depends on the positioning of the patient which is decided by the treatment planner. Some collision-prone couch-gantry pair become collision-free when the translation positions of patient couch is adjusted [110]. But for a continuous non-coplanar delivery, the patient couch has to be fixed. Trying to avoid of a collision-prone configuration by changing the position of the patient couch during a rotation of the gantry/couch could lead to a discontinuous workspace and possibly an unattainable trajectory.

Using our proposed methodology, the results on the collision-free couch-gantry angle pair can be obtained in a matter of minutes. We found that the computation time is dependent of the number couch-gantry angle pairs being evaluated and thus depends on the discretization used. Typical discretzation values in non-coplanar treatment are in the range between $2^\circ and 6^\circ$. With the discretization in this range, the computation time for this methodology is not significant.

The accuracy of these results can be affected by factors linked to the discrepancies between the real equipment and the simulated 3D CAD model. Such differences include differences in the isocentre position and differences in the couch translation positions during simulation. Another factor that could affect the accuracy could be in the positioning peripheral components such as the EPID imaging equipment usually attached to the rotating gantry. For LINACs equipped with this component, it is important that the operating mode during patient treatment co-incides with the position in simulation. However these factors do not lead to great discrepancies under normal operating conditions and a safety margin can be adopted to minimize their effects.

A limitation to this method is that it does not take into account collisions between the gantry and a patient model. This limitation can easily be overcome by introducting a bounding box that represents the patient on the couch. Future work is to introduce a patient model obtained from recontruction of patient image captured as a 3D point cloud for the collision detection studies.

CHAPTER

3

OPTIMIZING BEAM SELECTION FOR NON-COPLANAR VMAT TREATMENT PLANNING WITH SIMULATED ANNEALING

We propose an approach to beam selection for non-coplanar VMAT that combines a simulated annealing inspired algorithm with direct leaf trajectory optimization. Beam angle selection is performed using simulated annealing to obtain globally optimal beams. Direct leaf trajectory optimization is used for dosimetric evaluation during beam selection instead of fluence map optimization in order to account for machine constraints. Treatment plans for the AAPM TG-119 evaluation case, a clinical case in prostate cancer and for a clinical case in liver cancer are computed using our proposed algorithm and compared to the state of the art approach on the basis of prescription mean and maximum dose to the PTV, organs-at-risk and delivery time. The results show an accurate delivery of the prescription dose to the target tumor volume ($50Gy \pm 0.8$) in all cases. The results also show an improved organ at risk sparing in terms of a reduced mean dose to the core in TG-119 case (38%), the rectum, the heart in liver case (38%) and the penile bulb in prostate case (14% and 26% respectively). The estimated delivery time when using our proposed algorithm was higher in all cases ($\sim 30\%$) compared to the state of the art. An increase in the number of control points has been observed when using our method compared to the state of the art method but conversely there is a reduction in the average delivery time spent at each control point. The use of the proposed simulated annealing inspired algorithm to generate non-coplanar trajectories for VMAT presents an opportunity to search a larger space in order to obtain globally optimal beam orientations leading to an improvement in organ-at-risk sparing.

3.1 Introduction

The main goal in VMAT is to deliver rapidly the maximum prescribed dose to the tumor, minimizing the dose to the surrounding organ-at-risk. Given these objectives, both improved dose planning and delivery monitoring approaches are becoming increasingly essential [118, 119, 120].

In non-coplanar VMAT, the gantry carrying the radiation beam and the patient couch rotate simultaneously to change the radiation beam orientation. At the same time, the radiation fluence intensity is changed at each control point to obtain a prescribed dose distribution within the tumor in the patient. Several authors [84, 77, 83] have argued that non-coplanar VMAT could lead to superior treatment plans and should be used more extensively in treatment planning. A major advantage is that non-coplanar VMAT can achieve better organ-at-risk avoidance by orienting the radiation beams in a different geometric plane relative to the patient.

One of the earliest approaches for non-coplanar VMAT planning is to make use of a combination of a fixed patient couch and a rotating gantry during treatment [87, 88, 89, 90]. One weakness of this approach is that the definition of the treatment trajectory is manually done and thus varies from one treatment planner to the other. Such a method for selecting non-coplanar trajectory is not repeatable for a different tumor geometry or when a different planner creates the trajectory. Also, the entire space of possible couch-gantry orientation combination is not explored to select the most optimal trajectory with respect to the treatment objectives.

Another approach for non-coplanar VMAT makes use of a combination of a fixed gantry and a rotating couch during treatment [91, 121]. This approach was used for accelerated partial breast irradiation (APBI) to successfully reduce the dose received by normal breast tissues during treatment. But using such a technique comes with an increased risk of collision and an increased planning complexity. The use of a rotating couch fixed gantry combination produces a discontinuous and non-isocentric beam trajectory which is unsuitable for tumor most locations in the body. The search space for the optimal control points for irradiation is also severely limited.

Most recent non-coplanar VMAT studies employ a combination of a dynamic couch-gantry motion during treatment [92, 85, 86, 77, 93, 94, 95, 96]. In this way, there is increased degree of freedom and consequently a greater flexibility to obtain optimal control points for patient irradiation.

A challenging aspect of non-coplanar VMAT planning is the creation of the treatment trajectory for patient irradiation. The treatment trajectory is a sequence of orientations along which the couch and gantry move during treatment. Early approaches [88, 89] to the determination of non-coplanar trajectories for VMAT were performed manually with unoptimized beams.

Subsequent improvements saw the introduction of geometric methods that use the beam's eye view (BEV) information [85, 86, 94, 96, 95]. The geometric methods assign a score to each beam orientation in relation to the tumor's shape and a search algorithm is used to determine a non-coplanar trajectory through the lowest scoring beams.

The geometric methods differ in the search algorithm they employ such as hierarchical clustering [85], Djikstra's algorithm [86, 94] or A^* [96, 95]. The advantage of these geometric methods is that they offer a fast way to choose beam angles that form part of the non-coplanar VMAT treatment trajetory. The drawback of such geometric methods is that they do not evaluate the fluence contribution of a combination of beams angles during selection. So a single beam angle that may appear to offer a good target coverage and organ-at-risk avoidance may become suboptimal in a combination with other beam angles.

An alternative to geometric methods are fluence methods [103, 77, 93, 94] which formulate the trajectory generation problem as a beam angle optimization problem. Fluence methods solve a fluence map optimization [122] (FMO) problem when selecting beam angles for the non-coplanar VMAT trajectory. Some of the fluence methods use a two-step approach [77, 93]. First a beam angle optimization is solved to obtain a set of beams. These beams are then linked to form a trajectory by solving a traveling-salesman problem and the final VMAT plan is created using this trajectory . These fluence methods that involve two-steps differ principally in their beam angle selection strategy such as: genetic algorithm[77], greedy strategy [93], look-ahead strategy [93], gradient-norm strategy [93].

Other fluence methods [103, 94] perform VMAT optimization and trajectory generation concurrently. One approach [94] uses an $l_{2,1}$ anisotropic sparse minimization for VMAT optimization while alternately using a graph search to find a non-coplanar trajectory. Another approach [103] creates the beam trajectory by performing monte-carlo search on a tree structure. Different possible trajectories in the tree-structure are evaluated by solving an FMO problem. The solution obtained from the fluence optimization is used in subsequently to search for new nodes to be included on the tree.

Most of the highlighted fluence methods [103, 77, 93, 94] solve an FMO problem in order to evaluate the dosimetric quality of a beam combination during trajectory creation. The problem with the use of FMO for evaluating the dosimetric quality of a trajectory is that the machine and multi-leaf collimator (MLC) constraints are not considered during the trajectory evaluation process. The highlighted methods use the direct aperture optimization technique [72] (DAO), which is a non-convex optimization problem, for generating the VMAT final plan. The non-convexity of the DAO problem and the extremely large number of possible apertures makes it difficult to use DAO for dosimetric evaluation of the beams during trajectory formation.

Another approach called the direct leaf trajectory optimization [80] has been proposed for VMAT planning. The direct leaf method optimizes directly the MLC trajectory for radiation delivery in a sliding window fashion while taking into account MLC and machine constraints. This method has the advantage of avoiding the arc-sequencing step used in DAO so that plan quality is not compromised. This formulation thereby lends itself to be used for dosimetric evaluation during in the simultaneous beam selection and VMAT generation process.

A recent state of the art non-coplanar VMAT method [93] uses direct leaf trajectory optimization for creating the final VMAT plan. The fluence methodology proposed in this work is the state of the art and the general approach is seen in other fluence methods [103, 77, 94] with variations in the beam angle selection strategy. However, this state of the art method uses FMO for dosimetric evaluation during beams selection phase. Due to the large number of possible beams under consideration, fluence evaluation is done on a limited of the beam solution space during trajectory creation.

In this work, our hypothesis is that in order to obtain a high quality non-coplanar VMAT treatment plan we have to explore the entire space of candidates beams during trajectory generation to select the dosimetrically optimal beams. There is also a need to consider the MLC and machine constraints during the trajectory creation phase. This ensures the final trajectory is deliverable. It also ensures that the plan dosimetry evaluated during trajectory creation corresponds as much as possible to the final VMAT plan dosimetry.

Within this context, we propose and investigate a non-coplanar VMAT planning method that selects globally optimal beam orientations during trajectory creation while considering the MLC and machine constraints. We compare the resulting treatment plan obtained using our method to a state of the art approach [93]. The contribution of this paper is a simulated-annealing inspired algorithm for beam selection in non-coplanar VMAT treatment planning. The proposed algorithm is capable of producing the global optimum to the combinatorial optimization problem by evaluating the fluence contribution in the space of candidate beam angles in an unrestricted manner. Our method follows the general non-coplanar VMAT planning method proposed in [93] with the main difference in the beam angle selection method.

The chapter is organized as follows: Section 3.2.2 presents the simulated annealing non-coplanar VMAT planning algorithm, the method used to choose the algorithm parameters and the conditions for convergence. Details on the beam trajectory generation are presented in section 3.2.3 while section 3.2.4 shows the implementation details. The metrics used for comparison in the evaluation study on three patient cases can be found in section 3.2.5. The results of the evaluation study are presented in section 3.3 and then discussed in section 3.4.

3.2 VMAT treatment plan optimization

Given the 3D computed tomography (CT) image of a cancer patient, the entire volume contains a set of $\mathbb{V}$ discrete voxels. The incident radiation beam b for patient treatment at each orientation can be decomposed into a set of beamlets. The dose received by a voxel $j \in \mathbb{V}$ is denoted as d_j and the intensity of an incident beamlet $i \in b$ with fluence intensity x_i. $\mathbb{B}$ denotes the set of candidate beam angles that are available for the VMAT treatment planning. Such that $b \in \mathbb{B}$ a set of equally spaced couch-gantry angle pairs that constitute a 4π space. At the initial stage, the infeasible or collision-prone configurations are removed from $\mathbb{B}$. The dose influence matrix, $\mathbf{D}$, expresses the relationship between the dose received by a voxel d_j and a beamlet of unit fluence intensity x_i, such that:

$$d_j = \sum_{i \in b} D_{ji} x_i \tag{3.1}$$

$$\mathbf{D} = \begin{bmatrix} D_{1,1} & D_{1,2} & \dots & D_{1,i} \\ \vdots & \vdots & \ddots & \vdots \\ D_{j,1} & D_{j,2} & \dots & D_{j,i} \end{bmatrix}, \ \mathbf{x} = \begin{bmatrix} x_1 \\ \vdots \\ x_i \end{bmatrix}, \ \mathbf{d} = \begin{bmatrix} d_1 \\ \vdots \\ d_j \end{bmatrix} \tag{3.2}$$

Given a dose prescribed by the physician $\mathbf{d}^p$ to be delivered to the tumor, our objective function minimizes the least-square deviation between the prescribed dose and the actual dose received by the tumor voxels.

$$f(\mathbf{d}) = \frac{1}{N_t} \sum_{j \in \mathbb{V}_{\approx}} p^+ (d_j - d_j^p)^2 + \frac{1}{N_o} \sum_{j \in \mathbb{V}_{\rtimes}} p^- (d_j - d_j^p)^2 \tag{3.3}$$

where $\mathbb{V}_{\approx} \subset \mathbb{V}$ denotes the tumor voxels with cardinality $|\mathbb{V}_{\approx}| = N_t$ and $\mathbb{V}_{\rtimes} \subset \mathbb{V}$ denotes the organ-at-risk voxels with cardinality $|\mathbb{V}_{\rtimes}| = N_o$. p^+ is a penalty factor for controlling the relative importance of the target tumor voxels and p^- is the penalty factor for controlling the relative importance of organ-at-risk voxels. At an initial stage, the dose influence matrix $\mathbf{D}$ is calculated for each beam angle $b \in \mathbb{B}$ in the set of all candidate beam angles.

3.2.1 Non-coplanar VMAT planning methodology

Our planning follows the recent state of the art approach [93] with an aim to improve on the beam angle selection. Beam angle selection is performed to obtain optimal beams from the set of all candidate beam angles to serve as control points for the treatment trajectory. A traveling salesman problem is solved to connect all the optimal beam angles obtained from beam selection to form a valid treatment trajectory. Finally a direct leaf trajectory optimization is performed to obtain the final plan using the new trajectory.

In order to improve the beam angle selection step, our approach makes use use of direct leaf trajectory optimization to evaluate the fluence contribution during the beam angle selection instead of fluence map optimization. The direct leaf trajectory optimization is used during the beam angle selection phase to improve comparison between treatment plans and to better account for MLC and machine constraints. Another difference in our approach is that there is no-limitation on the space of the candidate beam angles to be explored during the search for optimal beams. Therefore a very large space of candidate beam orientations is available for selecting the optimal beam orientations.

3.2.2 Beam selection algorithm using simulated annealing

Simulated annealing [123] is a widely used heuristic method that is used to find a global solution to a combinatorial optimization problem. It mimicks the annealing process in metallurgy with the notion of slow cooling interpreted as a slow decrease in the probability of accepting sub-optimal solutions as the algorithm proceeds. Simulated annealing has been applied to beam selection for intensity-modulated radiotherapy (IMRT) planning [124] and selecting optimal seed locations during inverse brachytherapy treatment planning [125].

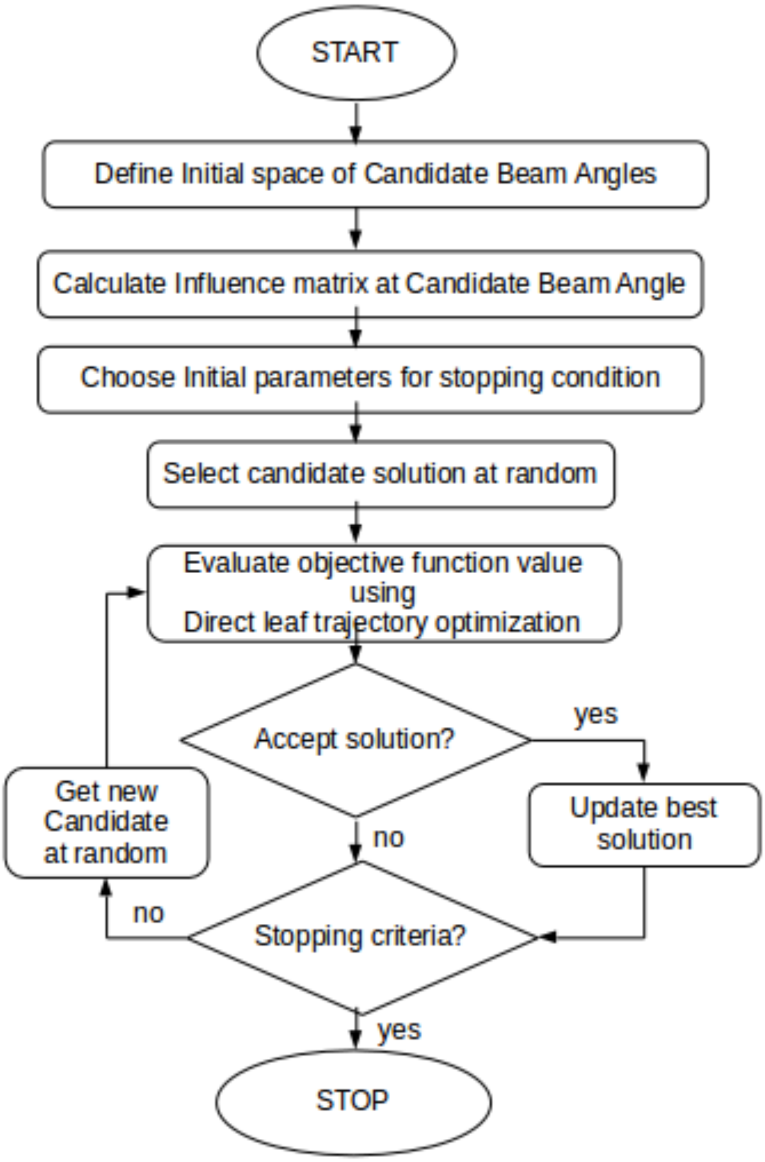

Figure 3.1 – Flowchart showing the Beam selection process using simulated annealing

The simulated annealing non-coplanar VMAT algorithm 4 is proposed in order to search the space of all input candidate beams to obtain globally optimal beam orientations. This method combines the work of [124] which applies a similar method for selecting beams for an IMRT optimization and direct leaf trajectory optimization[80]. The use of direct leaf trajectory optimization allows us to include the machine parameter constraints during the beam selection phase. This formulation for the VMAT optimization is a convex approximation and therefore lends itself for the evaluation of the objective function value in the simulated annealing algorithm. This formulation also has the advantage of avoiding the two-step process in DAO by eliminating the need to sequence fluence intensities into deliverable leaf apertures. The procedure for our proposed algorithm is illustrated in figure 3.1.

Algorithm 4 Non-coplanar VMAT by simulated annealing

```
$Init : \mathbb{K}^* \leftarrow \emptyset,\ \mathbb{B} \leftarrow \{b_1, b_2, ..., b_n\},\ i \leftarrow 0,\ \lambda \leftarrow 0.99,\ f \leftarrow directLeafOptim\,(\mathbb{K})$
$choose\ T_{init}\ using\ \ equation\ 3.4\ \ and\ T_{final}\ using\ \ equation\ 3.5$
$T_i \leftarrow T_{init}$
while ($T_i > T_{final}$) do
    $\mathbb{K}_i \leftarrow \mathbb{K}^*$
    $b^* \leftarrow randomSample\,(\mathbb{B} \setminus \mathbb{K}_i)$
    $\mathbb{K}_i \leftarrow \mathbb{K}_i \cup b^*$
    $f_i \leftarrow directLeafOptim\,(\mathbb{K}_i)$
    $p_i \leftarrow exp\left(\frac{f - f_i}{T_i}\right)$
    if ($rand\,(0, 1) \leq p_i$ ) then
        $\mathbb{K}^* \leftarrow \mathbb{K}_i$
        $f \leftarrow f_i$
    else
        $\mathbb{K}_i \leftarrow \mathbb{K}_i \setminus b^*$
    end if
    $T_i \leftarrow \lambda.T_{i-1}$
    $i \leftarrow i + 1$
end while
return $\mathbb{K}^*$ ; $f$
```

Algorithm 4 starts initially with a set of non-coplanar candidate beams ($\mathbb{B}$) and an initial temperature (T_{init}). The output is a set containing the optimal beam combination ($\mathbb{K}^*$). Our implementation of the direct leaf trajectory optimization is referred to as *directLeafOptim()* [80].

At each iteration, a beam (b^*) in the set of non-coplanar candidate beams ($\mathbb{B}$) is selected at random to be replaced by a candidate beam not included in the treatment plan using the function *randomSample()*. The objective function value (f) of this beam angle combination is calculated by solving the direct leaf trajectory optimization using the function *directLeafOptim()*. In this way, we take into account the machine constraints and MLC leaf constraints when comparing different beam angle combinations. The selected beam combination is accepted as the best if the acceptance probability p_i is greater than a threshold chosen by the user. The cooling temperature is progressively decreased by a factor (λ) to control the probability of accepting a new solution. The algorithm is stopped when the cooling temperature T_i is less than a chosen threshold for the final temperature T_{final}.

Choosing the Initial and Final Temperature for simulated annealing

The choice of the initial and final temperatures (T_{init} ,T_{final}) influences the cooling rate of Algorithm 4 and hence the speed of convergence [126]. If T_{init} is set too high, a lot of time is spent at the beginning of the algorithm and if set too low, the algorithm terminates with a local solution in a very short time. T_{init} is chosen using an analytical relationship that maximizes the probability of accepting state transitions during the initial search in the solution space [127]. Specifically:

$$T_{init} = \frac{-\Delta f_{max}}{ln\left(P - \Delta f_{max}\right)} \tag{3.4}$$

where $\Delta f_{max} = max\left(f(\mathbb{K}_i) - f(\mathbb{K}_j)\right)$ defines the maximum deterioration in the objective function value from solution $\mathbb{K}_i$ to a neighboring solution $\mathbb{K}_j$. $P()$ is the acceptance probability function. Typical values for $P\left(-\Delta f_{max}\right)$ are around 0.99, 0.9, 0.8. In the same way, a T_{final} set too high delays the algorithm termination and if set too low, the algorithm terminates with a local solution. Our choice of T_{final} minimizes the probability of accepting a state transition as the number of iterations $i \longrightarrow \infty$ so that:

$$T_{final} = \frac{-\Delta f_{min}}{ln(P(-\Delta f_{min}))} \tag{3.5}$$

where $\Delta f_{min} = min\left(f_i - f_j\right)$ defines the minimum deterioration in the objective function value from solution $\mathbb{K}_i$ to a neighboring solution $\mathbb{K}_j$. Typical values for the acceptance probability $P\left(-\Delta f_{min}\right)$ are around 0.1, 0.2, 0.3.

Convergence of the simulated annealing Algorithm

The convergence Algorithm 4 to the global minimum corresponds to the beam angle combination that gives the lowest objective function value from the direct leaf trajectory optimization among all candidate solutions. This corresponds to probability condition that $\lim_{i\to\infty} P\left[\mathbb{K}_i \in \mathbb{K}^*\right] = 1$ [126].

Simulated annealing can be viewed as a sequence of homogeneous Markov chains with constant temperature T_i in each chain and the temperature decreased from one chain to the next chain [128]. If the state transition matrix associated to the Markov chain at a particular temperature T_i is irreducible and aperiodic, then simulated annealing algorithm converges if and only if $\lim_{i\to\infty} T_i = 0$ [129]. Irreducibility implies that there exists a non-zero probability to find a solution from one beam angle combination $f\left(\mathbb{K}_i\right)$ to another $f\left(\mathbb{K}_j\right)$ [128].

Due to the approximate convexity of the direct leaf trajectory optimization formulation [80], a unique solution to the objective function value f can always be found and thus our formulation is irreducible. Similarly, aperiodicity means that starting from beam angle combination solution $f\left(\mathbb{K}_j\right)$ it is possible to return to $f\left(\mathbb{K}_i\right)$ in one period. This property is enforced in the function *randomSample()* so that at each period, each beam angle $b^* \in \mathbb{B} \setminus \mathbb{K}_i$ has an equal probability to be chosen.

3.2.3 Trajectory generation

After the selection of the optimal beams, a trajectory is generated to connect them together. A graph $G\left(N,E\right)$ can be used to represent the candidate beam angle space $\mathbb{B}$. Each node of this graph corresponds to a couch-gantry angle combination or control point i.e. $N = \{(c_1, g_1), (c_2, g_2), \ldots (c_n, g_n)\} = \{n_1, n_2, \ldots n_n\}$. There exists an edge between two nodes n_1 and n_2 if and only if the euclidean distance between them is less than a threshold ϵ.

$$\| n_1 - n_2 \| = \sqrt{(c_1 - c_2)^2 + (g_1 - g_2)^2} \le \epsilon \tag{3.6}$$

The threshold ϵ enforces the maximum motion constraint from one couch or gantry angle to the other. The value of ϵ depends on the spacing used in creating couch-gantry angle pairs. If the maximum allowed motion from one couch or gantry angle to the other is θ° then:

$$\epsilon = \sqrt{\theta^2 + \theta^2} \tag{3.7}$$

An adjacency matrix $\mathbf{A}$ is created to represent the edges of graph $G(N,E)$ such that:

$$\mathbf{A}(n_i, n_j) = \begin{cases} \| n_i - n_j \|, & \text{if } \| n_i - n_j \| \le \epsilon \; \forall i, j \in \mathbb{B} \\ \infty, & otherwise \end{cases} \tag{3.8}$$

A traveling salesman problem is solved on graph G to obtain a path to connect the optimal beam angles $\mathbb{K}^*$ already chosen by the simulated annealing algorithm. We have adapted a genetic algorithm implementation [130] for use in solving the traveling salesman problem. The objective is to minimize the total euclidean distance traveled along the path to visit all the input nodes. To solve the traveling salesman we create another adjacency matrix $\mathbf{A}_{\mathbb{K}^*}$ that defines edges of the selected optimal beam angles. Such that:

$$\mathbf{A}_{\mathbb{K}^*}(n_i, n_j) = \begin{cases} \| n_i - n_j \| \; \forall i, j \in \mathbb{K}^* \end{cases} \tag{3.9}$$

$\mathbf{A}_{\mathbb{K}^*}$ serves as an input to the genetic algorithm to solve the traveling salesman problem. The result is an optimal path $\mathbf{p}_1$ that connects all the selected optimal beam angles. But the optimal path $\mathbf{p}_1$ might not be feasible as some consecutive beam angles may be too far from each other. Therefore intermediate beam angles have to be included in-between using the algorithm 5 below:

Algorithm 5 Heuristic Algorithm for creating final trajectory

```
Init : $G$, $\mathbf{p}_1$, $\epsilon$, $\mathbf{A}_{\mathbb{K}^*}$, $N \leftarrow |\mathbf{p}_1|$, $\mathbf{p}_2 \leftarrow \emptyset$
for $i = 1$ to $N - 1$ do
    if ($\mathbf{A}_{\mathbb{K}^*}\left(\mathbf{p}_1^i, \mathbf{p}_1^j\right) > \epsilon$ ) then
        $\mathbf{s} \leftarrow shortestpath\left(G, \mathbf{p}_1^i, \mathbf{p}_1^j\right)$
        $\mathbf{p}_2 \leftarrow \mathbf{p}_2 \cup \mathbf{s} \setminus \mathbf{p}_1^i$
    else
        $\mathbf{p}_2 \leftarrow \mathbf{p}_2 \cup \mathbf{p}_1^i$
    end if
end for
return $\mathbf{p}_2$
```

Algorithm 5 loops through consecutive nodes or beam angles in the optimal path $\mathbf{p}_1$ (denoted as $\mathbf{p}_1^i, \mathbf{p}_1^j$)to check if they are too far apart using line 3. If both nodes are too far apart, a shortest part between both nodes is calculated on the graph G using the function *shortestpath()* to return a series of nodes to be traversed to connect both optimal nodes. The output of Algorithm 5 is a new feasible path $\mathbf{p}_2$ containing the optimal path $\mathbf{p}_1$ with intermediate nodes inserted heuristically. A final VMAT optimization is performed using our implementation of direct leaf trajectory optimization and the beam angles in the final path $\mathbf{p}_2$. A new dose influence matrix including only the optimal beam orientations is calculated $\mathbf{D}_{\mathbb{K}^*}$ for use in the final VMAT optimization.

3.2.4 Hardware and software Implementation Details

Our computations were performed on a computer with Intel® Xeon® 16-core W-2145 3.7GHz processor and 256GB random access memory (RAM). The VMAT treatment planning experiments were performed using matRad [131] a toolkit for radiotherapy computational research and the research code was written in Matlab (version 2017a). The VMAT optimization is solved using an ipopt [132] implementation of L-BFGS algorithm [133] that is included in matRad.

We assume that the couch and gantry move at the same speed which is constant during the treatment. The beamlet size is set to $7 \times 7\ mm^2$ and MLC size of $40 \times 40\ cm$ is used. This beamlet size was chosen so as to reduce the size of the dose influence matrix due to main memory limitations of the computer. The MLC size chosen is the standard size available from most equipment manufacturers to enable comparison. Table 3.1 summarizes the machine parameters used for the direct leaf trajectory optimization.

Table 3.1 – Machine Parameters used for direct leaf trajectory optimization

Variable	Description	Value
δ	Dose rate	600 MU/min
l_{max}	Max leaf speed	3 cm/sec
g_s	Gantry speed	6 deg/sec
c_s	Couch speed	6 deg/sec

Data sets and parameters

Three data sets of cancer cases, an AAPM TG-119 benchmark case, a clinical prostate case cancer and a clinical liver case were considered for treatment plan evaluation using our proposed method. The AAPM TG-119 is a phantom provided by American Association of Physicists in Medicine Task Group 119 [134]. It is particularly adapted for studying and comparing non-coplanar treatment planning using a C-shaped target surrounding by an area of OAR. The patient CT data and the associated labeled segmentation for the prostate cancer case and liver case were obtained from the CORT dataset [135].

The candidate beam orientations, defined as couch-gantry angle pairs, are obtained from the CORT dataset [135]. The candidate beam orientations consist of 1983 non-coplanar beam angles sampled at 5° discretization. The dose influence matrix for each of the three evaluation cases is calculated using the pencil-beam algorithm implemented in matRad.

All cases have a target prescription dose of 50Gy and the maximum dose allowed to the OAR is set at 0Gy. The importance factor are chosen by trial-and-error as $p^+ = 1000$ for the tumor voxels and $p^- = 10$ for the organ-at-risk voxels except for the skin voxels which is set as $p^- = 400$ in order to select beams that are not too close to each other. Table 3.2 shows the details used for our treatment planning.

Table 3.2 – Patient cases used for the experiments

Description	**d$^{\mathbf{p}}$**	**Number of voxels**	**Number of beamlets**
TG-119 Case	50Gy	3597681	14545
Prostate Case	50Gy	3047040	63722
Liver Case	50Gy	7910952	28222

For comparison, treatment plans for the two evaluation cases were also prepared using our implementation of the non-coplanar VMAT method proposed in [93] which we refer to in subsequent section as greedy method. We consider this method as the state of the art in non-coplanar VMAT optimization.

Greedy Non-coplanar VMAT planning methodology for comparison

For comparison, treatment plans for the three patient cases was also prepared using our implementation of the non-coplanar VMAT method proposed in [93] which we refer to in subsequent section as greedy method. Using the same input candidate beam angles $\mathbb{B}$, beam angle selection is performed using a greedy strategy.

At each iteration, all available candidate beam angles are included in the optimal combination and the beam angle that leads to the lowest objective function value after fluence map optimization is selected. The greedy algorithm has no restriction on the number of iterations or the number of beams angles required. The greedy algorithm is stopped only when a 5% increase in the final objective function value is detected in comparison to the most recent final objective function value. To keep comparison similar, the same objective function in equation 3.3, importance factors and machine parameters are employed for both treatment planning methodologies under comparison.

Coplanar VMAT planning methodology for comparison

For comparison we have also prepared VMAT treatment plans for each of the three patient cases using a coplanar trajectory. The VMAT treatment plan optimization for the coplanar method is done using direct leaf trajectory optimization defined in section 3.2.1 with the same dataset and machine parameters as in section 3.2.4. The main difference is in the manner which the trajectory is created. For the coplanar plans, the trajectory contains the same couch orientation but different gantry orientations.

The coplanar beam trajectory consists of 37 beam angles and are obtained from the space of the candidate beam orientations described in sub-section 3.2.4. This is done to keep the comparison to the non-coplanar beam trajectory similar by maintaining the same angular distance as the coplanar trajectory. The gantry angles for the coplanar plan ranges between $(-90^\circ \leq 0^\circ \leq 90^\circ)$ and are selected from the space of candidate beam orientations where the couch angles is 0°.

3.2.5 Comparison Metrics

The treatment plans are compared using metrics such as Dose volume histogram, mean dose, maximum dose and conformity number.

Dose volume histogram (DVH)

The DVH is a cumulative histogram that shows the proportion of the volume of each region-of-interest and the quantity dose received. This plot presents a concise information of how much dose is absorbed by each volume in the patient and is useful for comparing treatment plans.

Mean dose

This measures the mean of the dose absorbed by all voxels in a specific region-of-interest of the patient. Given N voxels in a region-of-interest $\mathbb{V}$ with each voxel j receiving dose d_j, it is calculated using the relation:

$$Mean\ dose = \frac{\sum_{j=1}^{N} d_j}{N} \ j \in \mathbb{V} \tag{3.10}$$

Maximum dose

This measures the maximum dose absorbed received by a specific region-of-interest of the patient.

Conformity Number

The conformity number was proposed by [136] to quantitatively assess the degree of conformity of delivered dose. It is given as:

$$CN = \frac{V_{T,ref}}{V_T} \times \frac{V_{T,ref}}{V_{ref}} \tag{3.11}$$

where V_{ref} is the volume that receives a dose equal to or greater than the reference dose, $V_{T,ref}$ is the volume of target that receives a dose equal to or greater than the reference dose and V_T is the volume of the target. The conformity number ranges between 0 and 1. A value of 1 denotes that an exact prescription dose has been delivered to the target with no dose to the surrounding tissues while 0 denotes a lack of conformal dose.

Delivery Time

The delivery time is estimated using the total exposure time at each control point. The exposure time at a control point corresponds to the maximum traversal time for each row of the multileaf collimator at this control point which is calculated using the relationship in equation 1.28. The delivery time is an estimation because it is unknown at the time of planning the actual time taking by the machine to move between two control points as it strictly depends on the model of the machine being used for the treatment delivery and its motion dynamics.

3.3 Results

3.3.1 TG-119 Case

Figure 3.2 shows the DVH plot comparing a treatment plan developed using SA method (algorithm 4) in dashed line to a treatment plan developed using the greedy method in thick lines for TG-119 case. A similar conformal dose distribution to the Target is observed for both methods.

However a reduction in the dose to the Core and the Body can be observed in the DVH using SA method. This reduction is confirmed from the dose statistics in table 3.3 with mean dose to the Core using SA method (4.7Gy) vs (12.3Gy) for greedy method. This improvement represents a 72% reduction in the mean dose to the Core. A reduction in the mean dose to the Body using the SA method (3.7Gy) is also observed compared to the greedy method (4.8Gy) which is equivalent to a 27% reduction.

Compared to the coplanar method as shown in figure 3.3, the SA method also shows a better Target coverage with a mean dose of (49.6Gy) vs (49.5Gy). Both methods have the same mean dose to the Body. A 76% reduction in the mean dose to the Core is observed using the SA method compared to the coplanar method.

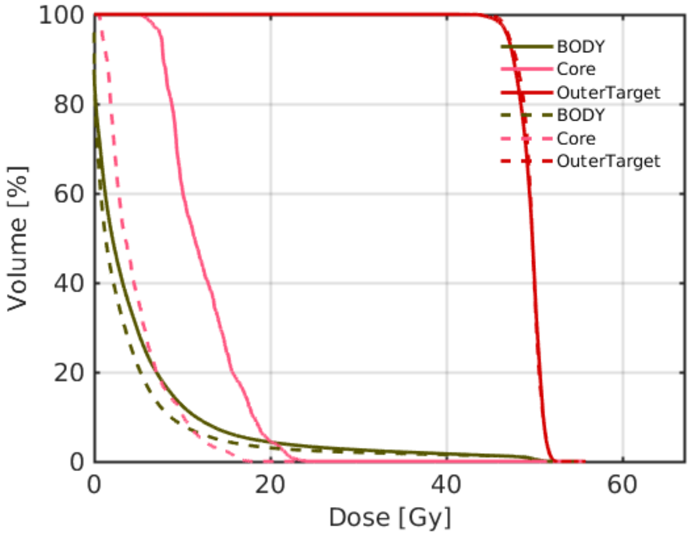

Figure 3.2 – DVH comparing the simulated annealing method (dashed lines) to greedy method (thick lines) for TG-119 case

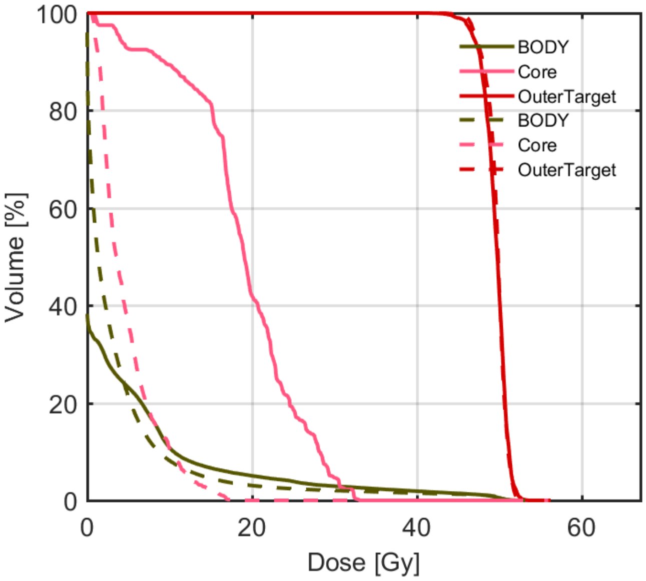

Figure 3.3 – DVH comparing the simulated annealing method (dashed lines) to Coplanar method (thick lines) for TG-119 case

Figures 3.4 shows the CT slices containing the dose contours for the TG-119 case planned using the three methods. A better conformal dose is observed from the dose contours when using the SA method. The improved dose conformity can be confirmed from table 3.3 with a conformity number of 0.92 for SA method compared to 0.91 for greedy method and 0.88 for the coplanar method. The SA method terminates with a lower final objective function value 16,400 vs 17,200 for greedy method and 25,500 for the coplanar method.

The trajectory comparison in figure 3.5 shows that the proposed SA method has a longer trajectory vs greedy method. The longer trajectory in the SA method is consequence of generating more control points (92) as more beams are added to the combination in search of a global solution. The greedy method has fewer control points (26) in its trajectory as the algorithm is stopped prematurely as soon as a local minimum is encountered. The coplanar trajectory is more straight forward as it is obtained from a fixed couch position defined by the treatment planner and not generated by an algorithm.

The effect of the trajectories on the treatment delivery can be further compared using the delivery time in table 3.4. We observe a delivery time of 227s for SA method vs a delivery time of 140s for greedy method and a delivery time of 183s for coplanar method. This implies that using the same couch and gantry speed, the trajectory for the SA method takes more time to deliver as it has more control points.

The shape of the final trajectory seen in figure 3.5 is created after the traveling sales man problem is solved to find a valid path that connects all control points. The control points are active during treatment and are indicated using a green circle. The intermediate trajectory points have no green circles around them and are not active during treatmeent. The intermediate trajectory points have been added in cases where two adjacent control points are not directly reachable. We note that the final delivery trajectory created for the SA method contains more intermediate control points have been added since it contains more control points.

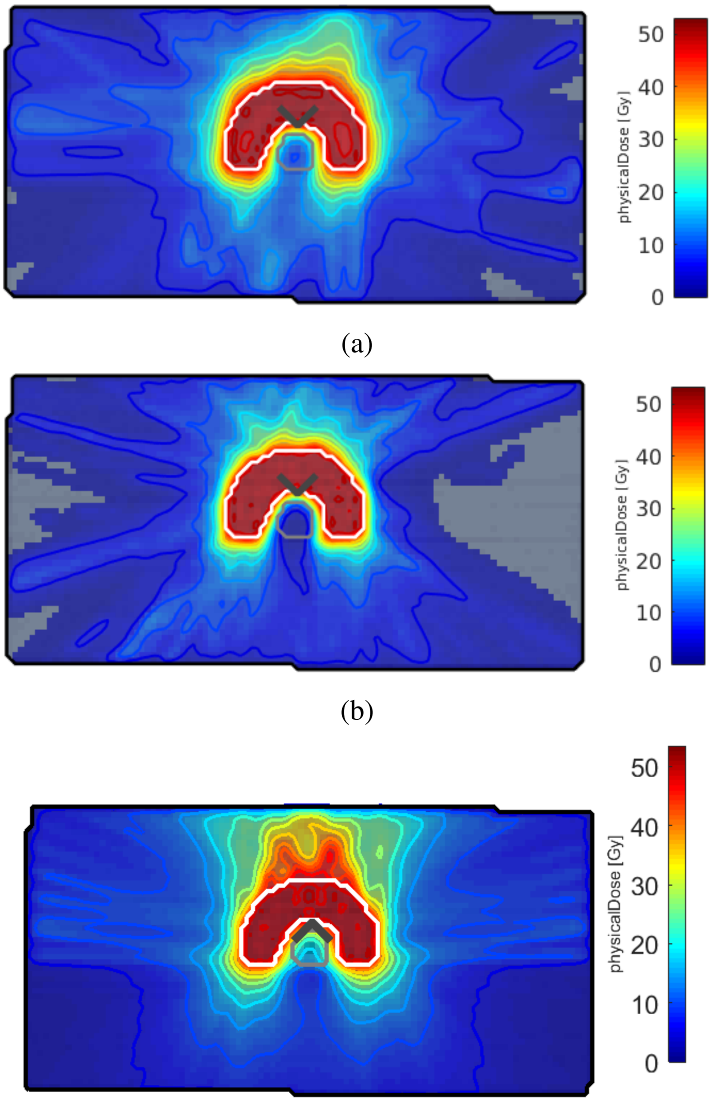

(a)

(b)

(c)

Figure 3.4 – Comparing Isodose contours for TG-119 using greedy method (a) SA method (b) and Coplanar method (c)

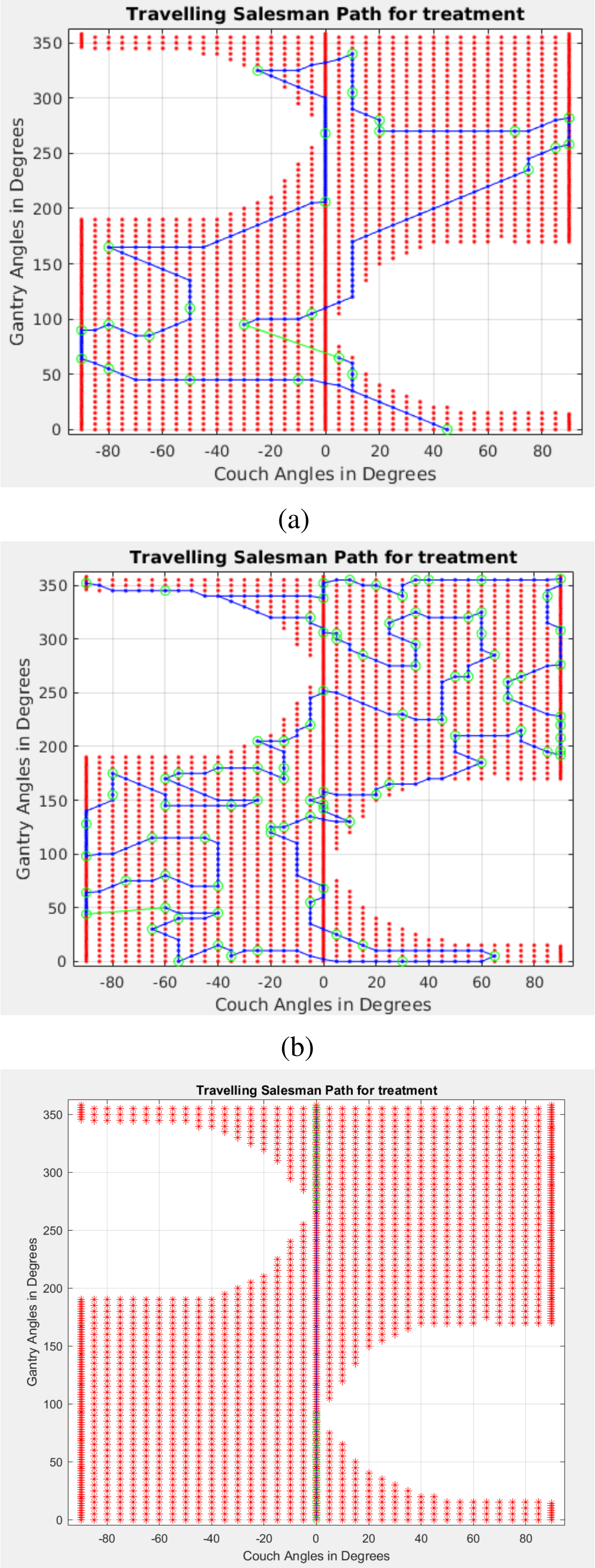

(a)

(b)

(c)

Figure 3.5 – Comparing Trajectories for TG-119 case using greedy method (a) and SA method (b) and Coplanar method (c)

Table 3.3 – Dose statistics for TG-119 case

Metric	**SA method**		**greedy method**		**Coplanar method**	
Objective function value	1.64×10^4		1.72×10^4		2.55×10^4	
Conformity Number	0.92		0.91		0.88	
Dose(Gy)	**Mean**	**Max**	**Mean**	**Max**	**Mean**	**Max**
Target	49.6	52.3	49.5	52.8	49.5	53.5
Core	4.7	17.6	12.3	24.2	18.9	32.9
Body	3.7	52.3	4.8	52.8	3.7	53.5

Table 3.4 – Comparing trajectory generated for TG-119 case

Metric	**SA method**	**greedy method**	**Coplanar method**
Estimated Delivery time	227s	140s	183s
No of control points	92	26	37

3.3.2 Liver Case

Figure 3.6 compares the DVH plot of the treatment plan using SA method (algorithm 4) in dashed line to a treatment plan developed using the greedy method in thick lines for Liver case. A similar conformal dose distribution to the target is observed for both methods.

The dose statistics in table 3.5 shows reductions to several organs-at-risk when using SA method vs greedy method. These reductions can be observed in the: SMASV 0.7Gy vs 1.6Gy (56%), Heart 2.6Gy vs 4.2Gy (38%), Celiac 1.1Gy vs 2.1Gy (48%), Duodenum 0.4Gy vs 1.0Gy (60%) and on the Skin 1.5Gy vs 1.7Gy (12%). Conversely an increase in the mean dose to the Spinal Cord is observed using the SA method 1.0Gy vs 0.2Gy for the greedy method.

Compared to the coplanar method, the SA method also shows a better Target coverage with a mean dose of (49.9Gy) vs (49.7Gy). This can also be observed in the DVH plot in figure 3.7. The coplanar method has 0Gy delivered to some organs at risk such as Celiac, Duodenum, SMASV. This is due to the trajectory chosen which is made up of a fixed couch position that completely avoids these organs. The same dose is recieved by the Skin (1.5Gy) and the Spinal Cord (1Gy) using both the SA method and the coplanar method. The main difference in both methods can be observed in the dose recieved by the heart which is 2.6Gy using the SA method and 7.5 Gy using the coplanar method. This represents a 66% reduction in the mean dose to the Heart.

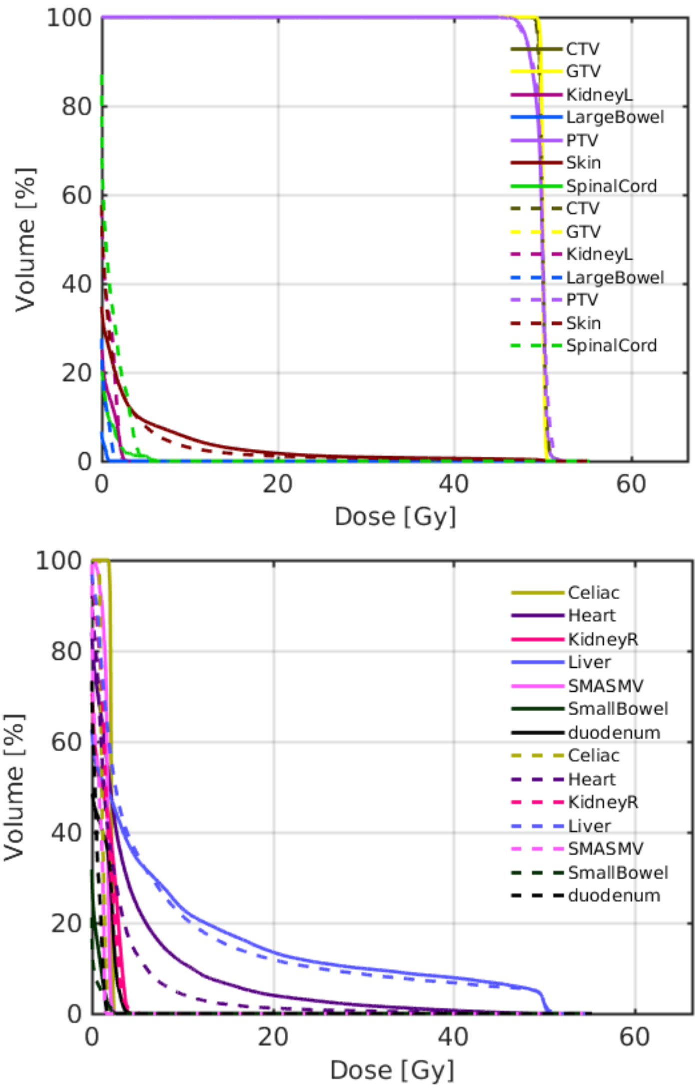

Figure 3.6 – DVH comparing the simulated annealing method (dashed lines) to greedy method (thick lines) for Liver case

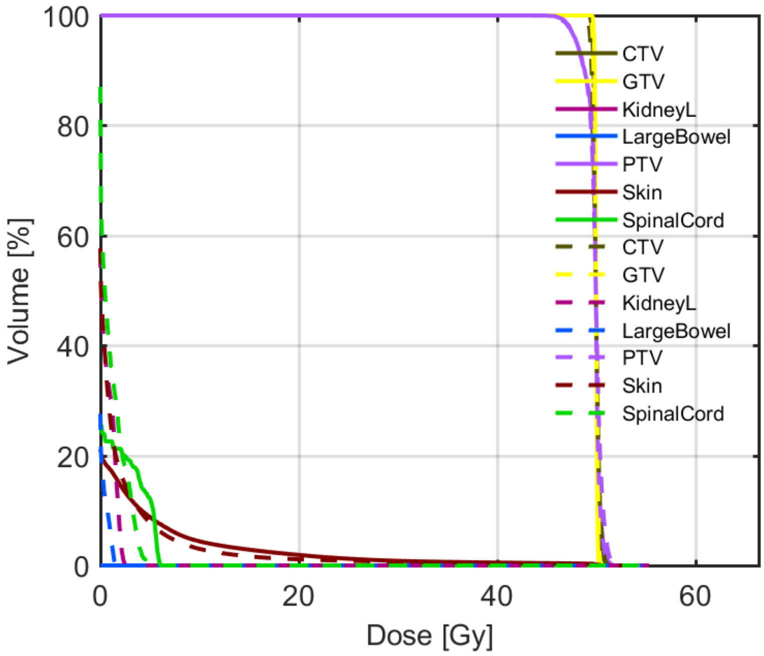

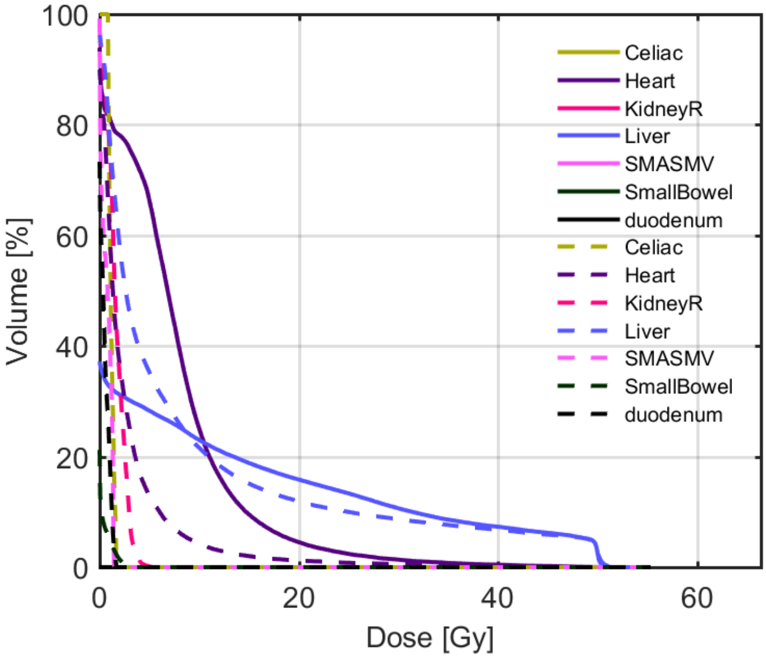

Figure 3.7 – DVH comparing the simulated annealing method (dashed lines) to coplanar method (thick lines) for Liver case

Table 3.5 – Dose statistics for Liver case

Metric	**SA method**		**greedy method**		**Coplanar method**	
Objective function value	9.5×10^3		1.05×10^4		9.63×10^3	
Conformity Number	0.95		0.9		0.93	
Dose(Gy)	**Mean**	**Max**	**Mean**	**Max**	**Mean**	**Max**
Target	49.9	51.4	49.7	51.9	49.7	51.8
Celiac	1.1	1.6	2.1	2.4	0	0
Heart	2.6	51	4.2	50	7.5	50.6
Spinal Cord	1.0	5.0	0.2	6.2	1	6
Duodenum	0.4	1.8	1.0	4.8	0	0
SMASV	0.7	1.4	1.6	2.4	0	0
Skin	1.5	52.6	1.7	51.9	1.5	51.8

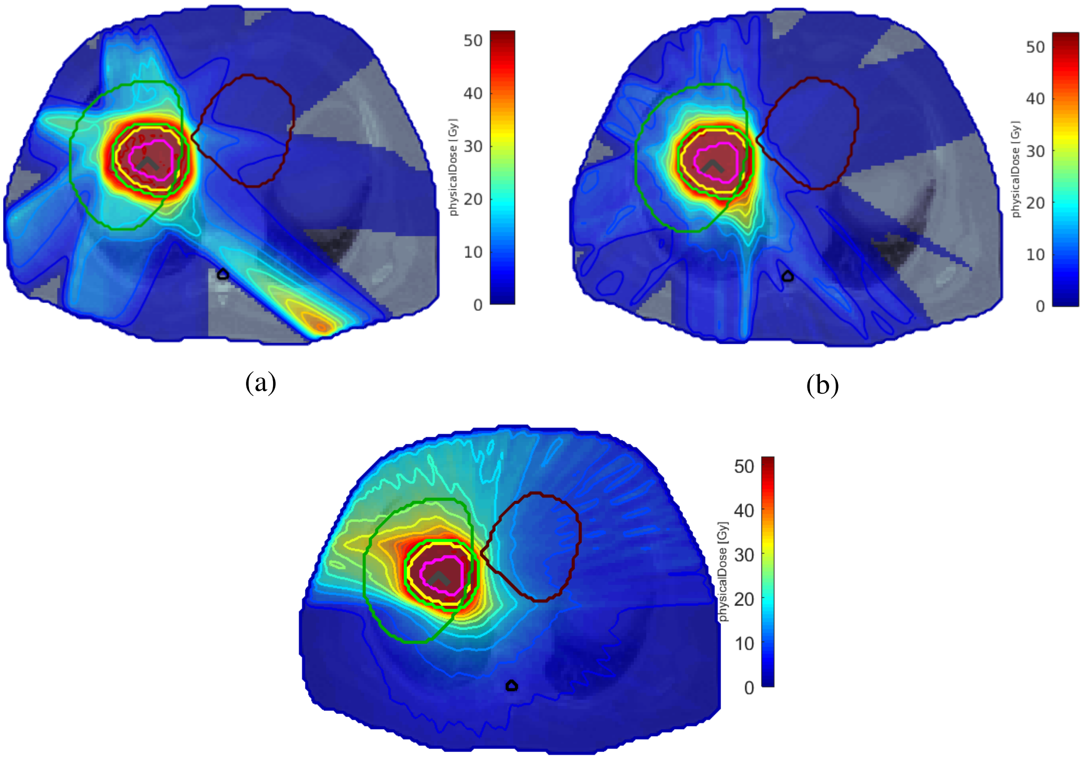

(a)

(b)

(c)

Figure 3.8 – Comparing Isodose contours for Liver using greedy method (a) SA method (b) and Coplanar method (c)

Figures 3.8 shows the CT slices containing the Isodose contours from the treatment plan for the Liver case using the three methods. A more conformal dose to the Liver using the SA method can be observed. We can observe a high dose area occuring in the bottom left of the CT slice for the greedy method figure 3.8a. This high dose area is an illustration of a local minimum being encountered. Since the greedy algorithm has no mechanism of removing

Metric	SA method	greedy method	Coplanar method
Estimated Delivery time	132s	127s	145s
No of control points	31	43	37

Table 3.6 – Comparing trajectory generated for Liver case

beams which become sub-optimal when other beams are added to the combination, the result is a sub-optimal solution. A higher conformity number (0.95) can be observed in table 3.5 for SA method compared to 0.91 for greedy method and 0.93 for coplanar method. The SA method terminates with a lower final objective function value 950 vs 1050 for greedy method and 963 for coplanar method.

The trajectory comparison in figure 3.9 shows that the proposed SA method has a longer trajectory vs greedy and the coplanar method. This can be confirmed in table 3.6 with 31 control points for the trajectory generated SA method vs 43 control points from the greedy method and 37 control points for the coplanar method. The longer trajectory occurs in SA method because the algorithm adds more control points to the beam combination in the search for a global optimum.

The delivery time is estimated to be 132s for the SA method leads vs 127s for the greedy method and 145s for the coplanar method The final trajectory is created after the traveling sales man problem is solved contains some intermediate control points like in the TG-119 case. The active trajectory points are circled in green while the non-active points are not circled and are not active during treatment delivery. The non-active trajectory points are inserted to ensure that the motion from one couch-gantry combination to the next is feasible.

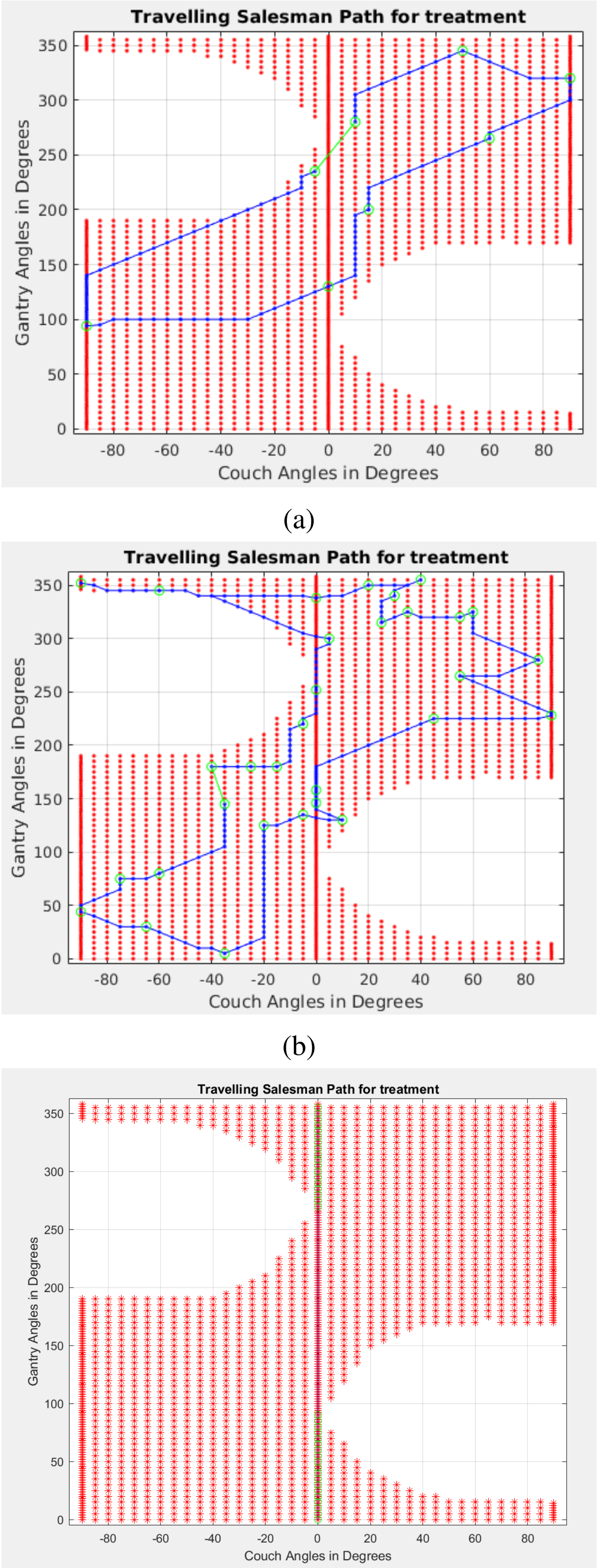

(a)

(b)

(c)

Figure 3.9 – Comparing Trajectories for Liver case using greedy method (a) SA method (b) Coplanar method (c)

3.3.3 Prostate Case

Figure 3.11 shows the DVH plot comparing a treatment plan developed using SA method (algorithm 4) in dashed line to greedy method in thick lines. A similar conformal dose distribution to the Target is observed for both methods (49.4Gy).

However a reduction in the dose to the bladder and the Rectum can be observed in the DVH using SA method. This reduction is confirmed from the dose statistics in table 3.7 with mean dose to the Rectum 19.5Gy vs 22.4Gy (14%), Bladder 22.5Gy vs 23.5Gy (4%), Penile Bulb 4.9Gy vs 6.2Gy (21%). The table also shows that the SA method has terminated with an objective function value that is 5% lower than greedy method.

Comparing to the coplanar method from the DVH in figure 3.14 the SA method shows a similar Target coverage with a mean dose of 49Gy vs 49.4Gy. The coplanar method has 8% less mean dose to the Skin 6.9Gy vs 6.4Gy and 82% less mean dose to the Penile Bulb 4.9Gy vs 0.4Gy. Conversely the SA method has has 15% less mean dose to the Bladder and 11% less mean dose to the Rectum.

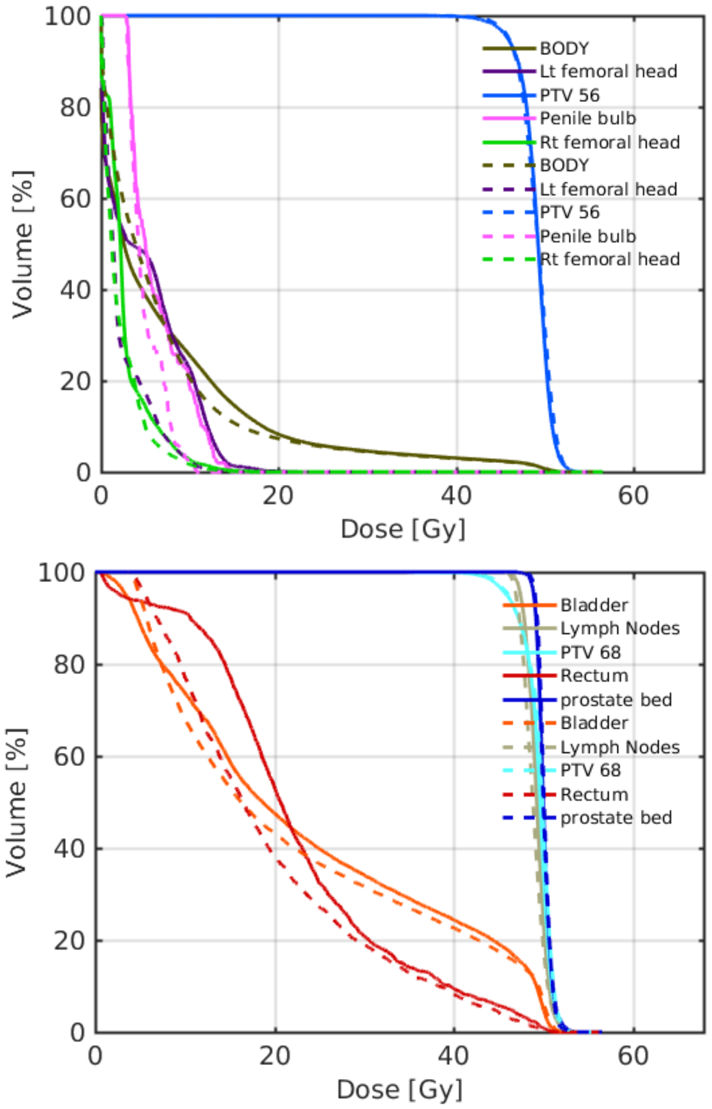

Figure 3.11 – DVH comparing the simulated annealing method (dashed lines) to greedy method (thick lines) for Prostate case

Table 3.7 – Dose statistics for Prostate case

Metric	SA method		greedy method		Coplanar method	
Objective function value	6.88×10^4		7.24×10^4		4.72×10^4	
Conformity Number	0.49		0.5		0.55	
Dose(Gy)	**Mean**	**Max**	**Mean**	**Max**	**Mean**	**Max**
Target	49	53.8	49.4	56.2	49.4	53.1
Skin	6.9	53.8	6.9	53.8	6.4	53.1
Bladder	22.5	53.7	23.5	53.5	26.2	52.3
Rectum	19.5	51.6	22.4	50.9	21.8	51.6
Penile bulb	4.9	10.6	6.2	14.5	0.3	1.2

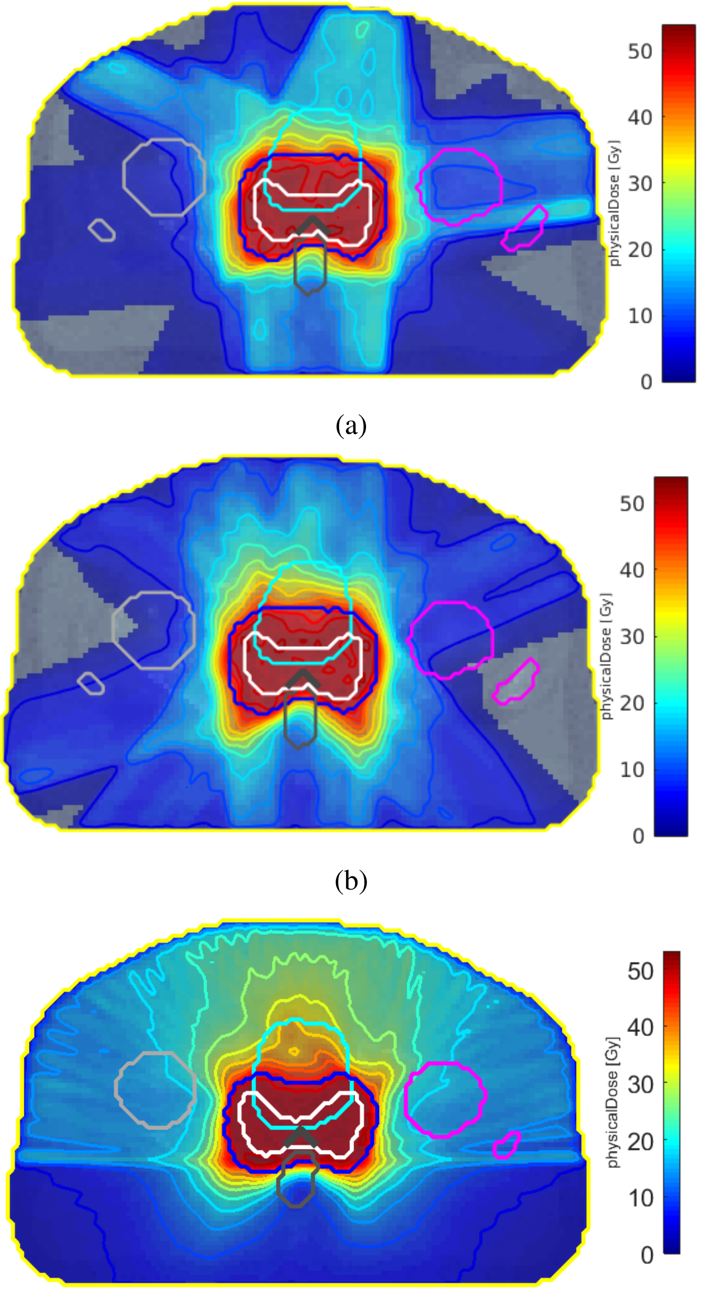

(a)

(b)

(c)

Figure 3.12 – Comparing Isodose Contours for Prostate using greedy method (a) SA method (b) and Coplanar method (b)

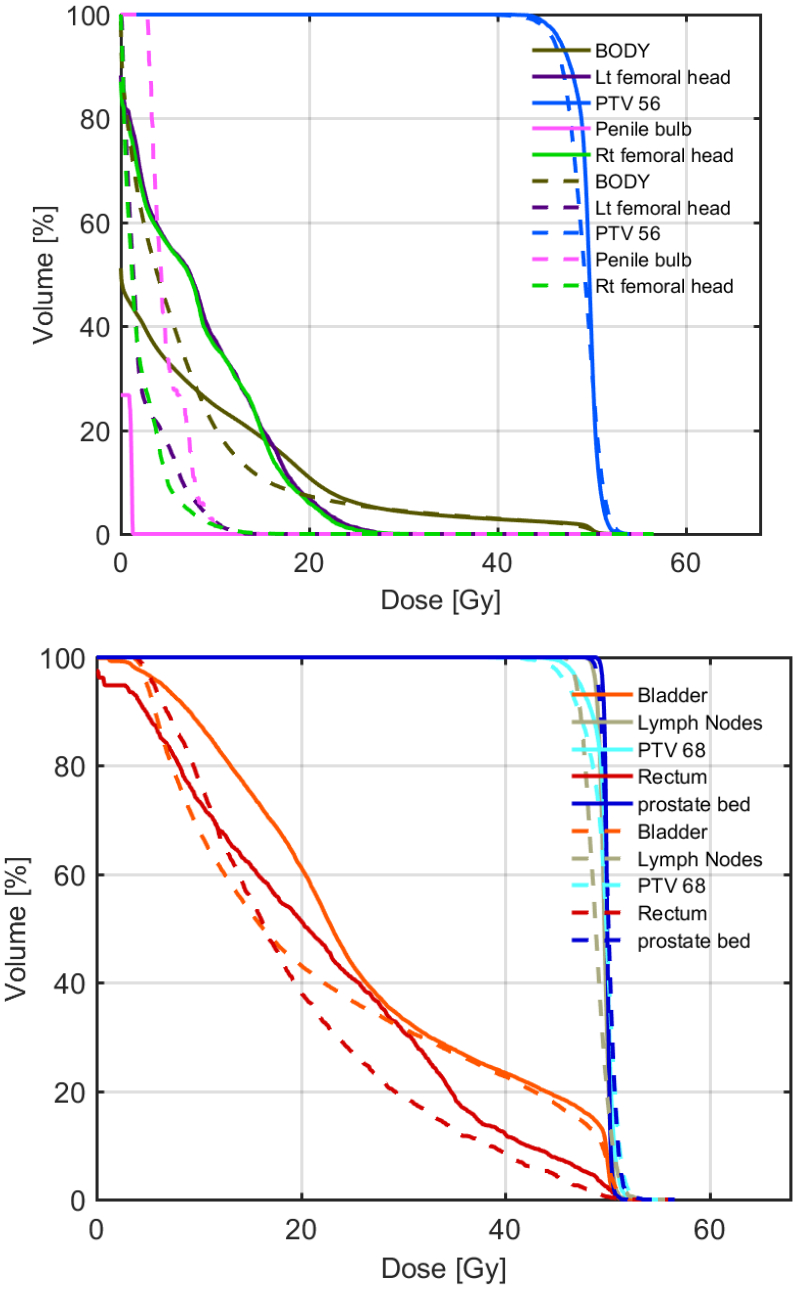

Figure 3.14 – DVH comparing the simulated annealing method (dashed lines) to Coplanar method (thick lines) for Prostate case

From the isodose contours shown in Figure 3.12 conformal dose is observed from the dose contours when using the SA method compared to the greedy and coplanar methods . We observed a higher dose region just outside the prostate and above the prostate using the coplanar method. This indicates a sub-optimal beam combination has been applied leading to fluence intensity that is concentrated in a particular region

. The trajectory comparison in figure 3.15 shows that the proposed SA method has a longer trajectory with 43 control points vs 10 control points for the greedy method and 37 control points for the coplanar method. Also the table 3.8 with a delivery time of 246s for SA method vs a delivery time of 87s for greedy method and 246s for the coplanar method. It is important to note that the fewer number of control points indicates the termination of the beam angle selection algorithm in the presence of a local minimum.

Metric	**SA method**	**greedy method**	**Coplanar method**
Estimated Delivery time	127s	87s	246s
No of control points	43	10	37

Table 3.8 – Comparing trajectory generated for Prostate case

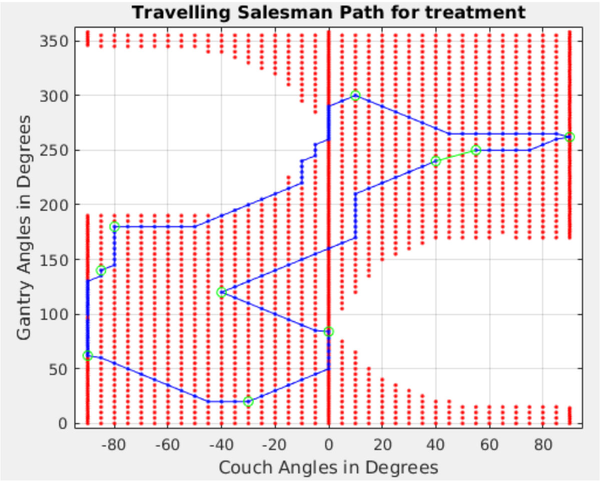

(a)

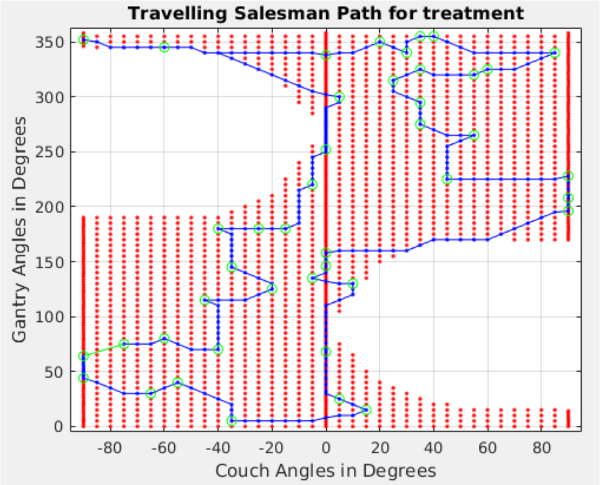

(b)

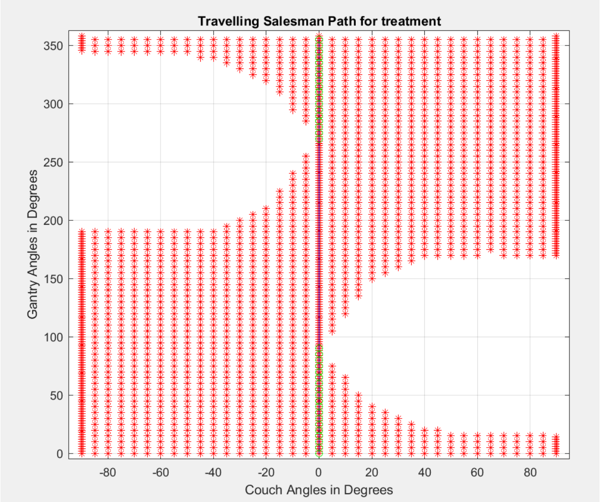

(c)

Figure 3.15 – Comparing Trajectories for Prostate using greedy method (a) SA method (b) and Coplanar method (c)

3.4 Discussion

The use of beam angle selection to generate non-coplanar trajectories for VMAT presents an opportunity to search a larger space to obtain optimal beam orientations for treatment. The consequence is that a huge number of solutions are possible to the resulting non-convex combinatorial optimization problem.

The beam angle selection methods that exist in literature (enumerated in section 3.1) limit the search space during fluence evaluation [93] and/or employ a two-step approach to overcome the non-convexity [77] which could lead to local solutions. The simulated annealing algorithm for non-coplanar VMAT treatment planning that we have presented is able to handle the problem of non-convexity by employing direct leaf trajectory optimization. The proposed algorithm has no restriction on the search space and thereby evaluates a very large number of possible treatment plans to obtain globally optimal treatment beams.

From the results in section 3.3, we observe dosimetric improvements in terms of organ-at-risk sparing is observed using the SA method such as: reduced mean dose to the core in TG-119 case (38%), the Heart in Liver case (38%) and the Rectum in Prostate case (14%). However, no significant differences are observed in the dose delivered to the target in all cases ($50Gy \pm 0.8$). We observed that there is a high dose region in the Liver case using the greedy method (figure 3.8a). This demonstrates the possibility of a local minimum when the beam selection algorithm is unable to escape this state and thus cannot find a global solution. The beam that is selected exists proximity to the treatment bed however the orientation is underneath the treatment bed. Such a beam encounters significant interference before it reaches the target in the tumor.

We found that the optimal beam orientations selected using the greedy method for all three patient cases were fewer in number and further apart in angular euclidean distance from each other. Conversely the SA method selects a large number of beams which are closer to each other to serve as active control points during treatment. The net effect of this during treatment delivery is no concentration of the high dose portions on organs such as the skin using the SA method.

Generally the SA method showed better organ-at-risk sparing compared to the coplanar method e.g reduced mean dose to the heart in the liver case and to the core in the TG-119 case. However, We have observed that in some cases the use of a non-coplanar trajectory created with the SA method does not lead to an imporved dosimetry compared to the coplanar trajectory. This is seen in the prostate case where the mean dose to the penile bulb and the Skin organs are lower for the coplanar method compared to the SA method. This difference in organ-at-risk sparing is reflected in the conformity number. An explanation is that these solutions from the coplanar method are locally optimal and is a function of the trajectory. The SA method in the search for global optimality may counter balance the sparing of an organs-at-risk with a higher mean dose to another organ-at-risk.

We observed that adding control points in the second stage to complete the trajectory could degrade the quality of the final plan if the intermediate control points are active during treatment. Such sub-optimal intermediate beam angles are excluded from the final direct leaf trajectory optimization along the selected non-coplanar trajectory. Indeed [77] affirms that such a trajectory that excludes intermediate beam angles may be realized by closing the MLC leaves or setting the dose rate to zero at when the machine traverses between two optimal beam angles.

Trajectory comparison shows that there is an increase in the number of control points when using the proposed SA method compared to the greedy method. But the increase in the trajectory length and delivery time are not significantly different to affect production time in clinical use. Compared to the coplanar method, the estimated delivery time for the SA method is lower in the Liver and the prostate case but conversely it is higer for the TG-119. The estimated delivery time is a function of the trajectory of the beam angles seleted and the time to deliver the desired dose to the target. The TG-119 case has a particularly complex shape and we see that more control points are needed for the trajectory and hence a higher delivery time for the SA method. For the liver and prostate cases there is a similar number of control points for both SA method and coplanar method so the lower delivery time for the SA method reflects an improved efficiency in dose delivery to the target.

Memory limitations during computation is a problem that can be encountered when implementing our proposed algorithm. The copy and storage of the dose influence matrix forms the bulk of the memory utilization during computation. We overcome this difficulty by using an increased beamlet size of $7mm \times 7mm$ and using a computer of large RAM (256GB). The effect of increasing the beamlet size is the reduction in the number of beamlets under consideration. This has a direct effect of reducing the number of columns of the dose influence matrix and thus reducing its size. Therefore makes it easier to store and transfer the dose influence matrix.

Future work is to evaluate this non-coplanar VMAT planning approach on a larger number of patient cases that have the cancer tumor located at different parts of the body. Another possibility in the future work is to include a delivery trajectory criterion during the beam angle selection phase so as to eliminate the need to insert intermediate beam orientations in the final phase.

CHAPTER

4

A SAMPLING-BASED APPROACH FOR NON-COPLANAR VMAT TREATMENT PLANNING USING RRT

We present a new method for non-coplanar VMAT treatment planning using Rapidly-exploring random trees. This algorithm is introduced to deal with the inefficient treatment trajectories that arises from inserting intermediate control points when beam selection methods are applied to non-coplanar VMAT treatment planning. The use of RRT method eliminates from aperture contention issues that could occur from such inefficient trajectories. The RRT method enables the simultaneous plan optimization and trajectory generation. The algorithm progressively samples the space of the input candidate beam orientations to build a tree consisting of nodes and edges. During the tree-construction, fluence intensity optimizaton is performed simultaneously to search for delivery trajectories with optimal dosimetry. A depth-first search is done after the tree construction to enumerate all valid trajectories on the tree. The trajectory which contains the treatment plan with the lowest objective function value is selected as the best. Treatment plans using Liver, TG-119 and Prostate cases were prepared and compared to a beam selection approach to non-coplanar VMAT planning. The results show that treatment plans of a comparable dosimetry to the beam selection approach can be obtained using this approach while obtaining a more efficient trajectory that is shorter in length, takes less time to deliver.

4.1 Introduction

VMAT improves delivery efficiency compared to conventional delivery methods such as fixed gantry IMRT due to a reduction in the delivery time and cumulative dose recieved by the patient. [42]. In non-coplanar VMAT, a simultaneous rotation of the linear accelerator gantry and the treatment bed is used to orient the beam for patient irradiation. The use of non-coplanar beams provides an opportunity for improved dosimetry over co-planar methods in terms of better target coverage and organs-at-risk (OAR) avoidance. Several authors have argued for the adoption of non-coplanar VMAT for use in treatment [84]. Non-coplanar VMAT has shown better OAR sparing compared to coplanar VMAT in several clinical studies [87, 88, 89].

But despite the advantages of non-coplanar VMAT, they are still not widely adopted for use at most radiotherapy treatment centers. The difficulty is in the design of the non-coplanar beam trajectories and the choice of the beam orientations that will form part of the trajectory. There exists a large number of possible trajectories and a method is required to select a trajectory containing beams that delivers the optimal dose distribution in the most efficient manner.

Several strategies have been proposed over the years for generating non-coplanar trajectories. The earliest methods relied on the experience of the treatment planner to manually define a non-coplanar trajectory [92, 87]. Such manual methods are not optimized and are only applicable to specific anatomies.

Further developments have seen the use of tumor geometric information for generating non-coplanar trajectories for VMAT treatment. The author in [85] presents a method that uses the geometrical information obtained from the beam-eye-view (BEV) to score different beam orientations. Then uses a hierarchical clustering algorithm determines a continuous couch-gantry trajectory from the beam scores by merging several discontinuous sub-arcs. The method presented by [86] uses a similar geometric approach with a graph search algorithm to determine a minimum-cost trajectory from a cost map. The cost map is calculated for each beamlet by ray-tracing it's intersection with the OARs. These geometric scoring methods suffer from aperture contention issues as adjacent beams of similar beam scores could result in uncorrelated MLC apertures shapes. To overcome aperture contention issues, [137] introduced TORUS which uses sectioning of the tumor geometry to generate a score for connected BEV regions. Dijkstra's algorithm is used to generate a trajectory from the resulting graph optimization problem.

More recent studies use a beam angle selection method to generate non-coplanar treatment trajectories [77, 93]. The selected beams could be far apart so intermediate way-points are introduced to form a complete trajectory. These studies differ mainly in the approach to beam angle selection. The method presented by [77] selects treatment beams using a genetic algorithm. [93] considers three beam selection strategies i.e. greedy strategy, look ahead strategy and gradient strategy. Both authors solve a traveling salesman problem to connect the selected beam angles to form a treatment trajectory. The difficulty is that beam selection is a highly non-convex and combinatorial optmization problem. A large number of solutions are possible leading the authors to restrict the solution space. Moreover, intermediate way-points are introduced to create a valid trajectory but are dosimetrically sub-optimal and could degrade the plan quality.

Non-coplanar VMAT planning imposes a dual goal to obtain a non-coplanar trajectory and a dosimetrically optimal VMAT plan along this trajectory. We note that all the aforementioned methods use a two-step approach of first designing a non-coplanar trajectory and then preparing a VMAT plan along this trajectory. By separating both processes it is possible to obtain a high quality VMAT plan on an undeliverable non-coplanar trajectory or a very efficient non-coplanar trajectory containing a sub-optimal VMAT plan. It becomes evident that the trajectory generation process must run concurrently with the VMAT optimization process.

To handle this problem, we propose a sampling-based non-coplanar VMAT planning algorithm that is capable of simultaneously generating a non-coplanar trajectory while performing VMAT treatment plan optimization. Another motivation for this work is to handle the problem of inserting intermediate control points in the trajectory as seen in methods that employ beam angle selection. Our proposed algorithm does not insert intermediate control points therefore, the trajectory obtained is a complete, valid and deliverable trajectory.

The contribution of this chapter is an algorithm inspired from rapidly-exploring random trees (RRT^*) for non-coplanar VMAT treatment planning. The algorithm progressively samples the space of the candidate beam orientations while evaluating the fluence contribution of each beam in an unrestricted manner to build a tree. Tree-construction and VMAT optimization are performed concrrently and a depth-first search is done at the end of the tree construction to select the lowest cost trajectory. We have also introduced two new metrics based on the bending energy that can be used to measure the smoothness of the resulting trajectory.

This chapter is organized as follows: section 4.6 presents the RRT^* non-coplanar VMAT planning algorithm, section 4.8 presents the hardware and software details for the implementation as well as details of the three patient cases and the metrics used in the evaluation study. can be found in section. The results of the evaluation study are presented in 4.9 and discussed in section 4.10.

4.2 Rapidly-exploring random trees (RRT)

The control of complex non-linear systems becomes very challenging as the number of degrees of freedom/ state-space dimensions increases [138]. Rapidly-exploring random trees are a class of sampling-based agorithms used in trajectory planning and control of complex systems. RRT algorithms are capable of handling such high dimensionality of complex systems. RRTs employ a probabilistic approach by continuously sampling a state space at randomn starting from a defined point $\mathbf{p}_{start}$ towards a goal point $\mathbf{p}_{end}$.

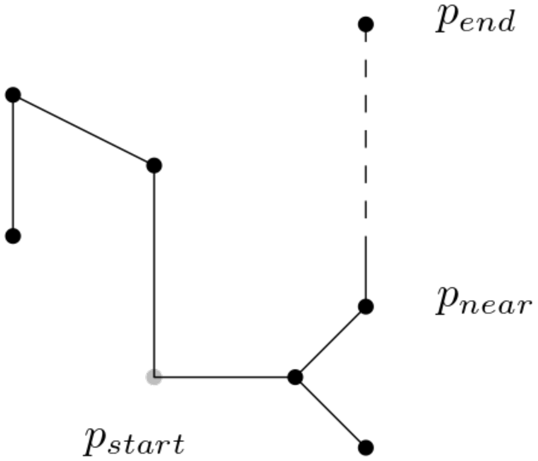

Figure 4.1 – Illustration of the RRT sampling process, discovered paths are shown with thick lines while the undiscovered paths are shown with dashed lines

Figure 4.1 illustrates the process of sampling of RRT algorithm. Starting from a defined point denoted as $\mathbf{p}_{start}$, the algorithmn selects a randomn point in the configuration space, $\mathbf{p}_{rand}$ and then finds the nearest point that exists already on the tree $\mathbf{p}_{near}$. A finite step is performed from $\mathbf{p}_{near}$ towards $\mathbf{p}_{rand}$ in order to find a new point $\mathbf{p}_{new}$ that is added to the tree. This process of node discoverly is performed iteratively until $\mathbf{p}_{new}$ becomes the sames as the goal point $\mathbf{p}_{end}$. The pseudo-code of the RRT algorithm is shown in algorithm 6.

Algorithm 6 Pseudocode for RRT algorithm

```
$Init:\ \mathbf{p}_{start}, \mathbf{p}_{end}, \mathbf{T}$
$\mathbf{T} \leftarrow addVertex(\mathbf{T}, \mathbf{p}_{start})$
repeat
    $\mathbf{p}_{rand} \leftarrow randConfiguration()$
    $\mathbf{p}_{near} \leftarrow nearestNeighbour(\mathbf{T}, \mathbf{p}_{rand})$
    $\mathbf{p}_{new} \leftarrow steer(\mathbf{p}_{near}, \mathbf{p}_{rand})$
    $\mathbf{T} \leftarrow addEdge(\mathbf{p}_{near}, \mathbf{p}_{new})$
until $\mathbf{p}_{new} = \mathbf{p}_{end}$
return $\mathbf{T}$
```

RRTs have been demonstrated to be probabilistically complete so that they are capable to find a path from $\mathbf{p}_{start}$ to $\mathbf{p}_{end}$ if one exists. RRTs also have very good exploring capabilities as the algorithm tends towards the unexplored regions of the configuration space with each iteration.

The author in [139] applies RRT for the kinodynamic motion planning for complex systems. The problem presented is to plan motion systems that have nonlinear dynamics in a high-dimensional configuration space with obstacles present. The authors developed a randomized planning approach for trajectory planning in high-dimensional state spaces using rapidly exploring random trees (RRT). Experimental verification was performed to determine the trajectories for hovercrafts and satellites in an enviroment with obstacles. The results show that after exploring many configuration states, a trajectory could be found successfuly with the

RRT algorithm.

In another work [140], RRT is applied to object grasping and path planning for mobile manipulators. The task is to bring the robot close to the goal configuration from a start configuration in order to grasp an object. RRT is applied to the planning phase to move the robot from start to goal while avoiding obstacles. The experiments are performed using a 10 degree-of-freedom Puma® robot successfully performs the path planning phase of the complex pick-and-place tasks in simulation.

Another application is the use of RRT algorithm for generating maneuver profiles for unmanned aerial vehichles (UAVs) [141]. This work uses RRT in the first step of the trajectory planning layer, to solve the time-dependent path planning problem of UAVs. One aim of using RRT in this method is to take advantage of its quick spreading ability that allows the exploration of a large portion of the configuration space.

In radiotherapy, the first application of a sampling-based approach is the Monte Carlo tree search algorithm (MCTS) for generating a static beam IMRT plan [103]. It was introduces to handle the inter-dependence of the beam trajectory and the beam parameters. The MCTS technique employs a tree structure to search for possible treatment trajectories while evaluating each encountered node. The nodes are evaluated using upper confidence bound applied to trees (UCT) which is defined as:

$$UCT = \overline{X}_j + C_p \sqrt{\frac{ln(n)}{n_j}} \tag{4.1}$$

where $\overline{X}_j$ is the average objective function value calculated over the number of visits on the node j, n_j is number of time the node j has been visited, C_p is a constant and n is the number of time the tree node has been visited. MCTS uses the UCT value to choose the next node to visit by selecting the node with the highest UCT value. MCTS selects a random node when all possible nodes to be visited have the same UCT value. The authors defined the objective function value $\overline{X}_j$ as a minimization of the linear combination of the mean and maximum dose to the PTVs and OARs [103]. The MCTS algorithm was evaluated on a chest wall case and a brain case and compared to a coplanar and a 4π treatment plans developed for the same patient cases. The results show that MCTS found trajectories that lead to an improved dosimetry compared with the coplanar treatment plan. Compared to the 4π treatment plan however presented a better OAR sparing compared to MCTS.

To the best of our knowledge, our work is the first attempt to produce a non-coplanar VMAT treatment trajectory using a sampling-based approach. It is also the first attempt to model the generation of a non-coplanar VMAT treatment trajectory through the use of rapidly-exploring random trees.

4.3 Asymptomatic sub-optimality of the RRT algorithm

The optimality of a path planning algorithm measures its ability to generate the shortest path, thus leading to an improved efficiency. Optimality can be measured using several criteria such as path length, collision-free space, execution time, and the total number of turns. It has been shown that the probability of RRT algorithm to converge to an optimal solution is 0 as the number of samples approaches infinity (∞) [142]. We do not detail the formal proof here as it is beyound the scope of our study. The implication is that RRT algorithm does not necessarily guarantee to find the least cost path. Conversely, this implies that the RRT algorithm converges to a suboptimal solution with probability of 1 as the algorithm progresses.

A new variant of RRT algorithm called RRT* was introduced to deal with the problem of asymptomatic sub-optimality of RRT algorithms. The RRT* inherits the asymptotic optimality of the RRG algorithm while maintaining a tree structure of RRT algorithm. This is done by reconfiguriation of the tree-structure to discover lower cost nodes to reach nodes that already exist in the tree.

4.4 Improved Rapidly-exploring random trees (RRT*)

RRT* is a state-of-the art technique widely used in planning trajectory for robots [142]. It belongs to a class of informative incremental sampling-based motion planning algorithms namely rapidly-exploring random trees/graphs (RRT/RRG). RRT* is an improved version of RRT. It combines the asymptotic optimality of RRG and the tree-like structure of RRT.

The strength of RRT* lies in its ability to explore the candidate space by rapidly growing a random tree while evaluating the trajectory cost function. The advantage of RRT* is that it can handle complex high-dimensional problems. They are particularly suitable for combinatorial optimization where a set of beam angles is chosen from a larger set.

When compared to RRT algorithm, RRT* algorithm quickly discovers the initial path and then improves its quality in subsequent iterations to produce a near-optimal path as the number of iterations approaches infinity. However, its has a slower rate of convergence compared to RRT because it requires many iterations to optimize the initial path [143].

RRT* explores the candidate space by rapidly growing a random tree and evaluating a cost function on trajectories on the tree. The cost function is used to steer the search towards the regions of the candidate space that have not been explored as the best path returned converges to the optimum cost function. RRT* has been used for planning dynamic trajectories for robots [144] and for exploring conformal energy landscapes of molecules [145].

4.5 Motivation for choosing RRT^* algorithm

Our original motivation for choosing the RRT^* is that it offers the possibility to generate a path while simultaneously evaluating a path objective. This property is quite similar to our objective of combining the non-coplanar trajectory generation phase with the VMAT plan optimization phase during treatment planning. Thus, a combination of both steps into a single algorithm will enable the generation of a non-coplanar VMAT plan that takes all constraints into account at every point during the creation of the delivery trajectory.

Previous authors have noted that beam selection is an NP-hard combinatory optimization problem [124] making it very difficult to combine the beam selection process with VMAT treatment planning constraints. The beam selection methods despite being the pre-dominant approach for selecting non-coplanar beam trajectories are also prone to fall into a local minimum especially when several constraints are considered concurrently. Thus another reason for choosing RRT^* algorithm is to use its space exploring and coverage capability to escape local solutions.

4.6 New RRT^* algorithm for Non-coplanar VMAT planning

The non-coplanar VMAT planning can be seen as a navigation through a connected bounded subset of a k-dimensional euclidean space guided by an information metric on the space.

In our case, $k = 2$ is parametrized by each couch-gantry angle pair to which we refer subsequently as nodes. The candidate beam angle space $\mathbb{B}$ can be represented by a graph $G(N, E)$. The nodes of this graph are defined as $N = \{(c_1, g_1), (c_2, g_2), ...(c_n, g_n)\} = \{\mathbf{n}_1, \mathbf{n}_2, ...\mathbf{n}_n\}$. The information metric in our space is the value of the the cost function $f(\mathbf{d})$ resulting from a set of nodes that constitute a valid trajectory.

Given the graph of the candidate beam angle space $\mathbf{G}$ and a starting node $\mathbf{n}_{init}$ the optimal planning problem is to determine an optimal trajectory $\mathbf{X}_{path}$ containing a connected set of nodes such that the cost function $f(\mathbf{d})$ (previously defined in equation 1.6) is the global minimum. The modified RRT* VMAT algorithm 7 is proposed in order to explore the candidate beam angle space to simultaneously generate an optimal VMAT treatment plan and a smooth non-coplanar trajectory. The procedure for our proposed algorithm is illustrated in figure 4.2.

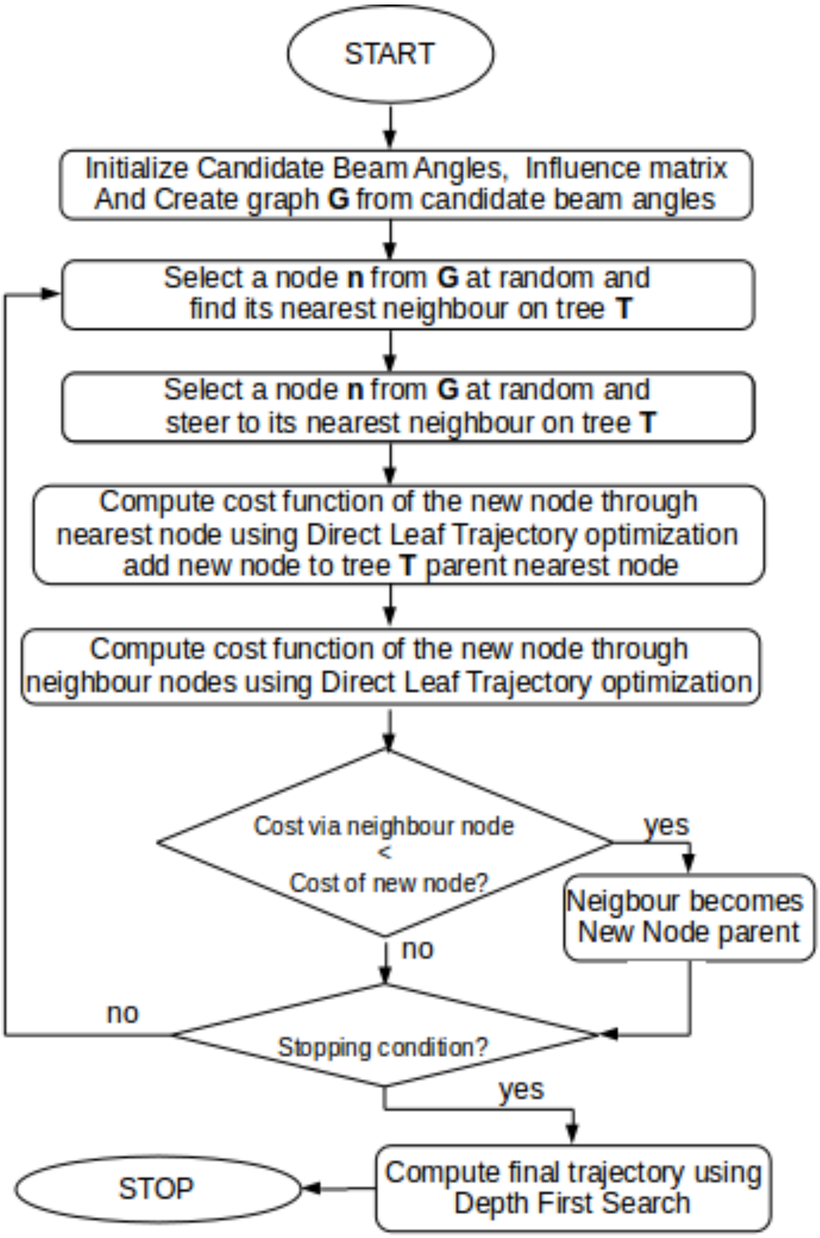

Figure 4.2 – Flowchart showing the procedure for RRT^* Non-coplanar VMAT planning algorithm

Algorithm 7 starts with an initial node $\mathbf{n}_{init}$ and the graph $\mathbf{G}$ as input. $\mathbf{n}_{init}$ serves as the starting node and is chosen using a first order estimate of the steepest descent direction using a projected gradient of the objective function [93].

$$||(-\nabla f(\mathbf{d}))||_{+} = \sqrt[2]{\sum_{i \in b} \left(- \frac{\partial f(\mathbf{d})}{\partial x_i^b} \right)_{+}^{2}} \tag{4.2}$$

Algorithm 7 RRT* algorithm for non-coplanar VMAT

```
$Init$ : $\mathbf{V} \leftarrow \{\mathbf{n}_{init}\}$, $\mathbf{E} \leftarrow \emptyset$, $\mathbf{G} \leftarrow graph(\mathbb{B})$, $i \leftarrow 0$
$choose\ \epsilon\ using\ \ equation$ 3.7
for $i = 1$ to $N$ do
    $\mathbf{T} \leftarrow (\mathbf{V}, \mathbf{E})$
    $\mathbf{n}_{rand} \leftarrow datasample(\mathbf{G}, i)$
    $\mathbf{n}_{near} \leftarrow knnsearch(\mathbf{T}, \mathbf{n}_{rand})$
    $\mathbf{n}_{new} \leftarrow steer(\mathbf{n}_{near}, \mathbf{n}_{rand}, \mathbf{G}, \epsilon)$
    if $isvalid(\mathbf{n}_{new})$ then
        $\mathbf{V}^* \leftarrow \mathbf{V} \cup \mathbf{n}_{new}$; $\mathbf{n}_{min} \leftarrow \mathbf{n}_{near}$
        $\mathbf{p}_{\mathbf{n}_{new}} = getPathfromStart(\mathbf{T}, \mathbf{n}_{near}, \mathbf{n}_{init}) \cup \mathbf{n}_{new}$
        $f_{\mathbf{n}_{new}}(\mathbf{d}) = directLeafOptim(\mathbf{p}_{\mathbf{n}_{new}})$
        $f_{\mathbf{n}_{min}}(\mathbf{d}) \leftarrow f_{\mathbf{n}_{new}}(\mathbf{d})$
        $\mathbf{X}_{neighbour} \leftarrow Neighbours(\mathbf{T}, \mathbf{n}_{new}, \eta)$
        if $isnotempty(\mathbf{X}_{neighbour})$ then
            for $all$ $\mathbf{n}_{neighbour} \in \mathbf{X}_{neighbour}$ do
                $\mathbf{p}_{\mathbf{n}_{new}} = getPathfromStart(\mathbf{G}, \mathbf{n}_{neighbour}, \mathbf{n}_{init}) \cup \mathbf{n}_{new}$
                $f_{\mathbf{n}_{new}}(\mathbf{d}) = directLeafOptim(\mathbf{p}_{\mathbf{n}_{new}})$
                if $f_{\mathbf{n}_{neighbour}}(\mathbf{d}) < f_{\mathbf{n}_{min}}(\mathbf{d})$ then
                    $\mathbf{n}_{min} \leftarrow \mathbf{n}_{neighbour}$; $f_{\mathbf{n}_{min}}(\mathbf{d}) \leftarrow f_{\mathbf{n}_{neighbour}}(\mathbf{d})$
                end if
            end for
            $\mathbf{E}^* \leftarrow \mathbf{E}^* \cup \{\mathbf{n}_{min}, \mathbf{n}_{new}\}$
            for $all$ $\mathbf{n}_{neighbour} \in \mathbf{X}_{neighbour} \setminus \mathbf{n}_{min}$ do
                if $f_{\mathbf{n}_{neighbour}}(\mathbf{d}) < f_{\mathbf{n}_{neighbour}}(\mathbf{d})^{i-1}$ then
                    $\mathbf{n}_{parent} \leftarrow Parent(\mathbf{n}_{neighbour})$
                    $\mathbf{E}^* \leftarrow \mathbf{E}^* \setminus \{\mathbf{n}_{parent}, \mathbf{n}_{neighbour}\}$
                    $\mathbf{E}^* \leftarrow \mathbf{E}^* \cup \{\mathbf{n}_{new}, \mathbf{n}_{neighbour}\}$
                end if
            end for
        end if
    end if
    $\mathbf{V} \leftarrow \mathbf{V}^*$; $\mathbf{E} \leftarrow \mathbf{E}^*$
end for
leaves $\leftarrow dfsPreorder(\mathbf{T})$
$\mathbf{X}_{path} \leftarrow getmainPath(\mathbf{T}, \textbf{leaves})$
return $\mathbf{X}_{path}$
```

$||a||_+$ is a positivity function defined as max(0,a). **T** is a tree data-structure that is used to store the discovered nodes. **T** is composed of vertices **V** and edges **E**.

The nodes are stored in **V** and their corresponding edges stored in **E**. **T** also holds information about the parent node of each nodes that is discovered by the algorithm.

The algorithm progresses iteratively by sampling the candidate beam angle space using the matlab function *datasample()*. Given a graph **G** the function *datasample()* : $(\mathbf{G}) \mapsto \mathbf{n}_{rand}$ returns an undiscovered node sampled uniformly at random from the graph. The discovery of new nodes by the algorithm is illustrated in figure 4.3.

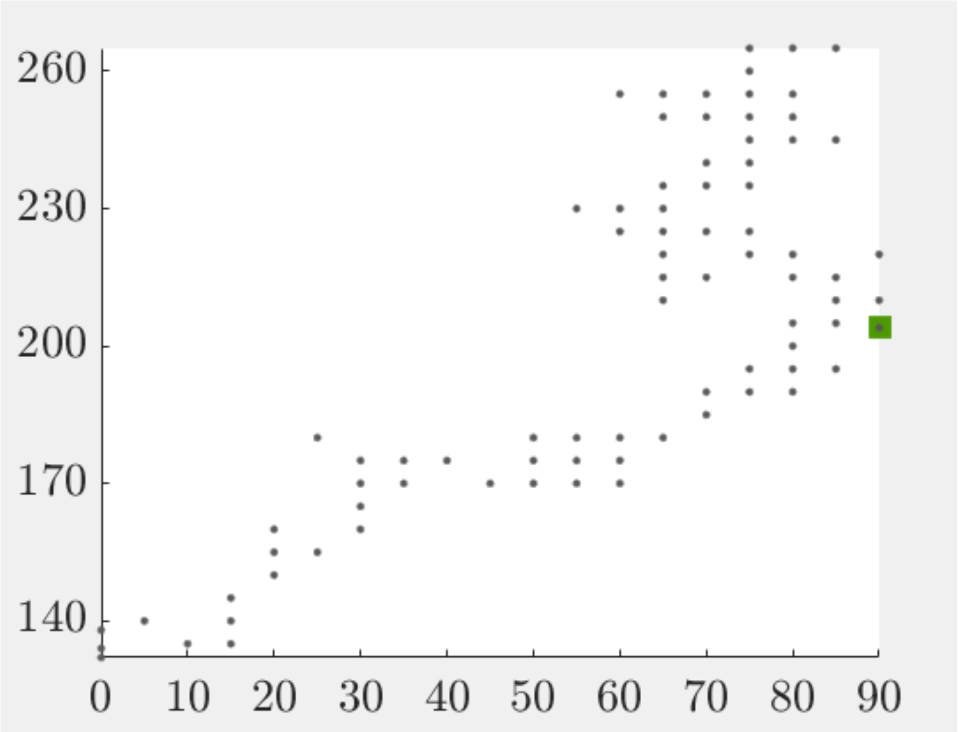

Figure 4.3 – Figure showing *RRT** algorithmn during node discovery. horizontal-axis = couch angle (degrees) and vertical-axis = gantry angle (degrees) The black dots denote discovered nodes at a specific couch-gantry angle while the green box denotes the start node $\mathbf{n}_{init}$

Subsequently, a search is performed using the matlab function *knnsearch()* to obtain the nearest neighbor node to $\mathbf{n}_{rand}$ in graph $\mathbf{G}$. Given a tree $\mathbf{T}$ and an input node $\mathbf{n}_{rand}$, the function *knnsearch()* : $(\mathbf{T}, \mathbf{n}_{rand}) \mapsto \mathbf{n}_{near}$ performs a nearest neighbor search to return the node on the tree closest to the input node.

The next step is to perform a steering operation such that node $\mathbf{n}_{rand}$ is reachable from the node $\mathbf{n}_{near}$. Given two nodes, the function *steer()* : $(\mathbf{n}_{near}, \mathbf{n}_{rand}, \mathbf{G}) \mapsto \mathbf{n}_{new}$ returns a node $\mathbf{n}_{new}$ such that $\| \mathbf{n}_{new} - \mathbf{n}_{rand} \|$ is minimized under the constraint $\| \mathbf{n}_{new} - \mathbf{n}_{near} \| \leq \epsilon$.

The steer function is implemented using the relation:

$$\mathbf{n}_{near} = \begin{bmatrix} c_{new} \\ g_{new} \end{bmatrix} = \begin{bmatrix} c_{near} \\ g_{near} \end{bmatrix} + \mathbf{s}.\epsilon \tag{4.3}$$

where $\mathbf{s}$ is a random vector $\mathbb{R}^2$ such that $\mathbf{s}(i)$ takes a value of either 0 or 1.

The node $\mathbf{n}_{new}$ is then checked for validity using the function *isvalid* which returns true if it is possible to reach node $\mathbf{n}_{new}$ from $\mathbf{n}_{near}$ or false otherwise. If valid, $\mathbf{n}_{new}$ is added to the tree $\mathbf{T}$.

The cost function value $f_{\mathbf{n}_{new}}(\mathbf{d})$ of the path $\mathbf{p}_{\mathbf{n}_{new}}$ starting from the root node $\mathbf{n}_{init}$ up to $\mathbf{n}_{new}$ while passing through $\mathbf{n}_{near}$ is calculated in the next step. $\mathbf{p}_{\mathbf{n}_{new}}$ is obtained by using the function *getPathfromStart*. Given a tree $\mathbf{T}$, a start node $\mathbf{n}_{init}$ and an end node $\mathbf{n}_{near}$, the function *getPathfromStart* : $(\mathbf{T}, \mathbf{n}_{near}, \mathbf{n}_{init}) \mapsto \mathbf{p}_{\mathbf{n}_{new}}$ recursively iterates through each node encountered from the end node to start node to obtain the indices of their parent node. These node indices represent a path. These node indices are concatenated together with the index of $\mathbf{n}_{new}$ and then used to select the corresponding columns from the dose influence matrix that are used in the objective function calculation.

We make use of an in-house implementation of the direct leaf trajectory optimization in the function *directLeafOptim* to calculate the cost function value [80]. The use of direct leaf trajectory optimization enables us to take into account the machine constraints and MLC leaf constraints during objective function calculation. The formulation of the optimization problem is convex and so are guaranteed a solution using commercially available solvers[72]. Another advantage that this method enables the calculation of the VMAT treatment plan in a single step by avoiding leaf sequencing. Given a path $\mathbf{p_n}$, created from the start node $\mathbf{n}_{init}$ and end node $\mathbf{n}$ using *getPathfromStart*, the function $directLeafOptim : (\mathbf{p_n}) \mapsto f_n(\mathbf{d})$ returns the final cost function value $f_n(\mathbf{d})$ using direct leaf trajectory optimization. This corresponds to obtaining the minimum of the optimization problem described in equation 1.20. We save this path and it's cost as the minimum cost path to reach node $\mathbf{n}_{new}$.

The next step is to determine all the neighboring nodes of $\mathbf{n}_{new}$. Given a tree, a node $\mathbf{n}$ and a distance parameter η in degrees, the function $Neighbours : (\mathbf{T}, \mathbf{n}, \eta) \mapsto \mathbf{X}_{neighbour}$ returns a list of nodes located at a distance η from $\mathbf{n}$ on the tree.

The next step in the algorithm is to search through all neighbor nodes to see if a lower cost alternative path to this node can be discovered by passing through $\mathbf{n}_{new}$. If this a lower cost alternative path is found from a neighboring node, $\mathbf{n}_{new}$ replaces the parent of this neighboring node. For each neighbour node $\mathbf{n}_{neighbour}$, we determine the path $\mathbf{p}_{\mathbf{n}_{new}}$ starting from the root node $\mathbf{n}_{init}$ up to $\mathbf{n}_{new}$ while passing through $\mathbf{n}_{neighbour}$ using the function *getPathfromStart* as already described. For each neighbour node $\mathbf{n}_{neighbour}$ who's path $\mathbf{p}_{\mathbf{n}_{new}}$ is determined, we calculate the resulting cost function value using $\mathbf{p}_{\mathbf{n}_{new}}$ (lines 13-21). If the neighbor nodes has a lower cost to reach the new node $\mathbf{n}_{new}$, it designated as the minimum cost node $\mathbf{n}_{min}$. The minimum cost node $\mathbf{n}_{min}$ becomes the parent of the newly discovered node $\mathbf{n}_{new}$.

After a fixed number of iterations N, the algorithm has generated a tree with all discovered nodes and their parent nodes. A function *dfsPreorder* is used to determine all terminal nodes on the tree. The *dfsPreorder* is an implementation of the iterative depth-first search [146]. Given a tree, the function $dfsPreorder : (\mathbf{T}) \mapsto$ **leaves** returns a list of terminal nodes on the tree by exploring, as far as possible, each branch of the tree starting from the root node. The algorithm for *dfsPreorder* function can be found in 8.

Algorithm 8 dfsPreorder by Iterative Depth-first search

```
$Init$ : $\mathbf{G}$, $\mathbf{Visited} \leftarrow \emptyset$, $\mathbf{S} \leftarrow stack$, $\mathbf{n} \leftarrow \mathbf{n}_{init}$
$\mathbf{S}.push(\mathbf{n})$
while $\mathbf{S}$ is not empty do
    if $\mathbf{n} \notin \mathbf{Visited}$ then
        $\mathbf{Visited} \leftarrow \mathbf{Visited} \cup \mathbf{n}$
        for $all$ $\mathbf{n}_{child} \in childNodes(\mathbf{G}, \mathbf{n})$ do
            $\mathbf{S}.push(\mathbf{n}_{child})$
        end for
    else
        $\mathbf{n} \leftarrow \mathbf{S}.pop()$
    end if
end while
$\mathbf{leaves} \leftarrow sort(\mathbf{Visited}, 'ascending')$
return $\mathbf{leaves}$
```

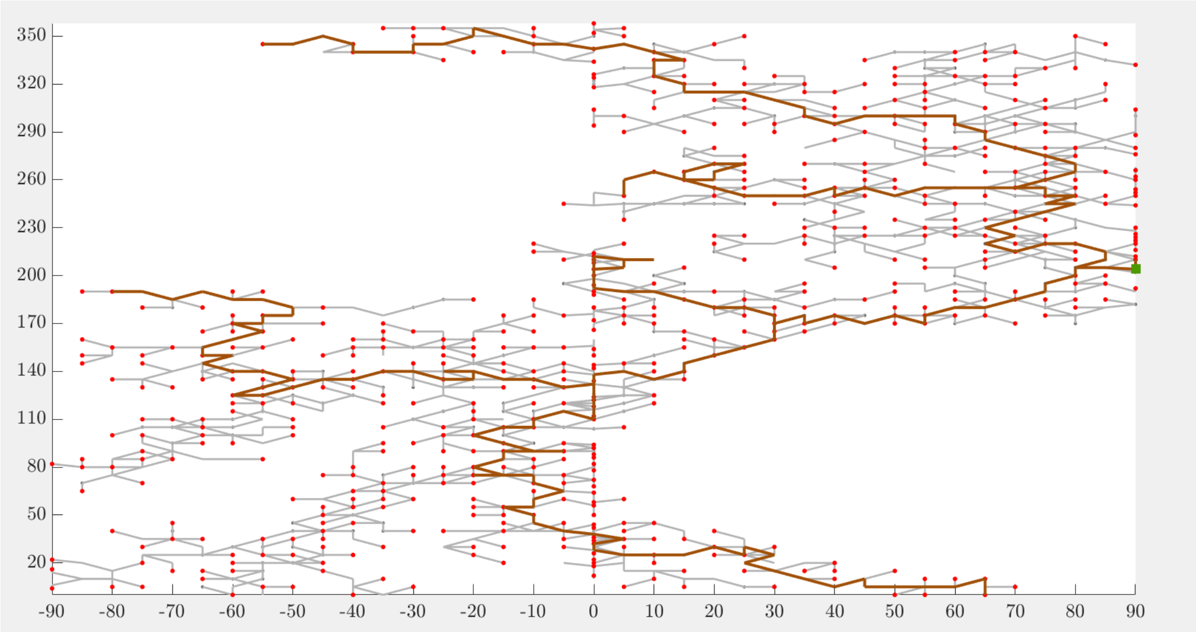

Figure 4.4 – Figure showing RRT^* algorithm after *dfsPreorder*, horizontal-axis = couch angle (degrees) and vertical-axis = gantry angle (degrees). The brown colored line connects discovered nodes starting from the root node. Each branch of the tree corresponds to a different trajectory that is discovered.

The discovered branches of $\mathbf{T}$ are illustrated in figure 4.4 and corresponds to different trajectories. Each leaf in the set **leaves** is a terminal node in a branch of the tree $\mathbf{T}$ starting from the root node $\mathbf{n}_{init}$. Each terminal node in **leaves** has an associated path cost to reach it from the root node. The path linking the lowest cost terminal node to the root node is chosen as the best path using the function *getmainPath*. Given a tree and a list of terminal nodes, the function $getmainPath : (\mathbf{T}, \mathbf{leaves}) \mapsto \mathbf{X}_{path}$ returns a list of nodes traversed from the lowest cost terminal node to the root node. The final path returned by algorithm 9 as $\mathbf{X}_{path}$.

Algorithm 9 getmainPath by searching for the lowest cost path

```
$Init :$ $\mathbf{G}$, leaves, $\mathbf{n}_{init}$, $\mathbf{X}_{path} \leftarrow \emptyset, f_{\mathbf{n}_{min}}(\mathbf{d}) \leftarrow \infty$
for $each\ leaf \in$ leaves do
    $\mathbf{p}_{\mathbf{n}_{leaf}} = getPathfromStart(\mathbf{T}, \mathbf{n}_{leaf}, \mathbf{n}_{init})$
    if $f_{\mathbf{n}_{leaf}}(\mathbf{d}) < f_{\mathbf{n}_{min}}(\mathbf{d})$ then
        $\mathbf{X}_{path} \leftarrow \mathbf{p}_{\mathbf{n}_{leaf}}$
    end if
end for
return $\mathbf{X}_{path}$
```

4.7 Modifications made to *RRT** for non-coplanar VMAT planning

We have made some modifications to the original *RRT** algorithm in order to adpat it to the non-coplanar VMAT treatment planning process. The first modification is the *steer()* function whose relation is defined in equation 4.3. The *steer()* function represents the motion of the system from one configuration to the another. Most applications that make use of *RRT** for path planning model the *steer()* function depending on the kinematics or dynamics of the system under consideration [138].

The particularity of the linear accelerator performing a non-coplanar treatment delivery prohibits an arbitrary motion from one configuration to the other. From a given position of the couch and gantry linear accelerator can only move to 8 possible configurations as illustrated in figure 4.5 and this gives rise to the the *steer()* function in equation 4.3.

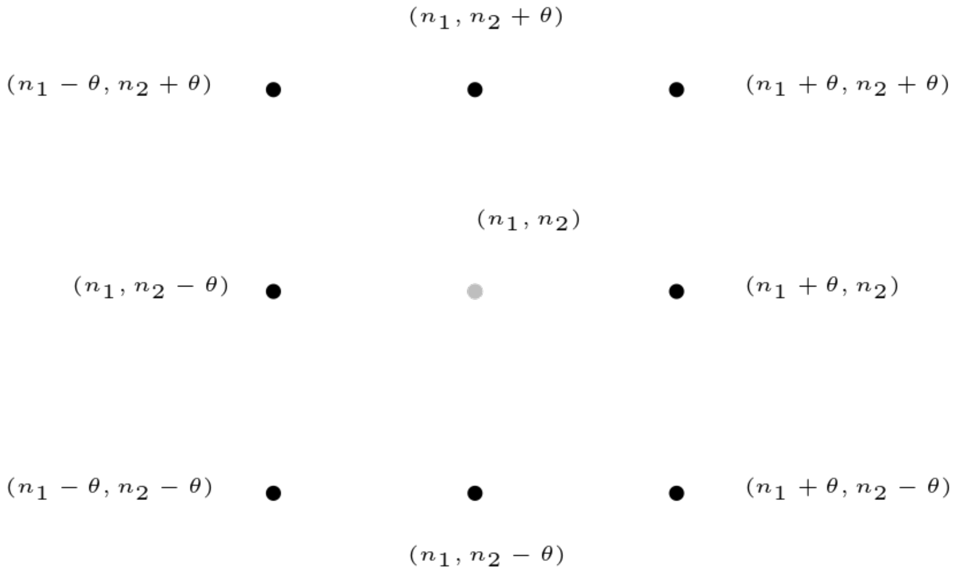

Figure 4.5 – Figure showing the 8 possible motions for a linear accelerator froma given couch-gantry angle (n_1, n_2) where θ represents the smallest allowed angular displacement of the linear accelerator and is equivalent to the discretization used to create all couch-gantry angle pairs

Another modification that we have introduced is in the computation of the cost function $f(\mathbf{d})$. Most applications of RRT^* to path planning consider the path cost to be a function of the state space configuration. Such that for a system whose position configuration is represented as 2-D cartesian co-ordiantes, a path-cost can be calculated using Euclidean, Malahanobis or Hausdorff distance [147]. For application to non-coplanar VMAT treatment planning, we have chosen to model the computation of path cost as the evaluation of the treatment objectives. In other words, we want the algorithm to generate a path that fufils the treatment objectives as defined by the objective function $f(\mathbf{d})$ in equation 1.6.

Finally, a key difference between our algorithm and classical path planning algorithms is the absence of a defined goal configuration. We have seen in section 4.2 that most sampling based planners define a start configuration $\mathbf{p}_{start}$ and an end configuration $\mathbf{p}_{end}$ so as to terminate the algorithm when the end configuration is attained. The RRT^* algorithm defines a fixed number of iterations N after which the algorithm is stopped. The advantage here is that the algorithm is guaranteed to terminate after a defined period but the difficulty is to choose the value N. We have chosen the number of iterations to be equivalent to 10% of the number of all candidate beam orientations under consideration.

4.8 Hardware and software Implementation Details

The RRT^* non-coplanar VMAT algorithm is implemented using existing helper functions in matRad [131]. matRad is a toolkit for radiotherapy computational research written in Matlab. matRad includes an ipopt [132] implementation of L-BFGS algorithm [133] used for solving the VMAT optimization.

The class for the tree and node representation are adapted from a Matlab implementation of a hierarchical tree data structure [148]. All calculations are performed using an Intel® Xeon® computer with a 16-core W-2145 3.7GHz processor and 256GB random access memory (RAM). The couch and gantry are set to the same constant speed of 6 $degs^{-1}$during treatment. A beamlet size of 7×7 mm^2 and an MLC leaf size of 40×40 cm is chosen for computation. This choice of the beamlet size helps to reduce the size of the dose influence matrix. A machine dose rate setting of $600MUmin^{-1}$ and a leaf speed of 3 cms^{-1} is used in our optimization.

4.8.1 Comparison Metrics

The metrics employed for comparison include dose volume histogram, mean dose, maximum dose and conformity number already defined in chapter 3. To make a comparison between trajectories we introduce two metrics, the bending energy and total bending energy.

Bending Energy

The bending energy (B_e) is a function of the curvature of a trajectory and is used to determine the smoothness of a trajectory [149]. It is defined as:

$$B_e = \frac{1}{n}\sum_{i=1}^{n} \mathbf{k}_i^2 \tag{4.4}$$

where $\mathbf{k}_i$ is the curvature of the trajectory at node i and n is the number of nodes along the trajectory. The curvature at any node is an angle defined using the inner product of the two vectors formed by the two neighbor nodes of each node such that:

$$\mathbf{k}_i = \frac{(\mathbf{n}_{i-1} - \mathbf{n}_i).(\mathbf{n}_{i+1} - \mathbf{n}_i)}{||\mathbf{n}_{i-1} - \mathbf{n}_i||\,||\mathbf{n}_{i+1} - \mathbf{n}_i||} \tag{4.5}$$

Trajectories that contain sharp curves will have a high value of B_e.

Total Bending Energy

The Total bending energy (TB_e) is a metric that quantifies both the smoothness and the length of a trajectory [149]. It is defined as:

$$TB_e = \sum_{i=1}^{n} \mathbf{k}_i^2 \tag{4.6}$$

Trajectories that contain sharp curves with many nodes will have a high value of TB_e.

4.9 Results

4.9.1 Comparison of RRT^* method vs greedy method

TG-119 Case

The DVH plot in figure 4.6 compares a treatment plan developed for a TG-119 case using RRT^* method (dashed lines) vs greedy method (thick lines). We observe that both methods deliver a similar dose distribution to the *Target* (50 Gy ± 0.5). We also observe a reduced dose to the *Core* and *Body* using the RRT^* method. Table 4.1 shows a comparison of the dose statistics for both methods. Using the RRT^* method 40% lower mean dose is observed in the *Core* 7.4 Gy vs 12.3 Gy and 19% less to the *Body* 3.9 Gy vs 4.8 Gy.

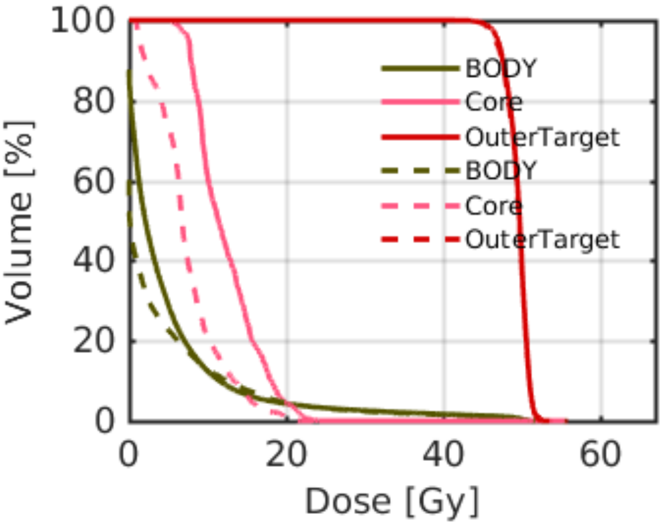

Figure 4.6 – DVH for TG-119 case comparing the RRT^* method (dashed lines) to greedy method (thick lines)

A slice of the CT showing the isodose contours for the TG-119 case planned using both methods can be observed in Figures 4.7. The CT slice shows a more conformal dose distribution around the *Target* with the greedy method. From table 4.1, we note that the greedy method terminates with a lower final objective function value of 17,200 vs 24370 for RRT^* method. Comparing the trajectories using figure 4.8 shows that the proposed RRT^* method has more control points on the trajectory (62) vs the greedy method (26). RRT^* method also has an estimated delivery time of 234s vs 140s for greedy method as can be observed in table 4.2. We can see a better trajectory smoothness with RRT^* method B_e (0.51 vs 0.89) and TB_e (32.16 vs 128).

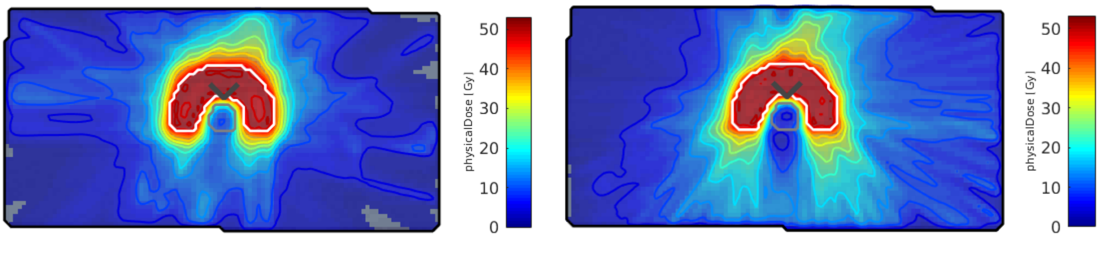

(a)

(b)

Figure 4.7 – Comparing Isodose contours for TG-119 using greedy method (a) and RRT^* method (b)

Table 4.1 – Dose statistics for TG-119 case

Metric	**greedy method**		**RRT* method**	
Objective function value	1.72×10^4		2.44×10^4	
Conformity Number	0.91		0.9	
Dose(Gy)	**Mean**	**Max**	**Mean**	**Max**
Target	49.5	52.8	49.5	53.2
Core	12.3	24.2	7.4	21.3
Body	4.8	52.8	3.9	53.2

Table 4.2 – Comparing trajectory characteristics generated for TG-119 case

Metric	**greedy method**	**RRT* method**
Estimated Delivery time	140s	234s
No of control points	26	62
B_e	0.89	0.51
TB_e	128	32.16

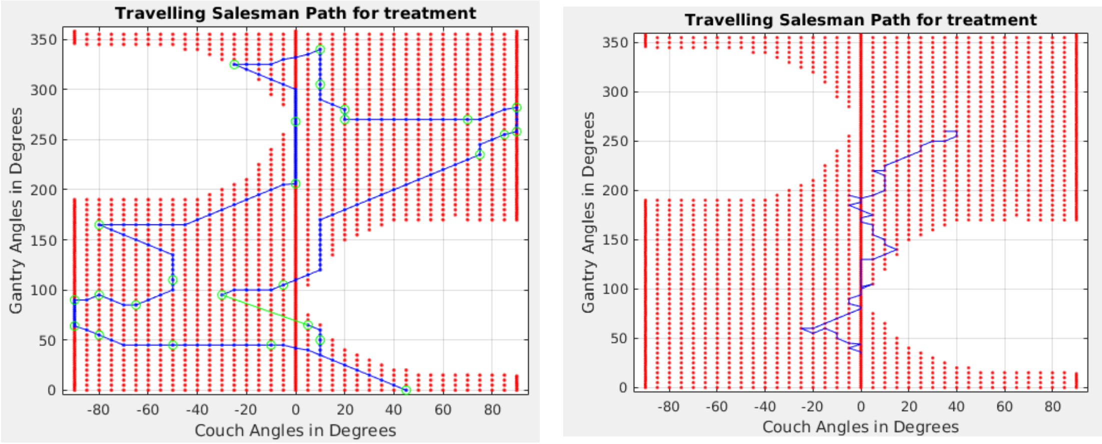

(a) (b)

Figure 4.8 – Comparing Trajectories for TG-119 using greedy method (a) and RRT^* method (b)

Liver Case

A DVH comparison between RRT^* method (dashed lines) and greedy method (thick lines) for the Liver case is shown in figure 4.9. The *Target* recieves a similar dose distribution when using both methods with a mean dose of (50 Gy ± 0.3). We observe from table 4.3 the reductions in the mean dose to the OARs using the RRT^* method vs greedy method. These reductions include: *SMASV* 1.05 Gy vs 1.6 Gy (35%), *Heart* 3.2 Gy vs 4.2 Gy (24%), *Duodenum* 0.6 Gy vs 1.0 Gy (40%) and *Celiac* 0.8 Gy vs 2.1 Gy (62%).

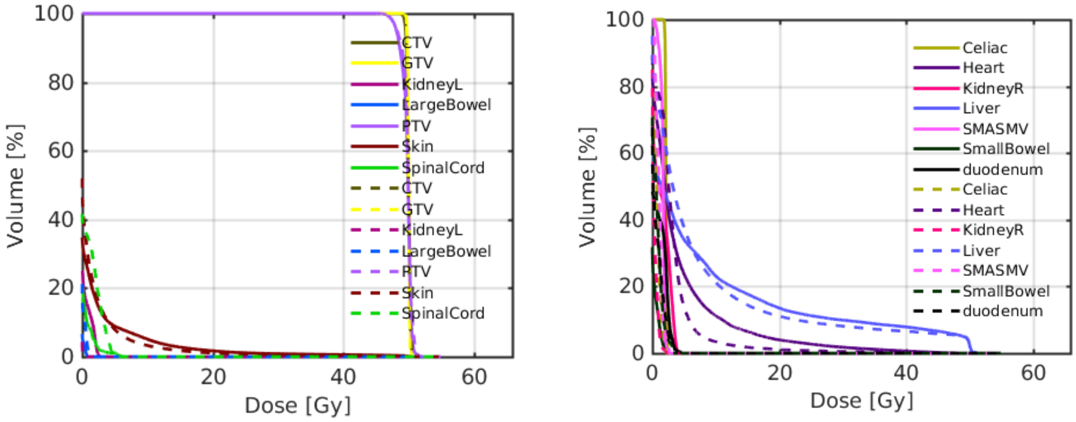

Figure 4.9 – DVH comparing the RRT^* method (dashed lines) to greedy method (thick lines) for Liver case

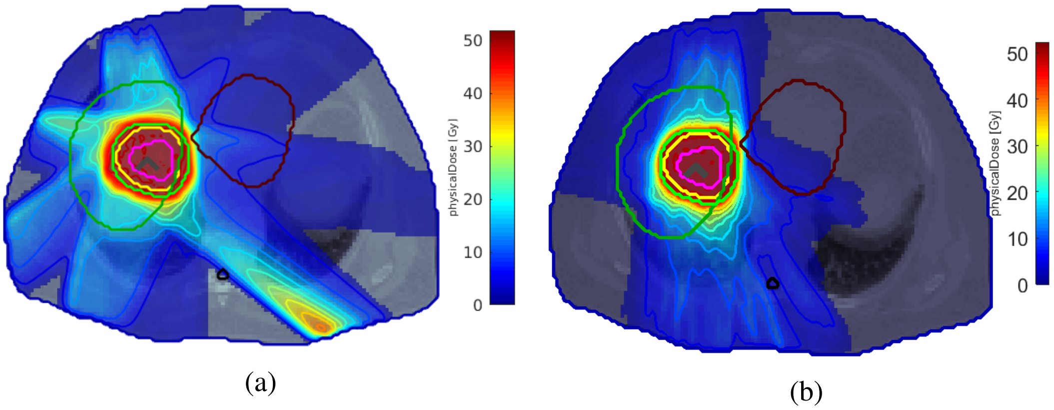

(a)

(b)

Figure 4.10 – Comparing Isodose contours for Liver using greedy method (a) and RRT^* method (b)

Table 4.3 – Dose statistics for Liver case

Metric	**greedy method**		**RRT* method**	
Objective function value	1.05×10^4		9.29×10^3	
Conformity Number	0.9		0.96	
Dose(Gy)	**Mean**	**Max**	**Mean**	**Max**
Target	49.7	51.9	49.9	51.3
Celiac	2.1	2.4	0.8	2.1
Heart	4.2	50	3.2	50.9
Duodenum	1.0	4.8	0.6	5.2
SMASV	1.6	2.4	1.05	2.6
Skin	1.7	51.9	1.5	52.3

Table 4.4 – Comparing trajectory generated for Liver case

Metric	**greedy method**	**RRT* method**
Estimated Delivery time	127s	168s
No of control points	43	52
B_e	0.92	0.5
TB_e	66.44	26.08

On the whole, treatment plans created with both methods have a similar dosimetry with the RRT^* method achieving slightly better dosimetry. The isodose contours in figure 4.10 and the conformity number in table 4.3 (0.96 vs 0.9) show the improved conformal dose distribution using the RRT^* method. The final objective function value of greedy method is a higher 10500 vs 9290 for the RRT^* method. Another difference in both treatment plans can be seen when we compare their trajectories in figure 4.8. The greedy method produces a treatment plan with fewer control points (43) while the RRT^* method has more control points (52). Comparing trajectory metrics in table 4.4 we see that the RRT^* method produces a smoother trajectory. This trajectory smoothness is verifieed by a lower value of B_e (0.5 vs 0.92) and TB_e (26.08 vs 66.44) for the RRT^* method.

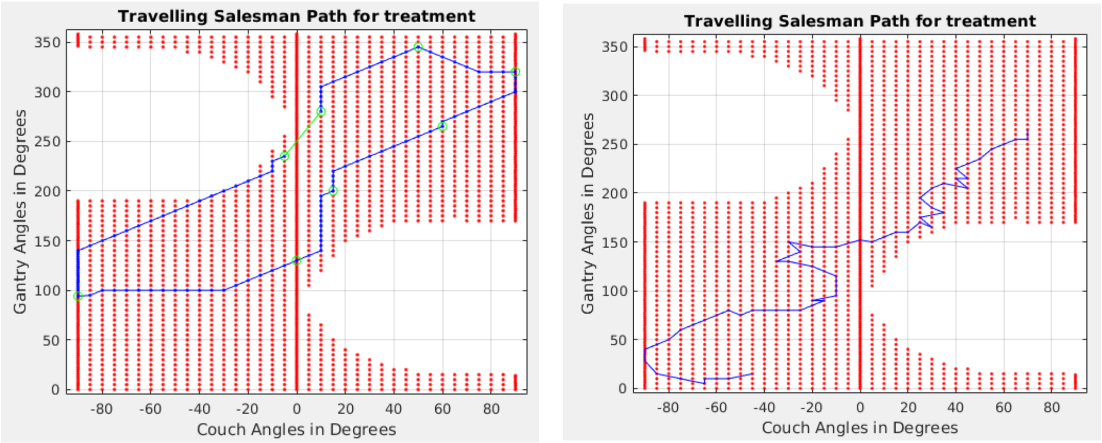

(a) (b)

Figure 4.11 – Comparing Trajectories for Liver using greedy method (a) and RRT^* method (b)

Prostate Case

Figure 4.13 makes a comparison of the DVH plot for the prostate case using using RRT^* method (dashed lines) vs greedy method (thick lines). The *Target* recieves the prescribed dose distribution (50 Gy ± 0.9) in both cases. We observe a reduced mean dose to the *Skin*,*Penile bulb* and *Rectum* using the RRT^* method. This reduction in the mean dose represents 6.7 Gy vs 6.9 Gy (3%) to the *Skin*, 1.2 Gy vs 6.2 Gy (91%) to the *Penile bulb* and 21.08 Gy vs 22.4 Gy (6%) to the *Rectum*. On the contrary the plan made using RRT^* method has an increased mean dose to the *Bladder* 24.08 Gy vs 23.5 Gy (3%) as seen in table 3.7. The table also shows that the greedy method has terminated with a lower objective function value of 72400 vs 85735 for the RRT^* method.

Table 4.5 – Dose statistics for Prostate case

Metric	**greedy method**		**RRT* method**	
Objective function value	7.24×10^4		8.57×10^4	
Conformity Number	0.5		0.48	
Dose(Gy)	**Mean**	**Max**	**Mean**	**Max**
Target	49.4	56.2	49.02	55
Skin	6.9	53.8	6.7	55
Bladder	23.5	53.5	24.08	52.58
Rectum	22.4	50.9	21.08	49.59
Penile bulb	6.2	14.5	1.2	4.7

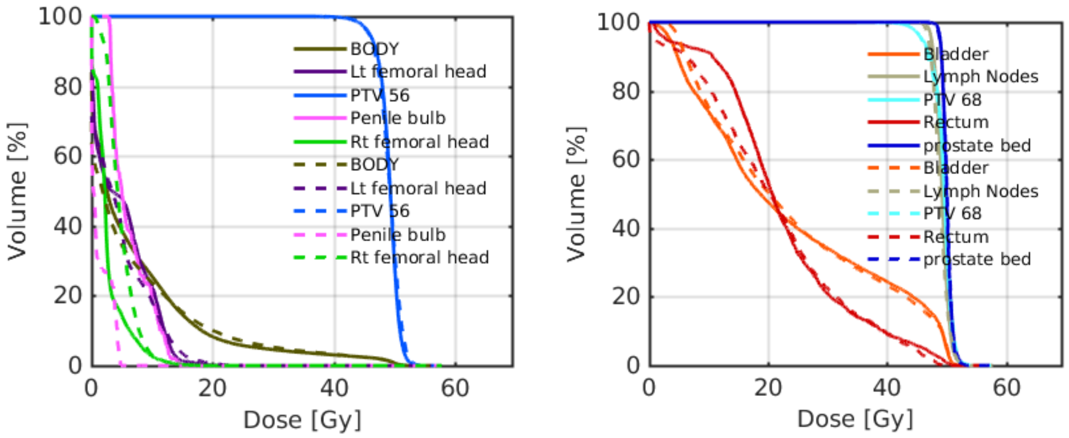

Figure 4.13 – DVH comparing the RRT^* method (dashed lines) to greedy method (thick lines)

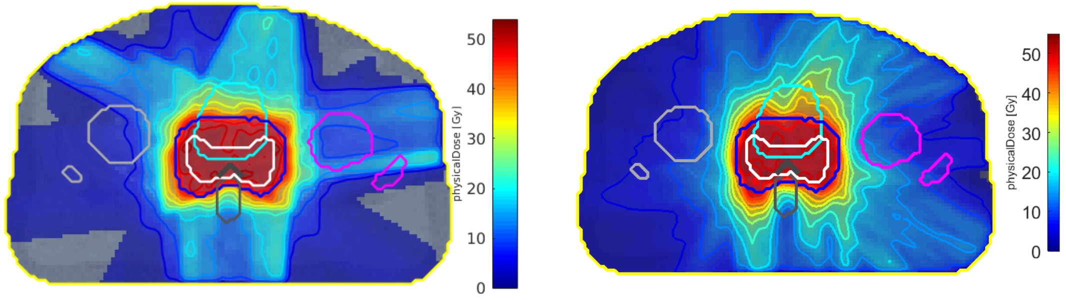

(a) (b)

Figure 4.14 – Comparing Isodose Contours for Prostate using greedy method (a) and RRT^* method (b)

The isodose contours in figure 4.14 shows that the RRT^* method produces a more conformal dose distribution. Comparing the trajectories produced by both methods in figure 4.15, we see that greedy method has 10 control points vs RRT^* method with 72 control points. The RRT^* method has better smoothness metrics of B_e (0.5 vs 0.89) and TB_e (36.37 vs 82.83) compared to the greedy method.

Table 4.6 – Comparing trajectory generated for Prostate case

Metric	greedy method	RRT* method
Estimated Delivery time	87s	153s
No of control points	10	72
B_e	0.89	0.5
TB_e	82.83	36.37

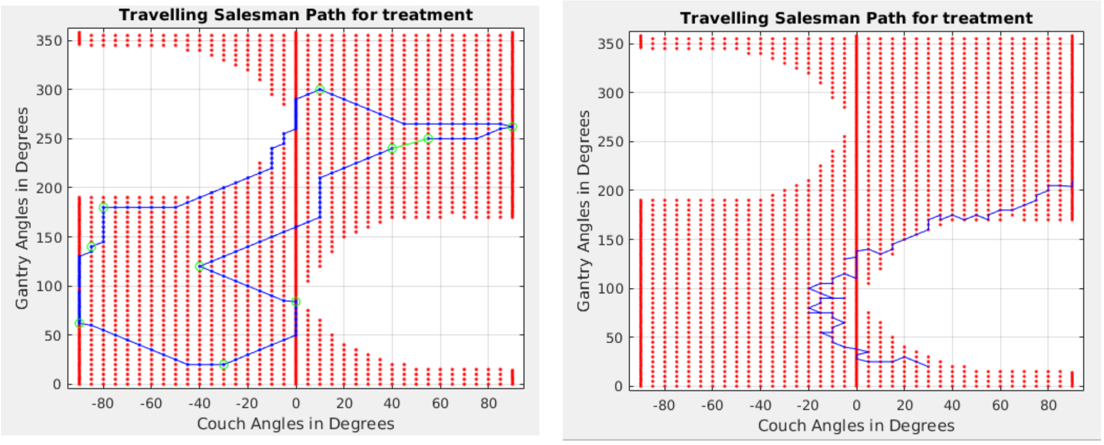

(a)

(b)

Figure 4.15 – Comparing Trajectories for Prostate using greedy method (a) and RRT^* method (b)

4.9.2 Comparison of RRT^* method vs simulated annealing method

TG-119 Case

The DVH plot in figure 4.16 compares a treatment plan developed for a TG-119 case using SA method (dashed lines) vs RRT^* method (thick lines). The dose distribution to the *Target* using both methods are very similar and in the range of (50 Gy ± 0.5). However a reduced mean dose to the *Core* and *Body* can be observed using the SA method. The dose statistics for both methods are compared in table 4.7. The table shows that the mean dose is reduced to the *Core* (4.7 Gy vs 7.4 Gy) and *Body* (3.7 Gy vs 3.9 Gy) using SA method vs RRT^* method. This represents a reduction of 36% in the mean dose to *Core* and 5% to the *Body*.

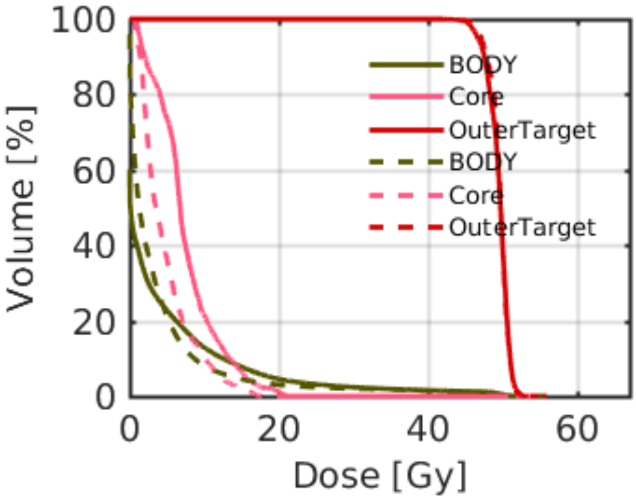

Figure 4.16 – DVH for TG-119 case comparing the simulated annealing method (dashed lines) to RRT^* method (thick lines)

A slice of the CT showing the dose contours for the TG-119 case planned using both methods can be observed in Figures 4.17. The CT slice shows a more conformal dose distribution with the SA method. From table 4.7, we note that the SA method terminates with a lower final objective function value of 16,400 vs 24370 for RRT^* method. The main difference between both methods can be seen when we compare the trajectories they produce. The trajectory comparison in figure 4.18 shows that the proposed RRT^* method has a shorter trajectory with 62 control points vs 92 control points for the SA method. This can be confirmed in table 4.8 with a delivery time of 234s for RRT^* method vs 227s for SA method. We can also observe that the proposed RRT^* method has a better trajectory smoothness as quantified by a lower value of B_e (0.51 vs 0.79) and TB_e (32.16 vs 201.48).

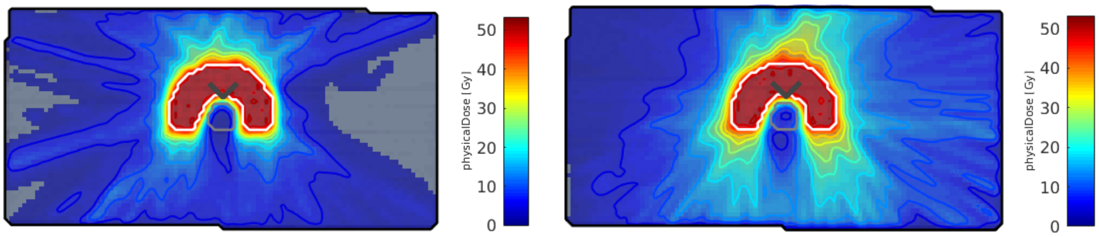

(a)

(b)

Figure 4.17 – Comparing Isodose contours for TG-119 using SA method (a) and RRT^* method (b)

Table 4.7 – Dose statistics for TG-119 case

Metric	**SA method**		RRT^* **method**	
Objective function value	1.64×10^4		2.44×10^4	
Conformity Number	0.92		0.9	
Dose(Gy)	**Mean**	**Max**	**Mean**	**Max**
Target	49.6	52.3	49.5	53.2
Core	4.7	17.6	7.4	21.3
Body	3.7	52.3	3.9	53.2

Table 4.8 – Comparing trajectory generated for TG-119 case

Metric	**SA method**	RRT^* **method**
Estimated Delivery time	227s	234s
No of control points	92	62
B_e	0.79	0.51
TB_e	201.48	32.16

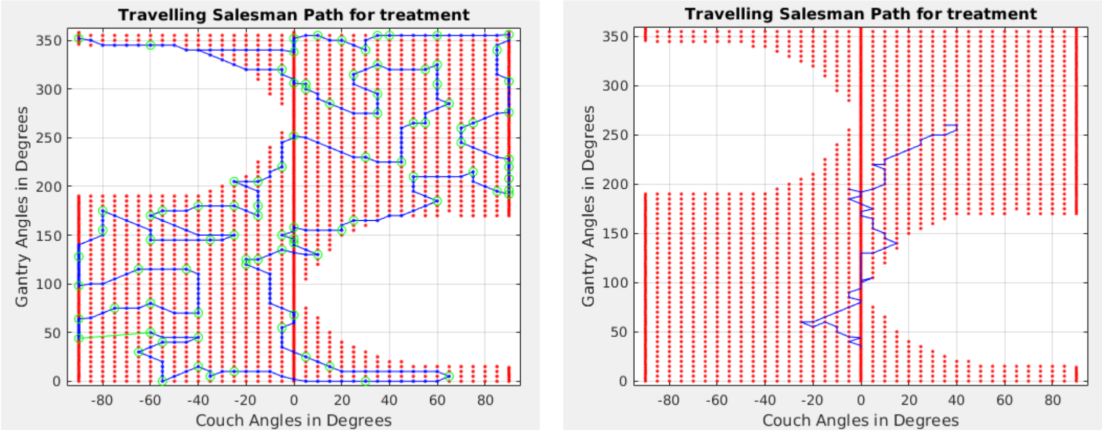

(a) (b)

Figure 4.18 – Comparing Trajectories for TG-119 using SA method (a) and RRT^* method (b)

4.9.3 Liver Case

The DVH shown in figure 4.19 compares the treatment plan calculated using SA method (dashed lines) vs RRT^* method (thick lines) for the Liver case. Both methods produce a similar dose distribution to the *Target* and *Skin* as observed in the DVH plot. The dose statistics in table 4.9 shows a reduction in the mean dose to the OARs when using SA method vs RRT^* method. These OARs include : *SMASV* 0.7 Gy vs 1.05 Gy (33%), *Heart* 2.6 Gy vs 3.2 Gy (18%), *Duodenum* 0.4 Gy vs 0.6 Gy (33%). Conversely an increase in the mean dose to the *Celiac* 1.1 Gy vs 0.8 Gy (27%) is observed using the SA method vs the RRT^* method.

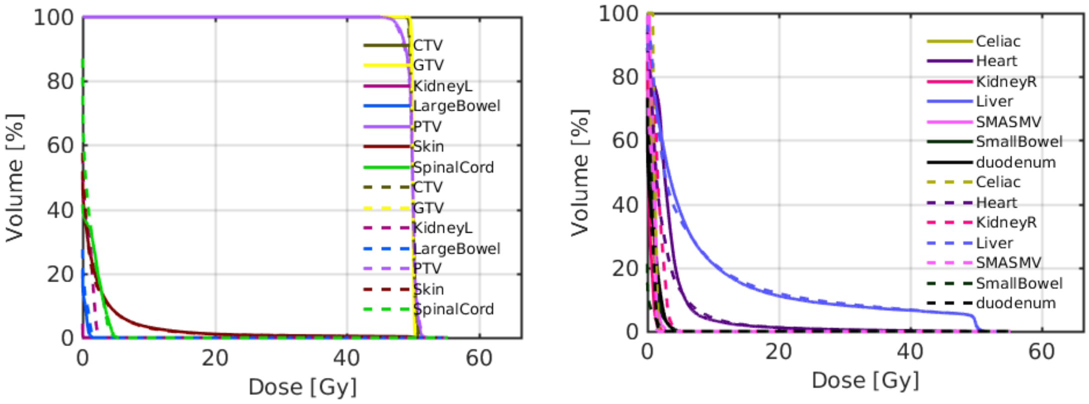

Figure 4.19 – DVH comparing the SA method (dashed lines) to RRT^* method (thick lines) for Liver case

The dose ditribution of both treatment plans can be observed from figure 4.20 showing the CT slices containing the Isodose contours. The conformity number is very similar for both methods (0.95 vs 0.96), can be observed in table 4.9. The final objective function value of SA method is a higher 9,500 vs 9290 for the RRT^* method. Comparing the trajectory of both treatment plans in figure 4.18, we can observe a longer trajectory when using the SA method ($Control\,points = 31$) while the RRT^* method has a shorter trajectory ($Control\,points = 52$). We also observe in table 4.10 that the RRT^* method produces a smoother trajectory. The trajectory smoothness is quantified by a lower value of B_e (0.5 vs 0.84) and TB_e (26.08 vs 115.65) for the RRT^* method as observed in table 4.10.

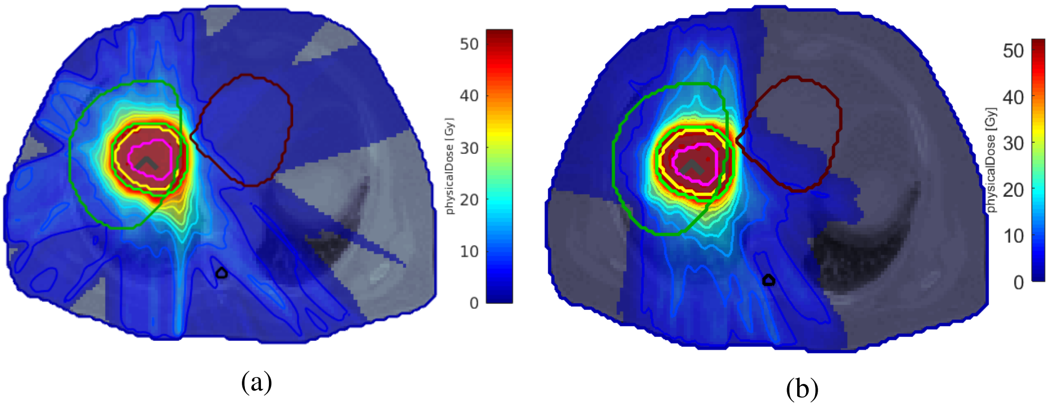

(a)

(b)

Figure 4.20 – Comparing Isodose contours for Liver using SA method (a) and RRT^* method (b)

Table 4.9 – Dose statistics for Liver case

Metric	SA method		RRT^* method	
Objective function value	9.5×10^3		9.29×10^3	
Conformity Number	0.95		0.96	
Dose(Gy)	**Mean**	**Max**	**Mean**	**Max**
Target	49.9	51.4	49.9	51.3
Celiac	1.1	1.6	0.8	2.1
Heart	2.6	51	3.2	50.9
Duodenum	0.4	1.8	0.6	5.2
SMASV	0.7	1.4	1.05	2.6
Skin	1.5	52.6	1.5	52.3

Table 4.10 – Comparing trajectory generated for Liver case

Metric	SA method	RRT^* method
Estimated Delivery time	132s	168s
No of control points	31	52
B_e	0.84	0.5
TB_e	115.65	26.08

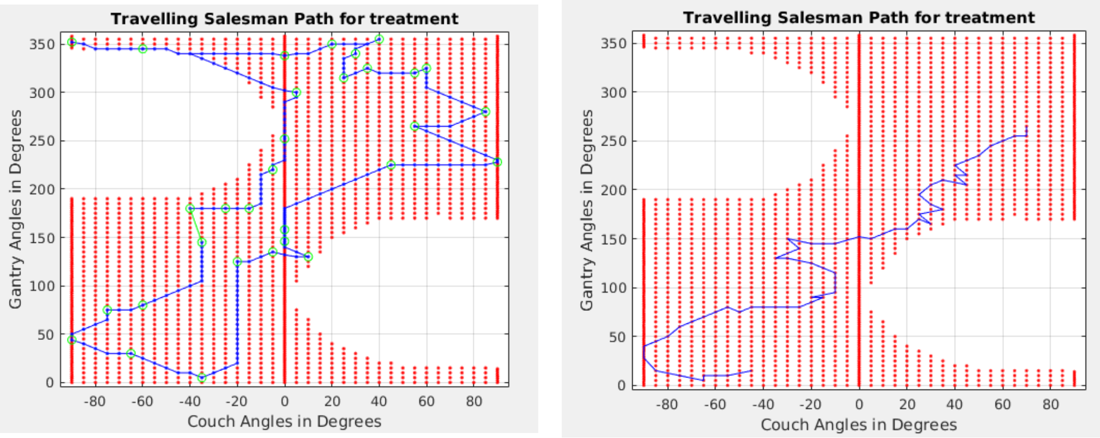

(a) (b)

Figure 4.21 – Comparing Trajectories for Liver using SA method (a) and RRT^* method (b)

4.9.4 Prostate Case

In figure 4.23, we see the DVH plot comparing a treatment plan for the prostate case using using SA method (dashed lines) vs RRT^* method (thick lines). We observe that both methods deliver the prescribed dose distribution to the *Target* with a mean dose of (50 Gy ± 1.2). However a reduction in the mean dose to the *Bladder* and to the *Rectum* can be observed in the DVH using SA method. This reduction is quantified from the dose statistics in table 4.11 with mean dose to the *Rectum* 19.5 Gy vs 28.5 Gy (32%), *Bladder* 22.5 Gy vs 26.6 Gy (15%). On the contrary the SA method shows an increased mean dose to the *Skin* 6.9 Gy vs 6.6 Gy (+4%). We also observed from the table that the SA method has terminated with a lower objective function value of 68800 vs 85735 for the RRT^* method.

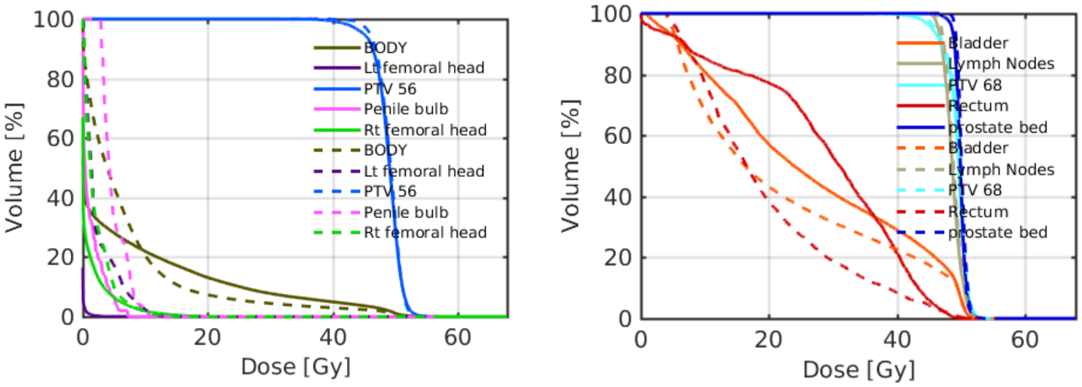

Figure 4.23 – DVH comparing the SA method (dashed lines) to RRT^* method (thick lines)

The isodose contours are presented in figure 4.24 shows that the SA method produces a more conformal dose distribution compared to RRT^* method. The SA method also has a higher conformity number 0.49 vs 0.39 as seen in table 4.11. The final objective function value of the SA method is lower at 68,800 vs 85,700 for the RRT^* method.From a comparison of the trajectories of both treatment plans in figure 4.25. The SA method has a trajectory with 43 control points compared to the RRT^* method with 72 control points. The RRT^* method has a delivery time of 153s as seen in table 4.12. Finally the RRT^* method has better smoothness metrics of B_e (0.5 vs 0.81) and TB_e (36.37 vs 134.12) compared to the SA method.

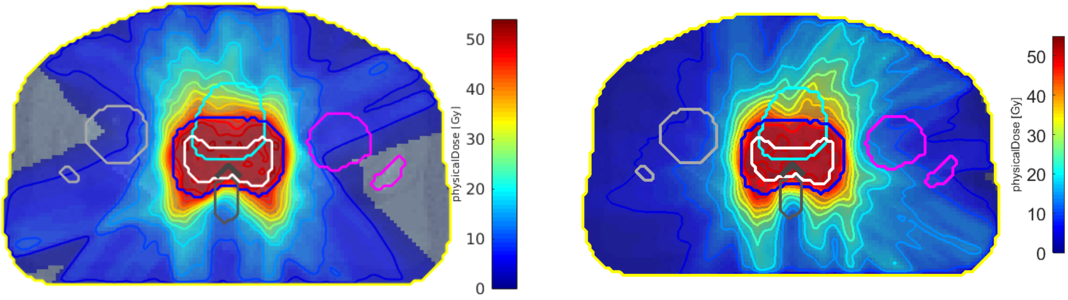

(a)

(b)

Figure 4.24 – Comparing Isodose Contours for Prostate using SA method (a) and RRT^* method (b)

Table 4.11 – Dose statistics for Prostate case

Metric	**SA method**		***RRT*** **method**	
Objective function value	6.88×10^4		8.57×10^4	
Conformity Number	0.49		0.31	
Dose(Gy)	**Mean**	**Max**	**Mean**	**Max**
Target	49	53.8	48.8	56.6
Skin	6.9	53.8	6.6	68
Bladder	22.5	53.7	26.6	52.9
Rectum	19.5	51.6	28.5	50
Penile bulb	4.9	10.6	1.2	7.2

Table 4.12 – Comparing trajectory generated for Prostate case

Metric	**SA method**	RRT^* **method**
Estimated Delivery time	127s	153s
No of control points	43	72
B_e	0.85	0.5
TB_e	134.12	36.37

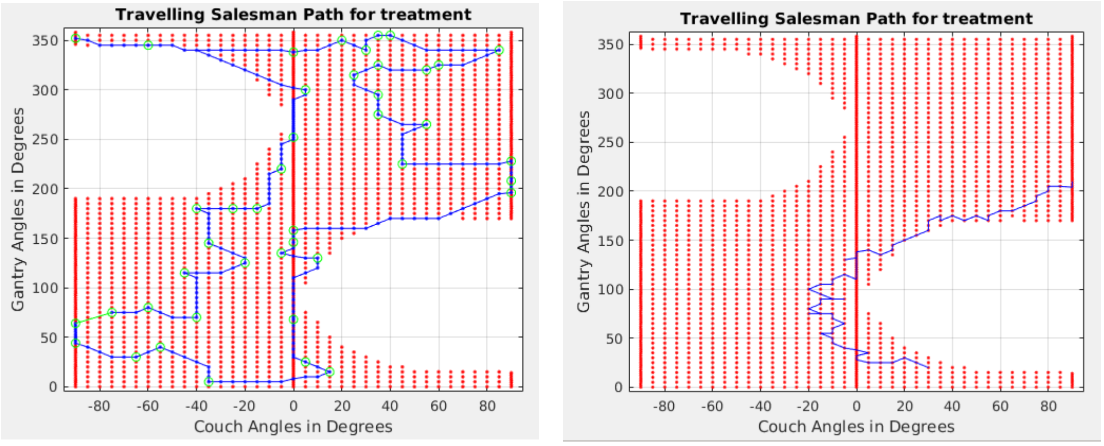

(a) (b)

Figure 4.25 – Comparing Trajectories for Prostate using SA method (a) and RRT^* method (b)

4.10 Discussion

We have presented an RRT^* method that simultaneously generates a non-coplanar trajectory while performing a VMAT optimization. The RRT^* method was inspired from the hypothesis that the quality of the final plan is dependent on the delivery trajectory employed. Therefore the trajectory generation is run concurrently as the VMAT plan optimization is performed.

The RRT^* method avoids the two-step approach found with beam angles selection methods for non-coplanar VMAT treatment planning such as the greedy method. The two-step approach of generating a non-coplanar trajetory and subsequently obtaining a VMAT plan along this trajectory can be seen in [93] and [77]. The advantage of avoiding this two-step approach is the elimination of the need to include intermediate nodes in order to form valid trajectories from the selected beam angles. Therefore no loss of plan quality occurs. All the nodes generated by the RRT^* algorithm are active during treatment delivery reducing the error between a treatment plan and it's delivery.

We have observed an improved dosimetry of the VMAT plan obtained using the RRT^* method compared to the greedy method. This is expected as the RRT^* method samples a larger portion of the global solution space to generate the non-coplanar VMAT treatment plan. A better OAR sparing was observed using the RRT^* method in most cases. The OAR sparing observed include: reduced mean dose to the core in TG-119 case (40%), the heart in Liver case (24%) and the rectum in Prostate case (6%). However, no significant differences are observed in the dose delivered to the target in all cases.

We observed that there is a (3%) increase in the mean dose to the bladder using the RRT^* method in the prostate case. In general, the RRT^* method has a comparatively superior dosimetry to our implementation of the state of the art greedy method. The smoothness of the trajectory was measured using the bending energy (B_e) and total bending energy (TB_e). A lower value of B_e and TB_e is observed when using the RRT^* method vs the greedy method in all patient cases.

When compared to the SA method, it is observed that the dosimetry of the VMAT plan obtained using the RRT^* method is not superior. This is expected as the SA method finds the global solution when generating the non-coplanar VMAT treatment plan. OAR sparing observed using the SA method include: reduced mean dose to the core in TG-119 case (36%), the heart in Liver case (18%) and the rectum in Prostate case (32%). The SA method has a better accuracy in dose delivered to the target in all cases. A (4%) increase in the mean dose to the skin was observed using the SA method compared to RRT^* method ($6.9Gy\ vs\ 6.6Gy$) in the prostate case. In general, the SA method has a comparatively superior dosimetry than the proposed RRT^* method.

The main improvement offered by the RRT^* method over SA method can be seen when we compare the trajectories obtained from both methods. We observe that the RRT^* method compared to the SA method for the three patient cases has a lower value of the smoothness metrics B_e and TB_e is also observed with the RRT^* method vs the SA method in all patient cases. From our observation, RRT^* also produces a trajectory with nodes that are more closely related to each other which results in improved trajectory smoothness. This observation is valid and comes from the fact that the generation of a new node using the RRT^* method is constrained to be in relation to the previouly generated nodes and the root node.

The RRT^* method is a sampling-based approach thus the space of the candidate beams is explored in a constrained manner compared to the SA method which is unconstrained. The tree structure of the RRT^* method constrains the discovery of new nodes to be related to the previously discovered nodes and the root node. The implication is that the choice of the root node influences the final trajectory as new nodes are included to the tree only after comparing them to previously discovered nodes. This constraint therefore makes the choice of the root node a very important task as it influences the final VMAT treatment plan trajectory and quality.

Our choice of the root node of the tree using a first order estimate of the steepest descent direction using a projected gradient of the objective function in equation 4.2 is not unique. Other methods such as geometric scoring or greedy strategy can be applied to choose the root node.

The RRT^* method offers a reasonable trade-off between treatment plan quality and plan deliverability. Very high quality VMAT plans may be undeliverable using the existing equipment. When a trade-off is made to obtain a deliverable trajectory, it is important to that the treatment plan quality remains as high as possible. By solving VMAT optimization concurrently with the trajectory generation, both criteria of quality and deliverability are continuosly monitored.

Conclusion and Future Work

Conclusion

Despite advances that have been made over the last decades on improved treatment techniques, cancer remains one of the major causes of mortality in europe and around the world. New techniques for radiotherapy notably the non-coplanar VMAT have been proposed and show very promising dosimetric results.

The non-coplanar VMAT technique helps to better focus the radiation beam on the tumor target while sparing the organs-at-risk during treatment especially in the presence of complex geometric arrangement of organs. VMAT makes use of a lower amount of monitor units for treatments thus reducing the secondary side-effects and increases patient survival. However the factors that hinder their adoption persist.

One problem is that a dynamic motion of the gantry and couch during treatment could lead to a collision and hamper patient safety. Another issue is that the introduction of non-coplanar orientations increases the space of possible solutions. Therefore, a globally optimal set of orientations have to be chosen for treatment. Also an increase in the number of orientations significantly increases the size of the matrices used to hold data during computation. There are also issues in creating a valid trajectory from a set of beam orientations that have been chosen to be employed for treatment.

The focus of this thesis is to propose improvements to some of these problems so as to aid the adoption of non-coplanar VMAT for cancer treatments Our propositions touch three aspects of non-coplanar VMAT planning namely collision detection, global optimization for beam selection and trajectory generation.

Collision Detection

In Chapter 2, a fast and efficient method for detecting collision-prone beam orientations was presented. This methodology is proposed to eliminate the possibility of a collision during the motion of the couch and gantry. In this way, collisons can be detected at the pre-planning stage and removed to create a set of collision-free candidate couch-gantry orientations for use in treatment planning stage.

The proposed method uses MATLAB and ADAMS in a co-simulation to detect contact forces occuring between parts of the 3D CAD model of the simulated LINAC. Experiments were made to compare the collision-prone orientations on the simulated LINAC to Varian Trubeam® installed at CHRU Brest. The aim of these tests is to check that collisions are detected on the simulated and the real LINAC at the same orientations. No differences were observed in the collisions detected on the simulated LINAC compared to the real equiment thus validating the proposed methodology. The collision-free workspace at three different couch positions are also compared.

It has been observed from our experiments that the collision-free workspace available for treatment can be increased or decreased by changing the couch positions. The proposed methodology is fast and easy to integrate into the treatment planning workflow and eliminates the need to peform cumbersome measurement on the equipment. Other radiotherapy treatment centers can easily use the proposed method of collision detection simply by using the 3D models of their installed radiotherapy equipment.

Beam selection using Simulated annealing

In Chapter 3, a simulated-annealing inspired algorithm is presented for selecting globally optimal beam orientations for non-coplanar VMAT planning. Beam angle selection is first performed using simulated annealing in order to obtain optimal beams that serve as control points for the treatment trajectory. The second step is to create a valid treatment trajectory by solving a traveling salesman problem to connect all the optimal control points obtained from beam selection. Finally a direct leaf trajectory optimization is performed to obtain the final plan using the new trajectory.

Simulated annealing is employed because of its ability to escape local solutions. Direct leaf trajectory optimization allows us to include the machine parameter constraints during the beam selection phase. Treatment plans for three patient cases: a AAPM TG-119 case, a liver case and a prostate case are computed using our proposed non-coplanar simulated annealing VMAT algorithm and compared to our implementation of two state of the art approaches. One approach uses a coplanar trajectory and optimizes a VMAT treatmentr plan along this trajectory. Another approach uses a greedy strategy to select non-coplanar beam orientations and makes a final VMAT treatment plan along this trajectory. Our comparisons were made on the basis of prescription dose accuracy, organ-at-risk sparing and delivery time.

The results show an accurate delivery of the prescription dose to the target tumor volume ($50Gy \pm 0.6$) in all cases. The results also show an improved organ-at-risk sparing in terms of a reduced mean dose to the core in TG-119 case (38%), the heart in liver case (38%) and the rectum in prostate case (14%). The estimated delivery time when using the proposed simulated annealing algorithm was higher in all cases compared to the greedy method. An increase in the number of control points has been observed when using the proposed simulated annealing algorithm compared to the state of the art methods.

Our conclusion from this study is that the simulated annealing algorithm offers a dosimetric improvement in terms of organs-at-risk sparing compared to the state-of-the-art approaches.

Trajectory generation using RRT^*

In Chapter 4, an algorithm based on RRT^* for generating the trajectory for the non-coplanar VMAT plan delivery is presented. This algorithm eliminates the need to insert intermediate control points when beam selection methods are applied to non-coplanar VMAT treatment planning.

The algorithm samples the input candidate beam orientations to build a tree consisting of nodes and edges. A direct leaf trajectory optimizaton is solved simultaneously during tree construction to search for delivery trajectories with optimal dosimetry. A depth-first search is done after the tree construction to create a set of all valid trajectories that exist on the tree. A criteria of lowest objective function value is used to select the treatment trajectory.

Treatment plans for three patient case: liver case, prostate case and AAPM TG-119 case were prepared and the results compared to a state-of-the-art approach which we refer to as greedy method. The comparisons are made on the basis of dosimetric quality and trajectory smoothness. The results show an improved dosimetric quality and improved trajectory smoothness when compared to greedy method. The reductions to the mean dose to the organs-at-risk observed include: reduced mean dose to the Core in TG-119 case (40%), the Heart in Liver case (24%) and the Rectum in Prostate case (6%). The RRT^* method generates a trajectory with a lower number of control points and a lower delivery time than the greedy method for the three patient cases. The smoothness of the trajectory was measured using the bending energy (B_e) and total bending energy (TB_e) are lower value for the RRT^* method indicating better trajectory smoothness.

In order to test the performance of the proposed RRT^* algorithm for non-coplanar VMAT we also compare the resulting treatment plan to the treatment plans obtained using the simulated annealing algorithm proposed in chapter 3. The comparison showed that the simulated annealing algorithm has a better dosimetry with respect to reductions in mean dose to the organs-at-risk. OAR sparing observed using the simulated annealing method include: reduced mean dose to the Core in TG-119 case (36%), the Heart in Liver case (18%) and the Rectum in Prostate case (32%). However, the RRT^* algorithm produced a smoother trajectory than the simulated annealing method when measured with the bending energy metric that has been introduced.

Our conclusion from this study is that the RRT^* method offers a reasonable trade-off between treatment plan quality and plan deliverability because the dosimetry of the treatment plan is continuously monitored during trajectory generation.

Future work

Future work will be to include the patient model in the collision detection framework presented in chapter 2. This will involve a capture of the patient 3D pose using a point cloud and converting this to a parasolid using image reconstruction techniques.

A significant challenge encountered during this work is the very large size of the dose influence matrix data. We were able to overcome this problem by using a computer with a very large random access memory (256Gb). It is important in the future to investigate the possibility of compressing much of this data using other techniques of data representation in order to enable the use of these algorithms on computers that do not have a large random access memory. The dose influence matrix used in this wrok is already stored using a sparse representation. The improvement could be in the representation of the columns of this matrix as singular nodes of a computation which are distributed in parallel by a master node and then results returned at the end of the computation.

Another interesting area for future work is to perform further analysis of the simulated annealing algorithm in chapter 3 on different patient cases. Only three patient cases were considered in this thesis due to computational resource limitations and lack of patient data. It will be interesting to see how the algorithm performs on other specialized patient cases like breast or on patient cases that involve a massive amount of dose influence matrix data such as head and neck case.

Finally, RRT^* algorithm in chapter 4 needs to further investigated for application to trajectory planning for other radiotherapy treatment techniques such as brachytherapy. An example will involve the use of the RRT^* method to plan needle insertion trajectories for robots used in brachytherapy.

Dissemination

Peer-reviewed Publications

Okoli, F.O., Bert, J., Abdelhaziz, S., Buisson, N. and Visvikis, D., 2019. Beam Selection for Non-Coplanar Volumetric Modulated Arc Therapy using Simulated Annealing, Acta Oncologica (submitted).

Invited Presentations

Oral presentation: "Rapidly-exploring random trees for creating Non-Coplanar VMAT Treatment planning". **Okoli, F.O.**, Bert, J., Abdelhaziz, S. and Visvikis, D. French National Conference CAMI LabEx Days, Grenoble France December 2020. (accepted)

Oral presentation: "Optimizing Beam Selection for Non-Coplanar VMAT Treatment Planning with Simulated Annealing". **Okoli, F.O.**, Bert, J., Abdelhaziz, S. and Visvikis, D. International Conference on the use of Computers in Radiation Therapy, Montreal Canada June 2019. (accepted)

Oral presentation: "Optimization of treatment planning for non-coplanar external radiotherapy". **Okoli, F.O.**, Bert, J., Abdelhaziz, S. and Visvikis, D. French National Conference CAMI LabEx Days, Brest France December 2018. (accepted)

Funding

This work is supported by the French Agence nationale de la recherche (ANR) under the Investissements d'Avenir Program CAMI Labex (Ref:ANR-11-LABX-0004) and the Brittany Region in France.

BIBLIOGRAPHY

[1] Faiz M. Khan. *The Physics of Radiation Therapy*. Lippincott Williams & Wilkins, 2003. Google-Books-ID: hmb-byF9ZHo8C. 5, 14, 15

[2] E. B. Podgorsak. *Radiation Oncology Physics: A Handbook for Teachers and Students*. 2008. 5, 15

[3] Roy. Multileaf collimators: Modern beam shaping. 5, 16

[4] S. Webb. *The Physics of Three Dimensional Radiation Therapy: Conformal Radiotherapy, Radiosurgery and Treatment Planning*. CRC Press, January 1993. Google-Books-ID: 2kKStkqe4UUC. 5, 18

[5] Anders Brahme. Optimization of stationary and moving beam radiation therapy techniques. *Radiotherapy and Oncology*, 12(2):129–140, 1988. 5, 19, 20

[6] D. Olender, W. Kilby, and R. A. Schulz. Robotic whole body stereotactic radiosurgery: Clinical advantages of the CyberKnifeH integrated system. *Medical Robotics and Computer Assisted Surgery*, 1:28–39, 2005. 5, 20, 31

[7] What Is Cancer? `https://www.cancer.gov/about-cancer/understanding/what-is-cancer`. 12

[8] Cancer - Wikipedia, the free encyclopedia. `https://en.wikipedia.org/wiki/Cancer`. 12

[9] Cancer Research UK. Worldwide cancer incidence statistics | cancer research uk, 2019. 12

[10] J. Ferlay, E. Steliarova-Foucher, J. Lortet-Tieulent, Sonia Rosso, J. W. W. Coebergh, H. Comber, David Forman, and Freddie Bray. Cancer incidence and mortality patterns in Europe: Estimates for 40 countries in 2012. *European journal of cancer*, 49(6):1374–1403, 2013. 12

[11] CancerToday. Cancer today. 12

[12] Why is early diagnosis important? `http://www.cancerresearchuk.org/about-cancer/cancer-symptoms/why-is-early-diagnosis-important`, 2015-04-02T16:50:26+01:00. 12

[13] What is Cancer Surgery? `http://www.cancer.net/navigating-cancer-care/how-cancer-treated/surgery/what-cancer-surgery`, 2011-03-31T00:03:00-04:00. 12

[14] Questions and Answers About Chemotherapy. `http://www.webmd.com/cancer/questions-answers-chemotherapy`. 12

[15] Cancer Research UK. What hormone therapy is. `http://www.cancerresearchuk.org/about-cancer/cancers-in-general/treatment/hormone/what-hormone-therapy-is`, January 2015. 12

[16] Targeted Therapy. `https://www.cancer.gov/about-cancer/treatment/types/targeted-therapies`. 12

[17] Cancer.Net. Breast cancer: Types of treatment. 12

[18] Radioactive decay - Wikipedia. `https://en.wikipedia.org/wiki/Radioactive_decay`. 13

[19] P. Mayles, A. Nahum, and J. C. Rosenwald. *Handbook of Radiotherapy Physics: Theory and Practice*. CRC Press, June 2007. Google-Books-ID: v68J1dgCEn8C. 13, 14, 15

[20] How does radiation work to treat cancer? | American Cancer Society. `http://www.cancer.org/treatment/treatmentsandsideeffects/treatmenttypes/radiation/radiationtherapyprinciples/radiation-therapy-principles-how-does-radiation-work`. 13

[21] Le Caër and Sophie. Water Radiolysis: Influence of Oxide Surfaces on H2 Production under Ionizing Radiation. *Water*, 3(1):235–253, February 2011. 13

[22] Edward C. Halperin, Carlos A. Perez, and Luther W. Brady. *Perez and Brady's Principles and Practice of Radiation Oncology*. Lippincott Williams & Wilkins, 2008. 13

[23] Radiological Society of North America (RSNA) (ACR) and American College of Radiology. Brachytherapy (Internal radiation therapy). `http://www.radiologyinfo.org/en/info.cfm?pg=brachy`. 14

[24] Ulrik Ringborg, David Bergqvist, Bengt Brorsson, Eva Cavallin-Ståhl, Jeanette Ceberg, Nina Einhorn, Jan-erik Frödin, Johannes Järhult, Gunilla Lamnevik, Christer Lindholm, et al. The swedish council on technology assessment in health care (sbu) systematic overview of radiotherapy for cancer including a prospective survey of radiotherapy practice in sweden 2001–summary and conclusions. *Acta Oncologica*, 42(5-6):357–365, 2003. 14

[25] Geoff Delaney, Susannah Jacob, Carolyn Featherstone, and Michael Barton. The role of radiotherapy in cancer treatment: estimating optimal utilization from a review of evidence-based clinical guidelines. *Cancer: Interdisciplinary International Journal of the American Cancer Society*, 104(6):1129–1137, 2005. 14

[26] Peter J. Biggs. Radiation Generators. In *Physics Review Course 52 Nd Annual Meeting, AAPM Philadelphia, PA July*, volume 17, 2010. 15

[27] Morton A Meyers. 3d ct imaging in clinical practice. *Abdominal imaging*, 34(1):1–2, 2009. 17

[28] Brigitte Gundlich, Patrick Musmann, Simone Weber, Oliver Nix, and Wolfhard Semmler. From 2d pet to 3d pet: issues of data representation and image reconstruction. *Zeitschrift fuer Medizinische Physik*, 16(1):31–46, 2006. 17

[29] Nickolas Papanikolaou and Spyros Karampekios. 3d mri acquisition: Technique. In *Image Processing in Radiology*, pages 15–26. Springer, 2008. 17

[30] Lei Xing, Yong Yang, and Daniel M Spielman. Molecular/functional image-guided intensity modulated radiation therapy. In *Image-Guided IMRT*, pages 187–198. Springer, 2006. 19

[31] Zhang Guowei, Jiang Ziping, David Shepard, Matt Earl, and Cedric Yu. Effect of beamlet step-size on imrt plan quality. *Medical Physics*, 32(11), 2005. 19

[32] Anders Brahme. Guest editorial: Optimization of the three-dinensional dose delivery and tomotherapy. *International Journal of Imaging Systems and Technology*, 6(1):1–1, 1995. 20

[33] R Alfredo C Siochi. Minimizing static intensity modulation delivery time using an intensity solid paradigm. *International Journal of Radiation Oncology* Biology* Physics*, 43(3):671–680, 1999. 20, 26

[34] Bin S. Teh, Shiao Y. Woo, and E. Brian Butler. Intensity modulated radiation therapy (IMRT): A new promising technology in radiation oncology. *The oncologist*, 4(6):433–442, 1999. 20

[35] Thomas Bortfeld, Arthur L. Boyer, Wolfgang Schlegel, Darren L. Kahler, and Timothy J. Waldron. Realization and verification of three-dimensional conformal radiotherapy with modulated fields. *International Journal of Radiation Oncology* Biology* Physics*, 30(4):899–908, 1994. 20

[36] Roger Svensson, P. Kallman, and Anders Brahme. An analytical solution for the dynamic control of multileaf collimators. *Physics in Medicine and Biology*, 39(1):37, 1994. 20

[37] James M. Galvin, Xuan-Gen Chen, and Robert M. Smith. Combining multileaf fields to modulate fluence distributions. *International Journal of Radiation Oncology* Biology* Physics*, 27(3):697–705, 1993. 20

[38] David M. Shepard, Michael C. Ferris, Gustavo H. Olivera, and T. Rockwell Mackie. Optimizing the delivery of radiation therapy to cancer patients. *Siam Review*, 41(4):721–744, 1999. 20

[39] Cedric X. Yu. Intensity-modulated arc therapy with dynamic multileaf collimation: An alternative to tomotherapy. *Physics in medicine and biology*, 40(9):1435, 1995. 20

[40] X Yu Cedric and Grace Tang. Intensity-modulated arc therapy: principles, technologies and clinical implementation. *Physics in Medicine & Biology*, 56(5):R31, 2011. 20

[41] Jan Unkelbach, Thomas Bortfeld, David Craft, Markus Alber, Mark Bangert, Rasmus Bokrantz, Danny Chen, Ruijiang Li, Lei Xing, Chunhua Men, and others. Optimization approaches to volumetric modulated arc therapy planning. *Medical physics*, 42(3):1367–1377, 2015. 20

[42] M. Teoh, C. H. Clark, K. Wood, S. Whitaker, and A. Nisbet. Volumetric modulated arc therapy: A review of current literature and clinical use in practice. *The British journal of radiology*, 2014. 20, 82

[43] Thomas Bortfeld. IMRT: A review and preview. *Physics in medicine and biology*, 51(13):R363, 2006. 20

[44] Xuejun Gu, Dongju Choi, Chunhua Men, Hubert Pan, Amitava Majumdar, and Steve B. Jiang. GPU-based ultra-fast dose calculation using a finite size pencil beam model. *Physics in medicine and biology*, 54(20):6287, 2009. 21

[45] Julien Bert, Hector Perez-Ponce, Ziad El Bitar, Sébastien Jan, Yannick Boursier, Damien Vintache, Alain Bonissent, Christian Morel, David Brasse, and Dimitris Visvikis. Geant4-based Monte Carlo simulations on GPU for medical applications. *Physics in medicine and biology*, 58(16):5593, 2013. 21

[46] Yair Censor. Mathematical optimization for the inverse problem of intensity-modulated radiation therapy. *Intensity-modulated radiation therapy: the state of the art, American Association of Physicists in Medicine, Medical physics monograph*, (29):25–49, 2003. 21

[47] Larry Armijo. Minimization of functions having lipschitz continuous first partial derivatives. *Pacific Journal of mathematics*, 16(1):1–3, 1966. 22

[48] Jorge Nocedal and Stephen Wright. *Numerical optimization*. Springer Science & Business Media, 2006. 23

[49] Jorge Nocedal and Stephen Wright. *Numerical Optimization*. Springer Science & Business Media, 2006. 23

[50] Dong C Liu and Jorge Nocedal. On the limited memory bfgs method for large scale optimization. *Mathematical programming*, 45(1-3):503–528, 1989. 23

[51] Thomas Bortfeld and Wolfgang Schlegel. Optimization of beam orientations in radiation therapy: some theoretical considerations. *Physics in Medicine & Biology*, 38(2):291, 1993. 25

[52] Mark Bangert. New concepts for beam angle selection in IMRT treatment planning: From heuristics to combinatorial optimization. 2011. 25

[53] Jörg Stein, Radhe Mohan, Xiao-Hong Wang, Thomas Bortfeld, Qiuwen Wu, Konrad Preiser, C Clifton Ling, and Wolfgang Schlegel. Number and orientations of beams in intensity-modulated radiation treatments. *Medical Physics*, 24(2):149–160, 1997. 25

[54] Carl Graham Rowbottom, Vincent S Khoo, and Steve Webb. Simultaneous optimization of beam orientations and beam weights in conformal radiotherapy. *Medical Physics*, 28(8):1696–1702, 2001. 25

[55] Andrei Pugachev, Jonathan G Li, Arthur L Boyer, Steven L Hancock, Quynh-Thu Le, Sarah S Donaldson, and Lei Xing. Role of beam orientation optimization in intensity-modulated radiation therapy. *International Journal of Radiation Oncology* Biology* Physics*, 50(2):551–560, 2001. 25

[56] Yongjie Li, Jonathan Yao, and Dezhong Yao. Automatic beam angle selection in imrt planning using genetic algorithm. *Physics in Medicine & Biology*, 49(10):1915, 2004. 25

[57] Yongjie Li, Dezhong Yao, Jonathan Yao, and Wufan Chen. A particle swarm optimization algorithm for beam angle selection in intensity-modulated radiotherapy planning. *Physics in Medicine & Biology*, 50(15):3491, 2005. 25

[58] Chuang Wang, Jianrong Dai, and Yimin Hu. Optimization of beam orientations and beam weights for conformal radiotherapy using mixed integer programming. *Physics in Medicine & Biology*, 48(24):4065, 2003. 25

[59] Ruijie Yang, Jianrong Dai, Yong Yang, and Yimin Hu. Beam orientation optimization for intensity-modulated radiation therapy using mixed integer programming. *Physics in Medicine & Biology*, 51(15):3653, 2006. 25

[60] Shiva Das, Timothy Cullip, Gregg Tracton, Sha Chang, Lawrence Marks, Mitchell Anscher, and Julian Rosenman. Beam orientation selection for intensity-modulated radiation therapy based on target equivalent uniform dose maximization. *International Journal of Radiation Oncology* Biology* Physics*, 55(1):215–224, 2003. 25

[61] Konrad Engel and Eckhard Tabbert. Fast simultaneous angle, wedge, and beam intensity optimization in inverse radiotherapy planning. *Optimization and Engineering*, 6(4):393–419, 2005. 25

[62] Evert Woudstra and PRM Storchi. Constrained treatment planning using sequential beam selection. *Physics in Medicine & Biology*, 45(8):2133, 2000. 25

[63] G Meedt, M Alber, and F Nüsslin. Non-coplanar beam direction optimization for intensity-modulated radiotherapy. *Physics in Medicine & Biology*, 48(18):2999, 2003. 25

[64] OCL Haas, KJ Burnham, and JA Mills. Optimization of beam orientation in radiotherapy using planar geometry. *Physics in Medicine & Biology*, 43(8):2179, 1998. 25

[65] Carl Graham Rowbottom, Steve Webb, and Mark Oldham. Beam-orientation customization using an artificial neural network. *Physics in Medicine & Biology*, 44(9):2251, 1999. 25

[66] George TY Chen, Danny R Spelbring, Charles A Pelizzari, James M Balter, Leon C Myrianthopoulos, S Vijayakumar, and Howard Halpern. The use of beam's eye view volumetrics in the selection of non-coplanar radiation portals. *International Journal of Radiation Oncology* Biology* Physics*, 23(1):153–163, 1992. 25

[67] R Vaitheeswaran, VK Sathiya Narayanan, Janhavi R Bhangle, Amit Nirhali, Namitha Kumar, Sumit Basu, and Vikram Maiya. An algorithm for fast beam angle selection in intensity modulated radiotherapy. *Medical physics*, 37(12):6443–6452, 2010. 25

[68] Andrei Pugachev and Lei Xing. Computer-assisted selection of coplanar beam orientations in intensity-modulated radiation therapy. *Physics in Medicine & Biology*, 46(9):2467, 2001. 25

[69] Gino J Lim, Allen Holder, and Josh Reese. A clustering approach for optimizing beam angles in imrt planning. 2009. 25

[70] Daniel O'Connor, Yevgen Voronenko, Dan Nguyen, Wotao Yin, and Ke Sheng. Fast non-coplanar beam orientation optimization based on group sparsity. *arXiv preprint arXiv:1710.05308*, 2017. 25

[71] Karl Otto. Volumetric modulated arc therapy: IMRT in a single gantry arc. *Medical physics*, 35(1):310–317, 2008. 26, 27

[72] Jan Unkelbach, Thomas Bortfeld, David Craft, Markus Alber, Mark Bangert, Rasmus Bokrantz, Danny Chen, Ruijiang Li, Lei Xing, Chunhua Men, et al. Optimization approaches to volumetric modulated arc therapy planning. *Medical physics*, 42(3):1367–1377, 2015. 26, 27, 53, 91

[73] D. M. Shepard, M. A. Earl, X. A. Li, S. Naqvi, and C. Yu. Direct aperture optimization: A turnkey solution for step-and-shoot IMRT. *Medical physics*, 29(6):1007–1018, 2002. 26

[74] Chunhua Men, H. Edwin Romeijn, Xun Jia, and Steve B. Jiang. Ultrafast treatment plan optimization for volumetric modulated arc therapy (VMAT). *Medical physics*, 37(11):5787–5791, 2010. 27

[75] Fei Peng, Xun Jia, Xuejun Gu, Marina A Epelman, H Edwin Romeijn, and Steve B Jiang. A new column-generation-based algorithm for vmat treatment plan optimization. *Physics in Medicine & Biology*, 57(14):4569, 2012. 27

[76] Karl Bzdusek, Henrik Friberger, Kjell Eriksson, Björn Hårdemark, David Robinson, and Michael Kaus. Development and evaluation of an efficient approach to volumetric arc therapy planning. *Medical physics*, 36(6Part1):2328–2339, 2009. 27

[77] Esther Wild, Mark Bangert, Simeon Nill, and Uwe Oelfke. Noncoplanar VMAT for nasopharyngeal tumors: Plan quality versus treatment time. *Medical physics*, 42(5):2157–2168, 2015. 27, 28, 31, 32, 33, 35, 52, 53, 79, 82, 108

[78] James L Bedford. Treatment planning for volumetric modulated arc therapy. *Medical physics*, 36(11):5128–5138, 2009. 27

[79] Silke Ulrich, Simeon Nill, and Uwe Oelfke. Development of an optimization concept for arc-modulated cone beam therapy. *Physics in Medicine & Biology*, 52(14):4099, 2007. 27

[80] Dávid Papp and Jan Unkelbach. Direct leaf trajectory optimization for volumetric modulated arc therapy planning with sliding window delivery. *Medical physics*, 41(1):011701, 2014. 27, 53, 57, 58, 91

[81] H. Edwin Romeijn, Ravindra K. Ahuja, James F. Dempsey, and Arvind Kumar. A column generation approach to radiation therapy treatment planning using aperture modulation. *SIAM Journal on Optimization*, 15(3):838–862, 2005. 28

[82] Gregory Smyth, Philip M Evans, Jeffrey C Bamber, and James L Bedford. Recent developments in non-coplanar radiotherapy. *The British journal of radiology*, 92(xxxx):20180908, 2019. 30, 33

[83] Gregory Smyth, Philip M Evans, Jeffrey C Bamber, Henry C Mandeville, Liam C Welsh, Frank H Saran, and James L Bedford. Non-coplanar trajectories to improve organ at risk sparing in volumetric modulated arc therapy for primary brain tumors. *Radiotherapy and Oncology*, 121(1):124–131, 2016. 31, 52

[84] Ke Sheng, David M Shepard, and Colin G Orton. Noncoplanar beams improve dosimetry quality for extracranial intensity modulated radiotherapy and should be used more extensively. *Medical physics*, 42(2):531–533, 2015. 31, 35, 52, 82

[85] Yingli Yang, Pengpeng Zhang, Laura Happersett, Jianping Xiong, Jie Yang, Maria Chan, Kathryn Beal, Gig Mageras, and Margie Hunt. Choreographing couch and collimator in volumetric modulated arc therapy. *International Journal of Radiation Oncology* Biology* Physics*, 80(4):1238–1247, 2011. 31, 32, 33, 52, 53, 82

[86] Gregory Smyth, Jeffrey C. Bamber, Philip M. Evans, and James L. Bedford. Trajectory optimization for dynamic couch rotation during volumetric modulated arc radiotherapy. *Physics in medicine and biology*, 58(22):8163, 2013. 31, 32, 52, 53, 82

[87] Chantal Audet, Brett A Poffenbarger, Pauling Chang, Paul S Jackson, Robert E Lundahl, Stephen I Ryu, and Gordon R Ray. Evaluation of volumetric modulated arc therapy for cranial radiosurgery using multiple noncoplanar arcs. *Medical physics*, 38(11):5863–5872, 2011. 31, 52, 82

[88] Grant M Clark, Richard A Popple, Brendan M Prendergast, Sharon A Spencer, Evan M Thomas, John G Stewart, Barton L Guthrie, James M Markert, and John B Fiveash. Plan quality and treatment planning technique for single isocenter cranial radiosurgery with volumetric modulated arc therapy. *Practical radiation oncology*, 2(4):306–313, 2012. 32, 52, 82

[89] Ester Orlandi, Tommaso Giandini, Eva Iannacone, Elena De Ponti, Mauro Carrara, Valeria Mongioj, Claudio Stucchi, Silvia Tana, Paolo Bossi, Lisa Licitra, et al. Radiotherapy for unresectable sinonasal cancers: dosimetric comparison of intensity modulated radiation therapy with coplanar and non-coplanar volumetric modulated arc therapy. *Radiotherapy and Oncology*, 113(2):260–266, 2014. 32, 52, 82

[90] Kaley Woods, Dan Nguyen, Angelia Tran, Y Yu Victoria, Minsong Cao, Tianye Niu, Percy Lee, and Ke Sheng. Viability of noncoplanar vmat for liver sbrt compared with coplanar vmat and beam orientation optimized 4π imrt. *Advances in radiation oncology*, 1(1):67–75, 2016. 32, 52

[91] Simona F. Shaitelman, Leonard H. Kim, Di Yan, Alvaro A. Martinez, Frank A. Vicini, and Inga S. Grills. Continuous arc rotation of the couch therapy for the delivery of accelerated partial breast irradiation: A treatment planning analysis. *International Journal of Radiation Oncology* Biology* Physics*, 80(3):771–778, 2011. 32, 52

[92] Jerôme Krayenbuehl, J. Bernard Davis, and I. Frank Ciernik. Dynamic intensity-modulated non-coplanar arc radiotherapy (INCA) for head and neck cancer. *Radiotherapy and oncology*, 81(2):151–157, 2006. 32, 52, 82

[93] Dávid Papp, Thomas Bortfeld, and Jan Unkelbach. A modular approach to intensity-modulated arc therapy optimization with noncoplanar trajectories. *Physics in medicine and biology*, 60(13):5179, 2015. 32, 33, 35, 52, 53, 54, 55, 61, 79, 82, 88, 108

[94] Qihui Lyu, Y Yu Victoria, Dan Ruan, Ryan Neph, Daniel O'Connor, and Ke Sheng. A novel optimization framework for vmat with dynamic gantry couch rotation. *Physics in Medicine & Biology*, 63(12):125013, 2018. 32, 34, 35, 52, 53

[95] Marco Langhans, Jan Unkelbach, Thomas Bortfeld, and David Craft. Optimizing highly noncoplanar vmat trajectories: the novo method. *Physics in Medicine & Biology*, 63(2):025023, 2018. 32, 33, 52, 53

[96] Michael K Fix, Daniel Frei, Werner Volken, Dario Terribilini, Silvan Mueller, Olgun Elicin, Hossein Hemmatazad, Daniel M Aebersold, and Peter Manser. Part 1: optimization and evaluation of dynamic trajectory radiotherapy. *Medical physics*, 45(9):4201–4212, 2018. 32, 52, 53

[97] Eugene L Lawler. The traveling salesman problem: a guided tour of combinatorial optimization. *Wiley-Interscience Series in Discrete Mathematics*, 1985. 34

[98] Gilbert Laporte. The traveling salesman problem: An overview of exact and approximate algorithms. *European Journal of Operational Research*, 59(2):231–247, 1992. 34

[99] Rajesh Matai, Surya Prakash Singh, and Murari Lal Mittal. Traveling salesman problem: an overview of applications, formulations, and solution approaches. *Traveling salesman problem, theory and applications*, 1, 2010. 34, 35

[100] Robert D Plante, Timothy J Lowe, and R Chandrasekaran. The product matrix traveling salesman problem: an application and solution heuristic. *Operations Research*, 35(5):772–783, 1987. 34

[101] Jan Karel Lenstra and AHG Rinnooy Kan. Complexity of vehicle routing and scheduling problems. *Networks*, 11(2):221–227, 1981. 34

[102] Hussain Aziz Saleh and Rachid Chelouah. The design of the global navigation satellite system surveying networks using genetic algorithms. *Engineering Applications of Artificial Intelligence*, 17(1):111–122, 2004. 34

[103] Peng Dong, Hongcheng Liu, and Lei Xing. Monte carlo tree search-based non-coplanar trajectory design for station parameter optimized radiation therapy (sport). *Physics in Medicine & Biology*, 63(13):135014, 2018. 35, 53, 85

[104] Sanjoy Dasgupta, Christos H Papadimitriou, and Umesh Virkumar Vazirani. *Algorithms*. McGraw-Hill Higher Education New York, 2008. 35

[105] Leo Liberti. Branch-and-bound for the travelling salesman problem. *LIX, Ecole Polytechnique, F-91128 Palaiseau*, pages 1–8, 2011. 35

[106] David S Johnson and Lyle A McGeoch. Experimental analysis of heuristics for the stsp. In *The traveling salesman problem and its variations*, pages 369–443. Springer, 2007. 35

[107] Nicos Christofides. Worst-case analysis of a new heuristic for the travelling salesman problem. Technical report, Carnegie-Mellon Univ Pittsburgh Pa Management Sciences Research Group, 1976. 35

[108] MATLAB. The mathworks. *Inc., Natick, Massachusetts, United States*, 488, 2013. 36, 41

[109] Car Adams, MSC. Msc. *Software Corporation*, 2005. 36, 41

[110] Stewart J Becker. Collision indicator charts for gantry-couch position combinations for varian linacs. *Journal of applied clinical medical physics*, 12(3):16–22, 2011. 40, 49

[111] John L Humm, Domenico Pizzuto, Eric Fleischman, and Radhe Mohan. Collision detection and avoidance during treatment planning. *International Journal of Radiation Oncology• Biology• Physics*, 33(5):1101–1108, 1995. 40, 49

[112] Miltiadis F Tsiakalos, Eduard Schrebmann, Kiki Theodorou, and Constantin Kappas. Graphical treatment simulation and automated collision detection for conformal and stereotactic radiotherapy treatment planning. *Medical physics*, 28(7):1359–1363, 2001. 40

[113] Laura Padilla, Erik A Pearson, and Charles A Pelizzari. Collision prediction software for radiotherapy treatments. *Medical physics*, 42(11):6448–6456, 2015. 40

[114] Zhengyou Zhang. Microsoft kinect sensor and its effect. *IEEE multimedia*, 19(2):4–10, 2012. 40, 49

[115] Csaba Pinter, Andras Lasso, An Wang, David Jaffray, and Gabor Fichtinger. Slicerrt: radiation therapy research toolkit for 3d slicer. *Medical physics*, 39(10):6332–6338, 2012. 41

[116] Vinith M Suriyakumar, Renee Xu, Csaba Pinter, and Gabor Fichtinger. Open-source software for collision detection in external beam radiation therapy. In *Medical Imaging 2017: Image-Guided Procedures, Robotic Interventions, and Modeling*, volume 10135, page 101351G. International Society for Optics and Photonics, 2017. 41, 49

[117] International Electrotechnical Commission et al. *Radiotherapy equipment: coordinates, movements and scales*. IEC, 2008. 41

[118] Livia Marrazzo, Chiara Arilli, Marlies Pasler, Martijn Kusters, Richard Canters, Luca Fedeli, Silvia Calusi, Marta Casati, Cinzia Talamonti, Gabriele Simontacchi, et al. Real-time beam monitoring for error detection in imrt plans and impact on dose-volume histograms. *Strahlentherapie und Onkologie*, 194(3):243–254, 2018. 52

[119] Saadia Benhalouche, Julien Bert, Nicolas Boussion, Awen Autret, Olivier Pradier, and Dimitris Visvikis. Gate monte-carlo simulation of an mv-cbct flat panel for synergistic imaging and dosimetric applications in radiotherapy. *IEEE Transactions on Radiation and Plasma Medical Sciences*, 1(5):444–451, 2017. 52

[120] Thahabah Alharthi, Sankar Arumugam, Phil Vial, Lois Holloway, and David Thwaites. Epid sensitivity to delivery errors for pre-treatment verification of lung sbrt vmat plans. *Physica Medica*, 59:37–46, 2019. 52

[121] Benjamin Fahimian, Victoria Yu, Kathleen Horst, Lei Xing, and Dimitre Hristov. Trajectory modulated prone breast irradiation: A linac-based technique combining intensity modulated delivery and motion of the couch. *Radiotherapy and Oncology*, 109(3):475–481, 2013. 52

[122] James Dempsey, Ravindra Ahuja, Arvind Kumar, Jonathan Li, and H Romeijn. Radiation therapy system using interior-point methods and convex models for intensity modulated fluence map optimization, September 22 2005. US Patent App. 11/039,331. 53

[123] Scott Kirkpatrick, C Daniel Gelatt, and Mario P Vecchi. Optimization by simulated annealing. *science*, 220(4598):671–680, 1983. 56

[124] Mark Bangert, Peter Ziegenhein, and Uwe Oelfke. Characterizing the combinatorial beam angle selection problem. *Physics in medicine and biology*, 57(20):6707, 2012. 56, 57, 87

[125] Konstantinos A Mountris, Julien Bert, and Dimitris Visvikis. Prostate brachytherapy optimization using gpu accelerated simulated annealing and monte carlo dose simulation. In *Nuclear Science Symposium, Medical Imaging Conference and Room-Temperature Semiconductor Detector Workshop (NSS/MIC/RTSD), 2016*, pages 1–2. IEEE, 2016. 56

[126] Dimitris Bertsimas, John Tsitsiklis, et al. Simulated annealing. *Statistical science*, 8(1):10–15, 1993. 58

[127] Héctor Sanvicente-Sánchez and Juan Frausto-Solís. A method to establish the cooling scheme in simulated annealing like algorithms. In *International Conference on Computational Science and Its Applications*, pages 755–763. Springer, 2004. 58

[128] Alexander G Nikolaev and Sheldon H Jacobson. Simulated annealing. In *Handbook of metaheuristics*, pages 1–39. Springer, 2010. 58

[129] Bruce Hajek. A tutorial survey of theory and applications of simulated annealing. In *1985 24th IEEE Conference on Decision and Control*, pages 755–760. IEEE, 1985. 58

[130] Joseph Kirk. Traveling salesman problem-genetic algorithm. *Retrieved from the MATLAB File Exchange website: www. mathworks. com/matlabcentral/fileexchange/13680-travelingsalesman-problem-genetic-algorithm*, 2007. 59

[131] E Cisternas, A Mairani, P Ziegenhein, O Jäkel, and M Bangert. matrad-a multi-modality open source 3d treatment planning toolkit. In *World Congress on Medical Physics and Biomedical Engineering, June 7-12, 2015, Toronto, Canada*, pages 1608–1611. Springer, 2015. 60, 94

[132] Andreas Wächter. Short tutorial: getting started with ipopt in 90 minutes. In *Dagstuhl Seminar Proceedings*. Schloss Dagstuhl-Leibniz-Zentrum für Informatik, 2009. 60, 94

[133] Ciyou Zhu, Richard H Byrd, Peihuang Lu, and Jorge Nocedal. Algorithm 778: L-bfgs-b: Fortran subroutines for large-scale bound-constrained optimization. *ACM Transactions on Mathematical Software (TOMS)*, 23(4):550–560, 1997. 60, 94

[134] Gary A Ezzell, Jay W Burmeister, Nesrin Dogan, Thomas J LoSasso, James G Mechalakos, Dimitris Mihailidis, Andrea Molineu, Jatinder R Palta, Chester R Ramsey, Bill J Salter, et al. Imrt commissioning: multiple institution planning and dosimetry comparisons, a report from aapm task group 119. *Medical physics*, 36(11):5359–5373, 2009. 60

[135] David Craft, Mark Bangert, Troy Long, Dávid Papp, and Jan Unkelbach. Shared data for intensity modulated radiation therapy (IMRT) optimization research: The CORT dataset. *GigaScience*, 3:37, 2014. 60, 61

[136] Arie Van't Riet, Ad CA Mak, Marinus A Moerland, Leo H Elders, and Wiebe Van Der Zee. A conformation number to quantify the degree of conformality in brachytherapy and external beam irradiation: application to the prostate. *International Journal of Radiation Oncology* Biology* Physics*, 37(3):731–736, 1997. 62

[137] Christopher Barry Locke and Karl Kenneth Bush. Trajectory optimization in radiotherapy using sectioning (torus). *Medical physics*, 44(7):3375–3392, 2017. 82

[138] Michael S Branicky, Michael M Curtiss, Joshua Levine, and Stuart Morgan. Sampling-based planning, control and verification of hybrid systems. *IEE Proceedings-Control Theory and Applications*, 153(5):575–590, 2006. 83, 93

[139] Steven M LaValle and James J Kuffner Jr. Randomized kinodynamic planning. *The international journal of robotics research*, 20(5):378–400, 2001. 84

[140] Dmitry Berenson, James Kuffner, and Howie Choset. An optimization approach to planning for mobile manipulation. In *2008 IEEE International Conference on Robotics and Automation*, pages 1187–1192. IEEE, 2008. 85

[141] Emre Koyuncu, N Kemal Ure, and Gokhan Inalhan. Integration of path/maneuver planning in complex environments for agile maneuvering ucavs. *Journal of Intelligent and Robotic Systems*, 57(1-4):143, 2010. 85

[142] Sertac Karaman and Emilio Frazzoli. Incremental sampling-based algorithms for optimal motion planning. *arXiv preprint arXiv:1005.0416*, 2010. 86

[143] Iram Noreen, Amna Khan, Khurshid Asghar, and Zulfiqar Habib. A path-planning performance comparison of rrt*-ab with mea* in a 2-dimensional environment. *Symmetry*, 11(7):945, 2019. 86

[144] Dustin J Webb and Jur Van Den Berg. Kinodynamic rrt*: Asymptotically optimal motion planning for robots with linear dynamics. In *2013 IEEE International Conference on Robotics and Automation*, pages 5054–5061. IEEE, 2013. 86

[145] Léonard Jaillet, Francesc J Corcho, Juan-Jesús Pérez, and Juan Cortés. Randomized tree construction algorithm to explore energy landscapes. *Journal of computational chemistry*, 32(16):3464–3474, 2011. 86

[146] wikipedia. Depth-first search — Wikipedia, the free encyclopedia. `https://en.wikipedia.org/w/index.php?title=Depth-first_search&oldid=896938638`, 2019. [Online; accessed 23-July-2019]. 91

[147] Rachel M Holladay and Siddhartha S Srinivasa. Distance metrics and algorithms for task space path optimization. In *2016 IEEE/RSJ International Conference on Intelligent Robots and Systems (IROS)*, pages 5533–5540. IEEE, 2016. 94

[148] Jean-Yves Tinevez. Tree data structure as a MATLAB class - File Exchange - MATLAB Central. `https://fr.mathworks.com/matlabcentral/fileexchange/35623`, 2012. 94

[149] Eugenio Aguirre and Antonio González. Fuzzy behaviors for mobile robot navigation: design, coordination and fusion. *International Journal of Approximate Reasoning*, 25(3):255–289, 2000. 95

DOCTORAT BIOLOGIE
BRETAGNE SANTE
LOIRE

Université de Bretagne Occidentale

Titre : L'Optimisation pour l'arc thérapie par modulation d'intensité volumétrique non-coplanaire

Mots clés : radiothérapie, planification du traitement, VMAT

Résumé : Le VMAT non coplanaire permets de traiter les tumeurs qui sont situées à proximité des organes à risques et ceux qui se trouve à coté ou entourées de tissus normaux. L'utilisation de trajectoires dynamiques pour le mouvement du lit et gantry permets la livraison plus précise des faisceaux pendant les traitements contre le cancer. Malgré les améliorations qui ont été constatées dans le VMAT non coplanaire, des défis persistent.

Dans cette thèse, nous présentons une méthodologie pour la détermination des orientations de faisceaux du traitement. Cette méthodologie est proposée pour éviter la possibilité d'une collision lors du mouvement du lit et gantry pendant le traitement. En même temps, nous proposons un algorithme basé sur le recuit simulé pour la planification de traitement VMAT non coplanaire. Cet algorithme est utilisé pour sélectionner les meilleures orientations possibles du faisceau pour la livraison précise de la dose prescrite.

Nous proposons également un algorithme inspiré de RRT pour générer la trajectoire du livraison du plan VMAT non coplanaire. L'algorithme est proposé pour résoudre le problème de l'insertion des faisceaux intermédiaires comme on a pu constaté dans les méthodes de VMAT par sélection des faisceaux.

Les résultats de cette étude montre des améliorations dans la détection des collisions,l'optimisation globale du plan de traitement e la génération de trajectoires pour la plan du traitement VMAT non coplanaire. Ces améliorations comprennent une meilleure dosimétrie en ce qui concerne les réductions de la dose moyenne aux organes à risque et une trajectoire de livrasion plus efficace.

Nos études indiquent qu'il existe un compromis raisonnable entre la qualité du plan de traitement et la délivrabilité du plan si la dosimétrie du plan de traitement VMAT est surveillée en permanence pendant la génération de trajectoire.

Title : Treatment Planning Optimization for Non-coplanar Volumetric Modulated Arc Therapy

Keywords : radiotherapy, treatment planning, VMAT

Abstract: Non-coplanar VMAT has the potential to treat tumors that are located in close proximity of critical organs or that are partially surrounded by normal tissues. The use of dynamic couch-gantry trajectories offers an opportunity for more precise and accurate delivery of radiation during cancer treatments. Despite the improvements that have been seen in non-coplanar VMAT, challenges still persist.

In this thesis, we present a methodology for the determination of collision free couch-gantry orientations. This methodology is proposed to avoid the possibility of a collision during the motion of the couch and gantry during treatment. We propose an algorithm based on simulated annealing for non-coplanar VMAT treatment planning. This algorithm is used to select the best possible beam orientations for the accurate delivery of the prescribed dose.

We also propose a RRT inspired algorithm for generating the trajectory for the non-coplanar VMAT plan delivery. The algorithm is proposed to solve the problem of the addition of intermediate beam orientations observed in beam selection methods.

From the results of studies on the proposed methods, improvements to collision detection, global optimization and trajectory generation for non-coplanar VMAT treatment planning were observed. These improvements include a better dosimetry with respect to reductions in mean dose to the organs-at-risk and a more efficient delivery trajectory.

Our studies indicate that there exists a reasonable trade-off between treatment plan quality and plan deliverability if the dosimetry of the VMAT treatment plan is continuously monitored during trajectory generation.